AN ABSTRACT OF THE DISSERTATION OF

Kyle Niezgoda for the degree of Doctor of Philosophy in Ocean, Earth and Atmospheric Science presented on August 11, 2022.

Title: Exploring the Relationships Between Stable Water Isotope Ratios and Large Scale Atmospheric Circulation in Paleoclimate Settings Using an Isotope-Enabled General Circulation Model.

Abstract approved: _____

David Noone

Climate model simulations and paleoclimate proxies are two tools that enable an understanding of the climate history of the Earth. When utilized together, they form a powerful paradigm for understanding past changes. Proxies are the only physical link to the past conditions on Earth, and models "fill in the gaps" that are intrinsic to the non-uniform spatial and temporal distribution of proxies. Precipitation changes are a major component of past climates, but proxies do not directly record precipitation amount. Instead, many proxies of precipitation are based on the stable oxygen or hydrogen isotopic composition of precipitation ($\delta^{18}O_p$ and δD_p, or δ_p). Hydroclimate reconstructions from isotope-based proxies are complicated because the relationship between δ_p and climate is not well understood in time and space and is highly variable in both domains. Following in the footsteps of recent work, the studies presented in this dissertation focus on constraining some of the uncertainty

surrounding the δ_p-climate relationship using results from general circulation model (GCM) simulations of two paleoclimate states, the mid-Holocene (MH, 6 ka), and the last glacial maximum (LGM, 21 ka). The MH and LGM contain a deluge of δ_p-based proxies and are historical benchmarks for GCM paleoclimate simulations, making them ideal case studies for this work. In all chapters, the isotope-enabled Community Earth System Model (iCESM) is employed in an "atmosphere-only" setup.

In chapter 1, an overview of the MH tropical hydrology is presented, and simulated δ_p results are compared to the suite of available cave stalagmite (speleothem) proxies. Model results indicate the presence of a relationship between large-scale mean atmospheric circulation and simulated δ_p through changes in the Hadley and Walker circulation. At the scale of individual speleothems, however, shifts in local- and regional-scale hydrology are more important for simulated δ_p than large-scale mean atmospheric changes. These results are discussed in the context of model validation, i.e. the extent to which simulated δ_p resembles the proxy-suggested spatial distribution of δ_p, and the isotopic role of various climate variables in regions where model minus proxy errors are high.

In chapter 2, the influence of the African Humid Period (AHP) on East Asian Summer Monsoon δ_p is investigated by increasing the vegetation coverage in northern Africa during the MH. Location-based water tracers, or "tags", are added to the MH simulation, and a technique is developed for deconstructing $\Delta\delta_p$ into two components: 1) changes in vapor source contribution, and 2) changes in vapor source isotope ratio. Shifts in EASM δ_p are found to be driven by an increased contribution from vapor of Pacific origin by shifts in atmospheric circulation that favor the convergence of Pacific vapor onto East Asia. In this experimental setup, circulation changes are induced only because of vegetation changes in North Africa, suggesting a teleconnection between the AHP and EASM δ_p. These results highlight the relative importance of changes in vapor source contribution over changes in vapor source isotope ratio, and demonstrate that small vapor sources (i.e. those that account for < 5% of total rainfall) can have significant impacts on δ_p.

In chapter 3, iCESM is used to simulate the millennial-scale variability in global temperature that occurred during the most recent glacial period, by inducing changes in the southern extent of North Atlantic sea ice. A warm and cold glacial climate state is simulated by shifting sea ice anomalously northward for the warm and southward for the cold, reminiscent of sea ice extent during Greenland interstadials (GI, warm) and Greenland stadials (GS, cold). GI – GS changes in simulated δ_p are compared to the GI – GS changes in Greenland Summit ice core δ_p. GI-GS variability in simulated δ_p is induced simply by capping the Greenland, Icelandic, and Norwegian seas (GIN) with sea ice, preventing evaporation. Using the same decomposition technique from chapter 2, it is shown that by removing the presence of GIN sea vapor in Greenland precipitation, δ_p of Greenland is reduced without any other factors changing, including the atmospheric circulation and the isotope ratio of vapor sources from other regions.

Results from these chapters highlight the specific role of changes in changes to the spatial variability of moisture sourcing. As long as precipitation is created from vapor source regions with distinct isotopic compositions, shifts towards certain regions over others is the main driving force behind total isotope ratio change. Furthermore, the potential of low-contribution vapor sources as the main drivers of total isotope ratio change is shown to be a significant factor for tropical rainfall, suggesting that non-local and seemingly insignificant vapor sources can dramatically impact total isotope ratios.

Exploring the Relationships Between Stable Water Isotope Ratios and Large Scale Atmospheric Circulation in Paleoclimate Settings Using an Isotope-enabled General Circulation Climate Model.

by

Kyle Niezgoda

A DISSERTATION

submitted to

Oregon State University

In partial fulfillment of

the requirements for the

degree of

Doctor of Philosophy

Presented August 11, 2022

Commencement June 2023

Doctor of Philosophy dissertation of Kyle Niezgoda presented on August 11, 2022

APPROVED:

Major Professor, representing Ocean, Earth and Atmospheric Science

---

Dean of the College of Earth, Ocean, and Atmospheric Sciences

---

Dean of the Graduate School

I understand that my dissertation will become part of the permanent collection of Oregon State University libraries. My signature below authorizes release of my dissertation to any reader upon request.

Kyle Niezgoda, Author

ACKNOWLEDGEMENTS

The author expresses sincere appreciation to all his co-authors for their enthusiastic support and helpful feedback. Thanks to the graduate students of the Climate Processes Research Group (CPRG) at Oregon State University, Kaleb Horlick, Dean Henze, and Amari Dolan-Caret, for their academic camaraderie and many fruitful conversations. This PhD was funded by grants from the National Science Foundation (NSF) Paleoclimate Perspective on Climate Change.

CONTRIBUTION OF AUTHORS

Chapter 1

David Noone provided key science advice and assisted in experimental design.

Bronwen Konecky provided guidance on proxy databases and model interpretation.

Chapter 2

David Noone assisted in development of analytical techniques.

Rich Fiorella provided methodology for adding location-based tags to CESM.

Clay Tabor provided vegetation files for Green Sahara forcing.

Chapter 3

Christo Buizert aided in science direction, experimental design, and results interpretation.

David Noone provided scientific support and guidance for results interpretation.

Kaden Martin supported results interpretation.

TABLE OF CONTENTS

PAGE

GENERAL INTRODUCTION 1

Motivation and scientific scope 1

Proxies and models as tools for paleoclimate reconstruction 2

Precipitation isotope ratios in paleoclimate modeling of the MH and LGM 4

Evolving beyond the amount- and temperature-effect: circulation-scale interpretations 6

Bibliography 8

CHAPTER 1: A SIMULATION OF THE MID-HOLOCENE TROPICAL HYDROLOGY USING THE ISOTOPE-ENABLED COMMUNITY ATMOSPHERE MODEL: MODEL OVERVIEW, COMPARISON TO SPELEOTHEM PROXIES, AND INSIGHTS ON INTERPRETATION OF Δ-BASED PROXIES. 15

Abstract 15

Introduction 16

Objectives 18

Methods and materials 19

Isotope-enabled CESM (iCESM) 19

Speleothem proxy records 20

Results 20

General overview of MH-PI hydrology 20

Hadley and Walker circulation relationship to $\Delta\delta^{18}O_p$ 22

Model-proxy comparison 24

Best-fit composite analysis 25

East China best-fit composite mean climatology 27

Northwest Africa best-fit composite mean climatology 28

Oman (Qunf cave) best-fit composite mean climatology 28

Northern Australia best-fit composite mean climatology 29

Discussion 29

Bibliography 32

Figures & Tables 38

CHAPTER 2: TARGETED TAGGING EXPERIMENTS REVEAL A PACIFIC OCEAN INFLUENCE ON EAST ASIAN SUMMER MONSOON $\Delta^{18}O_P$ IN GREEN-SAHARA SIMULATIONS. 51

TABLE OF CONTENTS (continued)

PAGE

ABSTRACT 51

INTRODUCTION 52

Asian Monsoon response to the green Sahara 54

Objectives 56

METHODS AND MATERIALS 56

Isotope-enabled, tracer-enabled CAM 56

Tagging setup 57

Tag decomposition of $\Delta\delta^{18}O_{total}$ 58

Moisture streamlines 60

Speleothem data 60

RESULTS 61

Model Validation 61

$\Delta\delta^{18}O_{total}$ decomposition 61

NPA and SPA tags 62

Physical interpretation of f-driven response for NPA 63

Regional continental recycling and western vapor source influences on the CHN tag 65

DISCUSSION 65

BIBLIOGRAPHY 70

FIGURES & TABLES 76

CHAPTER 3: D-O VARIABILITY IN GREENLAND SUMMIT $\Delta^{18}O_P$ CONTROLLED BY SOUTHERN EXTENT OF SEA ICE IN THE NORTH ATLANTIC DURING THE LAST GLACIAL 82

ABSTRACT 82

INTRODUCTION 83

Objectives 85

METHODS AND MATERIALS 86

Isotope-enabled CAM 86

LGM sea-ice setup and experimental design 86

Tagging setup 87

Decomposition of Greenland Summit $\Delta\delta^{18}O$ 88

RESULTS 89

TABLE OF CONTENTS (continued)

PAGE

Model results for ΔT, $\Delta\delta^{18}O_p$ 89

Summit tag $\Delta\delta^{18}O$ decomposition 89

Seasonal $\Delta\delta^{18}O$ decomposition 92

Sea ice control on vapor sourcing and atmospheric circulation 93

DISCUSSION 94

BIBLIOGRAPHY 96

FIGURES & TABLES 101

GENERAL CONCLUSION 108

FIGURES 111

LIST OF FIGURES

PAGE

Chapter 1

1.1 Proxy speleothem locations……38

1.2 Annual and summertime change in 2-meter air temperature and precipitation rate for MH-PI…..40

1.3 Change in simulated precipitation isotope ratio, Δδ18Op……40

1.4 Δδ18Op vs ΔP for annual mean land-based precipitation between latitudes 30° S and 30° N……..41

1.5 Zonal mean vapor transport and precipitation isotope ratio……42

1.6 Estimations of changes to the Hadley Cell and ITCZ position during the MH……..43

1.7 Hovmoller diagrams of $\delta^{18}O_p$ and $\Delta\delta^{18}O_p$ in latitude and month, averaged over longitudes 0° - 180°……..44

1.8 As in Fig. 1.7, except averaged over longitudes 180° - 360°……44

1.9 $\Delta\delta^{18}O$ of 10 cm soil water vs $\Delta\delta^{18}O_p$, colored by Δrelative humidity (RH) at 2m above surface…….45

1.10 Model-proxy comparison of $\delta^{18}O$……46

1.11 Histograms of simulated iCAM $\Delta\delta^{18}O_p$ linearly interpolated to speleothem locations……47

1.12 Best-fit composite results……48

1.13 Proxy-model comparison using best-fit composite data……49

1.14 Best-fit composite results for PSL, IVT, and T, as in Fig. 1.11……..50

1.15 Best-fit composite results for $\delta^{18}O_E$ and E, as in Fig. 1.11……50

1.16 Best-fit composite results for $\delta^{18}O_V$ and ω_{500}, as in Fig. 1.11……..50

Chapter 2

2.1 The tag layout, colored by shared regions……75

2.2 MJJAS mean simulated $\Delta\delta^{18}O_p$ with speleothem MH-PI values……..76

2.3 MJJAS mean Δδ18Op of the 5 EASM speleothem locations for the MHdry – PI (brown), MHgs – PI (green), and proxy values (black crosses)……77

2.4 The MJJAS mean tag decomposition of $\Delta\delta^{18}O_p$ for the EASM region……78

LIST OF FIGURES (continued)

PAGE

2.5 MJJAS fractional change in q_{NPA} from the MHdry to MHgs, $\Delta qfrac_{NPA}$……77

2.6 The tag decomposition of $\Delta\delta^{18}O_p$ as in Fig. 2.4, but for Western China, defined by the EASM box shifted 8° west……80

Chapter 3

3.1 Sea ice southern extent and annual mean SST for warm/LGM_{GI} (left) and cold/LGM_{GS} (right)……100

3.2 The tag layout, colored by shared regions……101

3.3 Temperature and precipitation isotope ratio changes during GI, GS, and the GI-GS difference….102

3.4 Decomposition of annual sum Greenland Summit precipitation into tag regions……103

3.5 Decomposition of Greenland Summit precipitation into seasons……104

3.6 Evaporation and sea ice extent across the seasonal cycle……105

3.7 1 hour back-trajectories of A45 tagged vapor with evaporation contours and sea ice southern extent, all using DJF data……106

Conclusion

C.1 The constructed decomposition of the perturbation thought experiment……110

LIST OF TABLES

PAGE

Chapter 1

1.1 Speleothem metadata……39

Chapter 2

2.1 Tag layout metadata……75

2.2 The 3 components of the vapor budget along the NPA vapor transport pathway……79

Chapter 3

3.1 Tag layout metadata……101

DEDICATION

To my grandfather, Albert Niezgoda, who always thought weather and climate were cool

General Introduction

Motivation and scientific scope

Over the last several decades, climate change research has delivered a few clear messages: the Earth is warming at unprecedented rates (Schiesinger & Jiang, 1992; Ding et al., 2007; Hansen, 2009), weather patterns are changing rapidly (Füssel, 2009), and ecosystems are undergoing dramatic transformations (Thomas, 2010; Chaudhury, 2022; Scheffers et al., 2022). Climate change and global warming pose serious existential risks. Since the industrial revolution began around the year 1850 CE, global mean temperature has increased by approximately 1° C, severe weather has become even more severe (Karl & Trenberth, 2003; Zhou, 2021), delicate balances in climate systems have been disturbed (Ming et al., 2021), and a growing list of endangered and extinct species has critically threatened ecosystems (Ceballos et al., 2015; Mach et al., 2016). Confident and accurate projections of climate change impacts are absolutely critical. They empower policy makers, interest groups, and stakeholders to make informed decisions about the future, saving money and lives, and preserving lifestyles, cultural customs, and livelihoods (Webster et al., 2003; Kunreuther et al., 2013; Diaz & Moore, 2017).

Changes to the physical climate result from the influence of two factors. First are anthropogenic (human-based) influences such as the emission of greenhouse gases through the burning of coal and fossil fuels, land use change through activities such as deforestation and agriculture, or pollution and overconsumption of Earthen materials. The characteristic global warming of the late 20th and early 21st century is "overwhelmingly due to human influences" (IPCC AR6 technical summary [Arias et al., 2021]; see also Crowley et al., 2020). Second is the "natural variability" of the Earth, which are changes to the Earth's climate that occur without the intervention of humans, such as changes to the Earth's orbital characteristics, changes in volcanic activity, and other natural sources of climate variability (Stern & Kaufman, 2014). Accurate predictions of future climate change are guided by a thorough understanding of the natural variability of the Earth. Past climate states that sufficiently resemble the modern day can provide an historical analogue for how the Earth might change in the future. For instance, extensive research on the anomalously warm Paleocene-Eocene Thermal Maximum (PETM, 55

Ma) has revealed several key concepts on how the modern climate might respond to a high emissions global warming scenario (Bowen et al., 2006; Sluijs et al., 2014; Aze, 2022). However, for most paleo-analogues, the rapid pace of modern global warming makes comparisons to much slower past climate change events difficult (Lioubimtseva, 2004; Haywood et al., 2011). The recent history of the Earth's climate also provides the historical context for modern climate change, i.e. the status of the climate before dramatic anthropogenic-driven change began (Mann et al., 1999; Marcott et al., 2013). The realized climate change signal is a combination of anthropogenic signals superimposed on the natural changes that would have happened regardless of the presence of humans. This dissertation focuses on the latter component, the natural influence, by observing recent changes (i.e. the last ~10k years) to the Earth's climate.

Proxies and models as tools for paleoclimate reconstruction

Paleoclimate research, or the study of the climate history of the Earth, is a useful endeavor for understanding the role of natural variability on future climate change (Snyder, 2010; Hansen & Sato, 2012). Paleoclimate discoveries detail the broad-scale scope of the evolution of weather patterns over long periods of time. For instance, decades of research has revealed a detailed cadence of glacial-interglacial cycles, with a period of approximately 100k years, over the last 800k years (Imbrie et al., 1992; Petit et al., 1999; Jouzel et al., 2007; Lüthi et al., 2008). Paleoclimate reconstructions like these have primarily been achieved through the collection and study of paleoclimate proxies – environmental specimens that physically preserve characteristics of the past and provide information where direct measurements are impossible. Our understanding of the 100k year glacial-interglacial cycle, for example, is largely based on the oxygen isotope ratio and CO_2 concentration of ancient atmospheric gases trapped in air bubbles in ice cores extracted from Greenland and Antarctica (Imbrie et al., 1993). Proxies are the only physical link to past conditions, but they are complicated by the need to transform the geological value recorded by the proxy into a useful climate variable (Dee et al., 2015). For instance, dendrochronology uses tree ring widths (a geological value) to reconstruct temperature and rainfall (climate variables), but the exact relationship between tree ring widths and temperature/precipitation is variable in space, time, between species, among organisms of the same species, and has biases and uncertainties (Hughes, 2002; Cook &

Pederson, 2011). Proxy-based reconstructions of past climates have been greatly enabled by recent data products that have assembled large amounts of proxies into a common database (e.g. PAGES2k consortium, 2017; Iso2k [Konecky et al., 2020]).

Model simulations of paleoclimate states provide important information on climates of the past as well. Modern Earth System Models (ESMs) are highly complex, representing physical processes across the various components of the Earth's climate, like the atmosphere and ocean (the classic components of a general circulation model; Manabe, 1969), as well as the cryosphere (land and sea ice), the land surface (topography, thermal radiation), land based hydrology (riverine systems and lakes), the biosphere (vegetation, evapotranspiration, the carbon cycle), geochemical processes (trace gases, nutrient transport), and more. Climate scientists have benefited from the continuous evolution of ESMs as tools for reconstructing past climates and forecasting future climates, and results from ESM simulations form a foundational aspect of any science endeavor under the umbrella of climate change research. Paleoclimate modelling ventures often focus their study on the equilibrium climate state of a specific time period. For example, the last glacial maximum (LGM, approx. 21 ka) has been extensively modelled since the birth of the most primitive general circulation models (Manabe & Wetherald, 1975; Rind, 1987; Bush & Philander 1999; Kitoh et al., 2001; Hewitt et al., 2003; for most recent PMIP overview of the LGM simulations see Kageyama et al., 2021). The wealth of knowledge garnered from these analyses has expanded our understanding on the role of ice-albedo feedbacks (Broccoli & Manabe, 1987; Burt, Randall, & Otto-Bliesner, 2014), the nature of glacial collapse (Abe-Ouchi et al., 2002), and climate sensitivity (Harvey, 1989; Hargreaves et al., 2012).

Model simulations and proxies are symbiotic components of a complete paleoclimate reconstruction (Schmidt et al., 2014). Proxy records are often spatially and temporally sparse, but paleoclimate model simulations play a complementary role by filling in these gaps. In addition, proxies are often spatially bound units of measurement, with a single value representing a single point in space, whereas the real climate has well-known spatial covariance. Model simulations provide the covariance between the locally defined proxy value and the regional-scale climate phenomena. In other words, models can provide guidance on

how to interpret proxies in terms of regional scale climate. At the same time, ESM simulations of past climates are decidedly imperfect. They contain known biases, parameterize away complexities from many climate phenomena, and are unable to reproduce some features of the climate. Proxies provide guidance on the accuracy of climate model simulations by validating model results if they resemble the proxy value (model-proxy validation), by nudging the model towards a state that more closely resembles the proxy value, or by setting a standard for model tuning.

The model-proxy relationship defines the scientific foundation of this dissertation. The research presented in the three chapters following this introduction seeks to identify novel techniques for using results from ESM paleoclimate simulations to broaden our interpretation of paleoclimate proxies, and to identify areas in which ESM simulations fail to reproduce the proxy-suggested paleoclimate state. This is achieved using a case study-like approach with two time periods: the mid-Holocene (MH, 6 ka) and the last glacial maximum (LGM, 21 ka). These time periods have an historic legacy in the paleoclimate modeling world, an extensive network of proxies, and key knowledge gaps, which are discussed in further detail in the following chapters.

Precipitation isotope ratios in paleoclimate modeling of the MH and LGM

Despite extensive research, discussion and debate continues surrounding hydrology changes that occurred during the MH and LGM, namely to the spatial and temporal patterns of precipitation. Precipitation is a key aspect of the hydrologic balance, but proxies do not directly record precipitation – as mentioned above, various geologic values can be transformed to precipitation. Many paleoclimate proxies of rainfall are based on the stable oxygen or hydrogen isotopic composition of precipitation ($\delta^{18}O_p$ and δD_p, or δ_p). In studies of modern climate, δ_p is widely recognized as an effective tracer of atmospheric circulation processes (e.g., Dansgaard, 1964; Rozanski, 200; Noone at el., 2011). Water undergoing a phase change has an associated isotopic change, or fractionation. For example, ^{18}O more readily condenses compared to ^{16}O because it has a lower diffusivity, and as such condensate tends to be “heavier” than (more enriched in ^{18}O than) the vapor from which condensation occurred, i.e. $\delta_{condensate} > \delta_{vapor}$. Ocean

basins can have a distinctive surface water isotope ratio, which is reflected in the overlying δ_{vapor}. This imprints parcels of vapor with information on the evaporation source location, which is preserved as the vapor is moved around. In summary, δ_p integrates the evaporation, condensation, transport, and source history of water as it cycles through the atmosphere and eventually falls as precipitation. Proxies of precipitation isotope ratios come in various geologic forms, such as cave stalagmites (McDermott, 2004), tree rings (e.g. Ballesteros-Canovás et al., 2015; Elshorbagy et al., 2016), and leaf waxes (e.g. Collins et al., 2013; Aichner et al., 2015; Feakins et al., 2016). Paleoclimate reconstructions using these proxies, now ubiquitous in the literature, have revolutionized our understanding of Holocene and Pleistocene climate change (e.g. Haug et al., 2001; Dykoski et al., 2005).

In tropical rainfall, a strong negative correlation is often observed between isotope ratios and precipitation amount, particularly on monthly and longer timescales (Dansgaard, 1964; Moerman et al., 2013). This finding has resulted in a common way to interpret tropical δ_p-based proxies, known as the "amount effect": variability in δ_p should be interpreted to reflect long-term variations in precipitation amount (Sachse et al., 2012, and refs therein). However, new observations have demonstrated that the amount effect is oversimplified in many tropical settings (e.g., Moerman et al., 2013; Kurita et al., 2009; Aggarwal et al., 2004). Recent modeling studies have brought into question the basic mechanisms responsible for the amount effect (e.g. Risi et al., 2008; Field et al., 2010; Konecky et al., 2019). Paleoclimate shifts in δ_p from tropical rainfall proxies are increasingly being thought of from the perspective of regional-scale hydrology. For instance, for most tropical rainfall, vapor supply comes from multiple isotopically-distinct evaporation regions; long-term shifts towards one region can drive shifts in δ_p that are unrelated to changes in precipitation amount (Aizen et al., 1996; Saravana Kumar et al., 2010; Yao et al., 2013; Wei et al., 2018).

Precipitation isotope ratios are a particularly unique variable for interpreting paleoclimate records because the commonly used function that converts δ_p into a climate variable is different for tropical versus polar precipitation. The amount effect plays a key role in the tropics, which is often used as a first-order approximation for δ_p-based reconstructions.

However, at higher latitudes, δ_p-based proxies are thought of as paleothermometers, i.e. proxies of temperature (Lorius & Merlivat, 1975; Masson-Delmont et al., 2008). Some recent studies have addressed this geographical influence on δ_p-based reconstructions as a reflection of the magnitude of spatial variability in certain climate variables between the two regions (Siler et al., 2021), but this geographic discrepancy is still largely unresolved.

Evolving beyond the amount- and temperature-effect: circulation-scale interpretations

δ_p is an invaluable asset to paleoclimatologists because it is, arguably, the closest link we have to the actual precipitation that hits the ancient surface. However, the proverbial "elephant in the room" remains; how can δ_p, a climate variable delicately associated with the strength of isotopic fractionation in the hydrologic system, provide two dramatically different climate interpretations based on geography, i.e. precipitation amount in the tropics and temperature in the poles? The oxygen molecules in water vapor do not know whether they are near the poles or the equator; put simply, δ_p obeys only the physics of fractionation. Because of this, the classic approach to using δ_p as a tool for paleoclimate reconstructions via the amount- and temperature-effects is an oversimplification that ignores components of the climate that play known roles in shaping δ_p, and greatly reduces the power of δ_p as a paleoclimate proxy.

δ_p of land-based precipitation results from the bulk fractionation and mixing that occurs at key points in the hydrologic cycle. Vapor parcels form from evaporation or evapotranspiration, are advected around via winds, and are eventually condensed out as precipitation. Evaporation and condensation are fractionating events, whereas advection is only mixing (i.e. non-fractionating). As vapor parcels are advected, they can be resupplied via evaporation or desiccated via condensation. This describes the entire isotopic hydrologic cycle. As such, a complete numerical description of δ_p is enabled by quantifying the bulk fractionating effects of total upstream evaporation and condensation, as well as the non-fractionating effect of mixing. To understand the climate interpretations of δ_p is to understand the relative contribution of these upstream processes. Fortunately, isotope-enabled general circulation models (GCMs) can fully quantify these values.

In the following three chapters, I utilize paleoclimate simulations of the MH (chs. 1 & 2) and LGM (ch. 3) with the goal of enhancing the interpretation of various δ_p-based proxies. In chapter 1, I use several speleothem archives from tropical regions, and compare these records to simulated δ_p. I further explore the simulated large-scale tropical climate shifts that occur during the MH, and link these shifts to MH changes in δ_p. In chapter 2 I detail the role of shifts in moisture sourcing on the δ_p of the East Asian Summer Monsoon (EASM) using an approach that decomposes simulated EASM $\Delta\delta_p$ into various regions that act as moisture sources for EASM rainfall. These results provide critical context for the interpretation of various speleothem proxies of the EASM. Finally, in chapter 3, I apply the same decomposition approach to δ_{ice} in Greenland ice cores to demonstrate the role of sea-ice on evaporation regimes and moisture sourcing for Greenland precipitation. These results are placed in the context of rapid climate change events during the last glacial period (Dansgaard-Oeschger events) and provide guidance on how to resolve the "temporal slope" between Greenland δ_{ice} and temperature.

Bibliography

Abe-Ouchi, A., Segawa, T., Yamagishi, T., Saito, F., & Nishimura, T. (2002). Topographic Effects of the Ice Sheets on their Self Maintenance and Shaping the Climate during the LGM. 2002, PP21B-0328.

Aichner, B., Feakins, S. J., Lee, J. E., Herzschuh, U., & Liu, X. (2015). High-resolution leaf wax carbon and hydrogen isotopic record of the late Holocene paleoclimate in arid Central Asia. Climate of the Past, 11(4), 619–633. https://doi.org/10.5194/cp-11-619-2015

Aizen, V., Aizen, E., Melack, J., & Martma, T. (1996). Isotopic measurements of precipitation on central Asian glaciers (southeastern Tibet, northern Himalayas, central Tien Shan). Journal of Geophysical Research: Atmospheres, 101(D4), 9185–9196. https://doi.org/10.1029/96JD00061

Aze, T. (2022). Unraveling ecological signals from a global warming event of the past. Proceedings of the National Academy of Sciences, 119(13), e2201495119. https://doi.org/10.1073/pnas.2201495119

Ballesteros-Cánovas, J. A., Stoffel, M., St George, S., & Hirschboeck, K. (2015). A review of flood records from tree rings. Progress in Physical Geography: Earth and Environment, 39(6), 794–816. https://doi.org/10.1177/0309133315608758

Berger, A., Dickenson, R. E., & Kidson, J. W. (1989). Understanding Climate Change. American Geophysical Union.

Bowen, G. J., Bralower, T. J., Delaney, M. L., Dickens, G. R., Kelly, D. C., Koch, P. L., Kump, L. R., Meng, J., Sloan, L. C., Thomas, E., Wing, S. L., & Zachos, J. C. (2006). Eocene hyperthermal event offers insight into greenhouse warming. Eos, Transactions American Geophysical Union, 87(17), 165–169. https://doi.org/10.1029/2006EO170002

Broccoli, A. J., & Manabe, S. (1987). The influence of continental ice, atmospheric CO2, and land albedo on the climate of the last glacial maximum. Climate Dynamics, 1(2), 87–99. https://doi.org/10.1007/BF01054478

Bush, A. B. G., & Philander, S. G. H. (1999). The climate of the Last Glacial Maximum: Results from a coupled atmosphere-ocean general circulation model. Journal of Geophysical Research: Atmospheres, 104(D20), 24509–24525. https://doi.org/10.1029/1999JD900447

Ceballos, G., Ehrlich, P. R., Barnosky, A. D., García, A., Pringle, R. M., & Palmer, T. M. (2015). Accelerated modern human–induced species losses: Entering the sixth mass extinction. Science Advances, 1(5), e1400253. https://doi.org/10.1126/sciadv.1400253

Chaudhury, M. (2014). Key Points on Climate Adaptation from the New IPCC Report. https://www.wri.org/insights/key-points-climate-adaptation-new-ipcc-report

Collins, J. A., Schefuß, E., Mulitza, S., Prange, M., Werner, M., Tharammal, T., Paul, A., & Wefer, G. (2013). Estimating the hydrogen isotopic composition of past precipitation using leaf-waxes from western Africa. Quaternary Science Reviews, 65, 88–101. https://doi.org/10.1016/j.quascirev.2013.01.007

Cook, E. R., & Pederson, N. (2011). Uncertainty, Emergence, and Statistics in Dendrochronology. In M. K. Hughes, T. W. Swetnam, & H. F. Diaz (Eds.), Dendroclimatology: Progress and Prospects (pp. 77–112). Springer Netherlands. https://doi.org/10.1007/978-1-4020-5725-0_4

Crowley, T. J. (2000). Causes of Climate Change Over the Past 1000 Years. Science, 289(5477), 270–277. https://doi.org/10.1126/science.289.5477.270

Dansgaard, W. (1964). Stable isotopes in precipitation. Tellus, 16(4), 436–468. https://doi.org/10.3402/tellusa.v16i4.8993

Dee, S., Emile-Geay, J., Evans, M. N., Allam, A., Steig, E. J., & Thompson, D. m. (2015). PRYSM: An open-source framework for PRoxY System Modeling, with applications to oxygen-isotope systems. Journal of Advances in Modeling Earth Systems, 7(3), 1220–1247. https://doi.org/10.1002/2015MS000447

Diaz, D., & Moore, F. (2017). Quantifying the economic risks of climate change. Nature Climate Change, 7(11), 774–782. https://doi.org/10.1038/nclimate3411

Ding, Y., Ren, G., Zhao, Z., Xu, Y., Luo, Y., Li, Q., & Zhang, J. (2007). Detection, causes and projection of climate change over China: An overview of recent progress. Advances in Atmospheric Sciences, 24(6), 954–971. https://doi.org/10.1007/s00376-007-0954-4

Dykoski, C. A., Edwards, R. L., Cheng, H., Yuan, D., Cai, Y., Zhang, M., Lin, Y., Qing, J., An, Z., & Revenaugh, J. (2005). A high-resolution, absolute-dated Holocene and deglacial Asian monsoon record from Dongge Cave, China. Earth and Planetary Science Letters, 233(1), 71–86. https://doi.org/10.1016/j.epsl.2005.01.036

Feakins, S. J., Bentley, L. P., Salinas, N., Shenkin, A., Blonder, B., Goldsmith, G. R., Ponton, C., Arvin, L. J., Wu, M. S., Peters, T., West, A. J., Martin, R. E., Enquist, B. J., Asner, G. P., & Malhi, Y. (2016). Plant leaf wax biomarkers capture gradients in hydrogen isotopes of precipitation from the Andes and Amazon. Geochimica et Cosmochimica Acta, 182, 155–172. https://doi.org/10.1016/j.gca.2016.03.018

Field, R. D., Jones, D. B. A., & Brown, D. P. (2010). Effects of postcondensation exchange on the isotopic composition of water in the atmosphere. Journal of Geophysical Research: Atmospheres, 115(D24). https://doi.org/10.1029/2010JD014334

Füssel, H.-M. (2009). An updated assessment of the risks from climate change based on research published since the IPCC Fourth Assessment Report. Climatic Change, 97(3), 469. https://doi.org/10.1007/s10584-009-9648-5

Hansen, J. (2010). Storms of My Grandchildren: The Truth About the Coming Climate Catastrophe and Our Last Chance to Save Humanity. Bloomsbury Publishing USA.

Hansen, J. E., & Sato, M. (2012). Paleoclimate Implications for Human-Made Climate Change. In A. Berger, F. Mesinger, & D. Sijacki (Eds.), Climate Change (pp. 21–47). Springer. https://doi.org/10.1007/978-3-7091-0973-1_2

Hargreaves, J. C., Annan, J. D., Yoshimori, M., & Abe-Ouchi, A. (2012). Can the Last Glacial Maximum constrain climate sensitivity? Geophysical Research Letters, 39(24). https://doi.org/10.1029/2012GL053872

Harvey, L. D. D. (1989). An energy balance climate model study of radiative forcing and temperature response at 18 ka. Journal of Geophysical Research: Atmospheres, 94(D10), 12873–12884. https://doi.org/10.1029/JD094iD10p12873

Haug, G. H., Hughen, K. A., Sigman, D. M., Peterson, L. C., & Röhl, U. (2001). Southward Migration of the Intertropical Convergence Zone Through the Holocene. Science, 293(5533), 1304–1308. https://doi.org/10.1126/science.1059725

Haywood, A. M., Ridgwell, A., Lunt, D. J., Hill, D. J., Pound, M. J., Dowsett, H. J., Dolan, A. M., Francis, J. E., & Williams, M. (2011). Are there pre-Quaternary geological analogues for a future greenhouse warming? Philosophical Transactions of the Royal Society A: Mathematical, Physical and Engineering Sciences, 369(1938), 933–956. https://doi.org/10.1098/rsta.2010.0317

Hewitt, C., Stouffer, R., Broccoli, A., Mitchell, J., & Valdes, P. J. (2003). The effect of ocean dynamics in a coupled GCM simulation of the Last Glacial Maximum. Climate Dynamics, 20(2), 203–218. https://doi.org/10.1007/s00382-002-0272-6

Hughes, M. K. (2002). Dendrochronology in climatology – the state of the art. Dendrochronologia, 20(1), 95–116. https://doi.org/10.1078/1125-7865-00011

Imbrie, J., Berger, A., Boyle, E. A., Clemens, S. C., Duffy, A., Howard, W. R., Kukla, G., Kutzbach, J., Martinson, D. G., McIntyre, A., Mix, A. C., Molfino, B., Morley, J. J., Peterson, L. C., Pisias, N. G., Prell, W. L., Raymo, M. E., Shackleton, N. J., & Toggweiler, J. R. (1993). On the structure and origin of major glaciation cycles 2. The 100,000-year cycle. Paleoceanography, 8(6), 699–735. https://doi.org/10.1029/93PA02751

Imbrie, J., Boyle, E. A., Clemens, S. C., Duffy, A., Howard, W. R., Kukla, G., Kutzbach, J., Martinson, D. G., McIntyre, A., Mix, A. C., Molfino, B., Morley, J. J., Peterson, L. C., Pisias, N. G., Prell, W. L., Raymo, M. E., Shackleton, N. J., & Toggweiler, J. R. (1992). On the Structure and Origin of Major Glaciation Cycles 1. Linear Responses to Milankovitch Forcing. Paleoceanography, 7(6), 701–738. https://doi.org/10.1029/92PA02253

IPCC, 2007: Climate Change2007: The Physical Science Basis. Contribution of Working Group I to the Fourth Assessment Report of the Intergovernmental Panel on Climate Change [Solomon, S., D. Qin, M. Manning, Z. Chen, M. Marquis, K.B. Averyt, M. Tignor and H.L. Miller (eds.)]. Cambridge University Press, Cambridge, United Kingdom and New York, NY, USA, 996 pp.

Joussaume, S., Sadourny, R., & Jouzel, J. (1984). A general circulation model of water isotope cycles in the atmosphere. Nature, 311(5981), 24–29. https://doi.org/10.1038/311024a0

Jouzel, J., Masson-Delmotte, V., Cattani, O., Dreyfus, G., Falourd, S., Hoffmann, G., Minster, B., Nouet, J., Barnola, J. M., Chappellaz, J., Fischer, H., Gallet, J. C., Johnsen, S., Leuenberger, M., Loulergue, L., Luethi, D., Oerter, H., Parrenin, F., Raisbeck, G., … Wolff, E. W. (2007). Orbital and Millennial Antarctic Climate Variability over the Past 800,000 Years. Science, 317(5839), 793–796. https://doi.org/10.1126/science.1141038

Kageyama, M., Harrison, S. P., Kapsch, M.-L., Lofverstrom, M., Lora, J. M., Mikolajewicz, U., Sherriff-Tadano, S., Vadsaria, T., Abe-Ouchi, A., Bouttes, N., Chandan, D., Gregoire, L. J., Ivanovic, R. F., Izumi, K., LeGrande, A. N., Lhardy, F., Lohmann, G., Morozova, P. A., Ohgaito, R., … Zhu, J. (2021). The PMIP4 Last

Glacial Maximum experiments: Preliminary results and comparison with the PMIP3 simulations. Climate of the Past, 17(3), 1065–1089. https://doi.org/10.5194/cp-17-1065-2021

Karl, T. R., & Trenberth, K. E. (2003). Modern Global Climate Change. Science, 302(5651), 1719–1723. https://doi.org/10.1126/science.1090228

Kitoh, A., Murakami, S., & Koide, H. (2001). A simulation of the Last Glacial Maximum with a coupled atmosphere-ocean GCM. Geophysical Research Letters, 28(11), 2221–2224. https://doi.org/10.1029/2000GL012271

Konecky, B. L., McKay, N. P., Churakova (Sidorova), O. V., Comas-Bru, L., Dassié, E. P., DeLong, K. L., Falster, G. M., Fischer, M. J., Jones, M. D., Jonkers, L., Kaufman, D. S., Leduc, G., Managave, S. R., Martrat, B., Opel, T., Orsi, A. J., Partin, J. W., Sayani, H. R., Thomas, E. K., … Iso2k Project Members. (2020). The Iso2k database: A global compilation of paleo-$\delta^{18}O$ and $\delta^{2}H$ records to aid understanding of Common Era climate. Earth System Science Data, 12(3), 2261–2288. https://doi.org/10.5194/essd-12-2261-2020

Konecky, B. L., Noone, D. C., & Cobb, K. M. (n.d.). The Influence of Competing Hydroclimate Processes on Stable Isotope Ratios in Tropical Rainfall. Geophysical Research Letters, 0(0). https://doi.org/10.1029/2018GL080188

Kunreuther, H., Heal, G., Allen, M., Edenhofer, O., Field, C. B., & Yohe, G. (2013). Risk management and climate change. Nature Climate Change, 3(5), 447–450. https://doi.org/10.1038/nclimate1740

Kurita, N., Ichiyanagi, K., Matsumoto, J., Yamanaka, M. D., & Ohata, T. (2009). The relationship between the isotopic content of precipitation and the precipitation amount in tropical regions. Journal of Geochemical Exploration, 102(3), 113–122. https://doi.org/10.1016/j.gexplo.2009.03.002

Kutzbach, J. E., & Guetter, P. J. (1986). The Influence of Changing Orbital Parameters and Surface Boundary Conditions on Climate Simulations for the Past 18 000 Years. Journal of the Atmospheric Sciences, 43(16), 1726–1759. https://doi.org/10.1175/1520-0469(1986)043<1726:TIOCOP>2.0.CO;2

Lioubimtseva, E. (2004). Climate change in arid environments: Revisiting the past to understand the future. Progress in Physical Geography: Earth and Environment, 28(4), 502–530. https://doi.org/10.1191/0309133304pp422oa

Lorius, C., & Merlivat, L. (1975). Distribution of mean surface stable isotopes values in east Antarctica; observed changes with depth in coastal area (p. 18).

Lüthi, D., Le Floch, M., Bereiter, B., Blunier, T., Barnola, J.-M., Siegenthaler, U., Raynaud, D., Jouzel, J., Fischer, H., Kawamura, K., & Stocker, T. F. (2008). High-resolution carbon dioxide concentration record 650,000–800,000 years before present. Nature, 453(7193), 379–382. https://doi.org/10.1038/nature06949

Mach, K. J., Mastrandrea, M. D., Bilir, T. E., & Field, C. B. (2016). Understanding and responding to danger from climate change: The role of key risks in the IPCC AR5. Climatic Change, 136(3), 427–444. https://doi.org/10.1007/s10584-016-1645-x

Manabe, S. (1969). CLIMATE AND THE OCEAN CIRCULATION: I. THE ATMOSPHERIC CIRCULATION AND THE HYDROLOGY OF THE EARTH'S SURFACE. Monthly Weather Review, 97(11), 739–774. https://doi.org/10.1175/1520-0493(1969)097<0739:CATOC>2.3.CO;2

Manabe, S., & Wetherald, R. T. (1975). The Effects of Doubling the CO2 Concentration on the climate of a General Circulation Model. Journal of the Atmospheric Sciences, 32(1), 3–15. https://doi.org/10.1175/1520-0469(1975)032<0003:TEODTC>2.0.CO;2

Mann, M. E., Bradley, R. S., & Hughes, M. K. (1999). Northern hemisphere temperatures during the past millennium: Inferences, uncertainties, and limitations. Geophysical Research Letters, 26(6), 759–762. https://doi.org/10.1029/1999GL900070

Marcott, S. A., Shakun, J. D., Clark, P. U., & Mix, A. C. (2013). A Reconstruction of Regional and Global Temperature for the Past 11,300 Years. Science, 339(6124), 1198–1201. https://doi.org/10.1126/science.1228026

Masson-Delmotte, V., Hou, S., Ekaykin, A., Jouzel, J., Aristarain, A., Bernardo, R. T., Bromwich, D., Cattani, O., Delmotte, M., Falourd, S., Frezzotti, M., Gallée, H., Genoni, L., Isaksson, E., Landais, A., Helsen, M. M., Hoffmann, G., Lopez, J., Morgan, V., … White, J. W. C. (2008). A Review of Antarctic Surface Snow Isotopic Composition: Observations, Atmospheric Circulation, and Isotopic Modeling. Journal of Climate, 21(13), 3359–3387. https://doi.org/10.1175/2007JCLI2139.1

McDermott, F. (2004). Palaeo-climate reconstruction from stable isotope variations in speleothems: A review. Quaternary Science Reviews, 23(7), 901–918. https://doi.org/10.1016/j.quascirev.2003.06.021

Ming, A., Rowell, I., Lewin, S., Rouse, R., Aubry, T., & Boland, E. (2021). Key messages from the IPCC AR6 climate science report. https://doi.org/10.33774/coe-2021-fj53b

Moerman, J. W., Cobb, K. M., Adkins, J. F., Sodemann, H., Clark, B., & Tuen, A. A. (2013). Diurnal to interannual rainfall δ18O variations in northern Borneo driven by regional hydrology. Earth and Planetary Science Letters, 369–370, 108–119. https://doi.org/10.1016/j.epsl.2013.03.014

Petit, J. R., Jouzel, J., Raynaud, D., Barkov, N. I., Barnola, J.-M., Basile, I., Bender, M., Chappellaz, J., Davis, M., Delaygue, G., Delmotte, M., Kotlyakov, V. M., Legrand, M., Lipenkov, V. Y., Lorius, C., PÉpin, L., Ritz, C., Saltzman, E., & Stievenard, M. (1999). Climate and atmospheric history of the past 420,000 years from the Vostok ice core, Antarctica. Nature, 399(6735), 429–436. https://doi.org/10.1038/20859

Rind, D. (1987). Components of the ice age circulation. Journal of Geophysical Research: Atmospheres, 92(D4), 4241–4281. https://doi.org/10.1029/JD092iD04p04241

Risi, C., Bony, S., & Vimeux, F. (2008). Influence of convective processes on the isotopic composition (δ18O and δD) of precipitation and water vapor in the tropics: 2. Physical interpretation of the amount effect. Journal of Geophysical Research: Atmospheres, 113(D19). https://doi.org/10.1029/2008JD009943

Rozanski, K. (2005). Isotopes in Atmospheric Moisture. In P. K. Aggarwal, J. R. Gat, & K. F. O. Froehlich (Eds.), Isotopes in the Water Cycle (pp. 291–302). Springer-Verlag. https://doi.org/10.1007/1-4020-3023-1_18

Saravana Kumar, U., Kumar, B., Rai, S. P., & Sharma, S. (2010). Stable isotope ratios in precipitation and their relationship with meteorological conditions in the Kumaon Himalayas, India. Journal of Hydrology, 391(1), 1–8. https://doi.org/10.1016/j.jhydrol.2010.06.019

Scheffers, B. R., De Meester, L., Bridge, T. C. L., Hoffmann, A. A., Pandolfi, J. M., Corlett, R. T., Butchart, S. H. M., Pearce-Kelly, P., Kovacs, K. M., Dudgeon, D., Pacifici, M., Rondinini, C., Foden, W. B., Martin, T. G., Mora, C., Bickford, D., & Watson, J. E. M. (2016). The broad footprint of climate change from genes to biomes to people. Science, 354(6313), aaf7671. https://doi.org/10.1126/science.aaf7671

Schiesinger, M. E., & Jiang, X. (1991). Revised projection of future greenhouse warming. Nature, 350(6315), 219–221. https://doi.org/10.1038/350219a0

Schmidt, G. A., Annan, J. D., Bartlein, P. J., Cook, B. I., Guilyardi, E., Hargreaves, J. C., Harrison, S. P., Kageyama, M., LeGrande, A. N., Konecky, B., Lovejoy, S., Mann, M. E., Masson-Delmotte, V., Risi, C., Thompson, D., Timmermann, A., Tremblay, L.-B., & Yiou, P. (2014). Using palaeo-climate comparisons to constrain future projections in CMIP5. Climate of the Past, 10(1), 221–250. https://doi.org/10.5194/cp-10-221-2014

Siler, N., Fiorella, R., & Noone, D. (2021). A Unified Theory of Variability in Precipitation Isotope Ratios. 2021, PP14B-06.

Sluijs, A., van Roij, L., Harrington, G. J., Schouten, S., Sessa, J. A., LeVay, L. J., Reichart, G.-J., & Slomp, C. P. (2014). Warming, euxinia and sea level rise during the Paleocene–Eocene Thermal Maximum on the Gulf Coastal Plain: Implications for ocean oxygenation and nutrient cycling. Climate of the Past, 10(4), 1421–1439. https://doi.org/10.5194/cp-10-1421-2014

Snyder, C. W. (2010). The value of paleoclimate research in our changing climate. Climatic Change, 100(3), 407–418. https://doi.org/10.1007/s10584-010-9842-5

Stern, D. I., & Kaufmann, R. K. (2014). Anthropogenic and natural causes of climate change. Climatic Change, 122(1), 257–269. https://doi.org/10.1007/s10584-013-1007-x

Thomas, C. D. (2010). Climate, climate change and range boundaries. Diversity and Distributions, 16(3), 488–495. https://doi.org/10.1111/j.1472-4642.2010.00642.x

Webster, M., Forest, C., Reilly, J., Babiker, M., Kicklighter, D., Mayer, M., Prinn, R., Sarofim, M., Sokolov, A., Stone, P., & Wang, C. (2003). Uncertainty Analysis of Climate Change and Policy Response. Climatic Change, 61(3), 295–320. https://doi.org/10.1023/B:CLIM.0000004564.09961.9f

Wei, Z., Lee, X., Liu, Z., Seeboonruang, U., Koike, M., & Yoshimura, K. (2018). Influences of large-scale convection and moisture source on monthly precipitation isotope ratios observed in Thailand, Southeast Asia. Earth and Planetary Science Letters, 488, 181–192. https://doi.org/10.1016/j.epsl.2018.02.015

Working Group Members, Technical Summary. In Climate Change 2021: The Physical Science Basis. Contribution of Working Group I to the Sixth Assessment Report of the Intergovernmental Panel on Climate Change [Masson-Delmotte, V., P. Zhai, A. Pirani, S.L. Connors, C. Péan, S. Berger, N. Caud, Y. Chen, L. Goldfarb, M.I. Gomis, M. Huang, K. Leitzell, E. Lonnoy, J.B.R. Matthews, T.K. Maycock, T. Waterfield, O. Yelekçi, R. Yu, and B. Zhou (eds.)]. Cambridge University Press, Cambridge, United Kingdom and New York, NY, USA, pp. 33−144. doi:10.1017/9781009157896.002.

Yao, T., Masson-Delmotte, V., Gao, J., Yu, W., Yang, X., Risi, C., Sturm, C., Werner, M., Zhao, H., He, Y., Ren, W., Tian, L., Shi, C., & Hou, S. (2013). A review of climatic controls on δ18O in precipitation over the Tibetan Plateau: Observations and simulations. Reviews of Geophysics, 51(4), 525–548. https://doi.org/10.1002/rog.20023

Zhou, T. (2021). New physical science behind climate change: What does IPCC AR6 tell us? The Innovation, 2(4), 100173. https://doi.org/10.1016/j.xinn.2021.100173

Chapter 1: A simulation of the mid-Holocene tropical hydrology using the isotope-enabled Community Atmosphere Model: model overview, comparison to speleothem proxies, and insights on interpretation of δ-based proxies.

Kyle Niezgoda
Bronwen Konecky
David Noone

Abstract

The mid-Holocene (MH, 6 ka) is an important period for paleoclimatologists because the boundary conditions of the climate system were not notably different than they are today, which makes the climate changes that occurred during the MH useful in the context of modern climate change. An abundant history of proxy datasets and model simulations has provided for an expansive overview of the climate differences between the MH and the modern day, but key areas remain unclear. One such area is the relationship between proxies of precipitation isotope ratios (δ_p) and the hydroclimate influences that shape isotope ratios, otherwise known as δ_p-climate relationships. In this paper, δ_p-climate relationships during the MH are explored for tropical rainfall with a proxy-guided general circulation modeling approach. Using the isotope-enabled Community Atmosphere Model (iCAM), isotope results from a MH equilibrium climate simulation are compared to a suite of speleothem δ_p proxies from several monsoon and monsoon-influenced tropical locales. Using a best-fit selection technique based on the root-mean-square of model-proxy δ_p errors (RMSE), composite climates are created by averaging the 5% of years with the lowest RMSE. Best-fit composite means are compared to the all-data mean, highlighting climate anomalies that are associated with poor model performance with respect to proxy fit. Best-fit composite means reveal that δ_p-climate relationships are variable in space during the MH. In some regions, model-proxy differences in δ_p are linked to changes in regional atmospheric circulation and nearby oceanic evaporation, whereas in other areas they are linked to changes in local precipitation and evaporation. This methodology provides for model-proxy comparison at the level of climatic structure, i.e. δ_p-climate relationships are explained through the lens of a physically complete climate model. By using a best-fit selection

approach, model development and model-proxy validation is enhanced by revealing not only where the model disagrees with the proxies, but why this is the case as well.

Introduction

The mid-Holocene (6 ka, MH) has served as a benchmark period for understanding insolation-driven variability in the climate system for many decades. The current understanding of the climate anomalies associated with this period stems from model and proxy evidence suggesting that global climate change events occurred between approximately 5 – 8 *kya*, roughly midway between the beginning of the Holocene and the present (Wanner et al., 2008). These changes are most often attributed to changes in the Earth's orbit, with the precession of the Earth's axis of particular importance, resulting in the northern hemisphere (NH) summer closer to the sun during the MH than in the modern day. In effect, this increased incoming solar radiation during the NH summer, resulting in increased global average temperature (Clement et al., 2010).

In the tropics, MH climate change events are often associated with changes to the spatial organization, seasonality, and intensity of the monsoons. Proxy evidence suggesting the presence of stronger and wetter NH monsoons during the MH is abundant, many of which are based on the stable oxygen or hydrogen isotopic composition of precipitation ($\delta^{18}O_p$ and δD_p, or δ_p) (e.g. PAGES2k consortium, 2017; Iso2k [Konecky et al., 2020]). In East Asia, for example, δ_p-based proxies from cave stalagmites (speleothems) generally indicate that MH rainfall was more depleted in ^{18}O (had a lower δ_p value) than the modern (Dykoski et al., 2005; Cosford et al., 2008; Hu et al., 2008; Cai et al., 2010; Dong et al., 2010; Yang et al., 2019). Lower δ_p values suggest increased rainfall amount, a commonly observed anticorrelation that is often dubbed the "amount-effect" (Dansgaard, 1964; Risi et al., 2008; Moerman et al., 2013). While the amount-effect is generally accurate to first order, it is also well known to have complicating factors, and shifts in δ_p from monsoon rainfall proxies are increasingly being thought of from the perspective of regional-scale hydrology (e.g., Rozanski, 2005; Noone at el., 2011). For most monsoons, vapor supply comes from multiple regions with isotopically-distinct evaporation profiles; long-term shifts in the source region can drive shifts in δ_p that are unrelated to

changes in precipitation amount (Aizen et al., 1996; Saravana Kumar et al., 2010; Yao et al., 2013; Wei et al., 2018). This problem is exacerbated by the nature of monsoons as seasonal overturning systems; isotopes of monsoon rainfall are intrinsically bound to the dramatic shifts in atmospheric circulation that occur in concert with monsoon onset and retreat. Monsoon δ_p has been linked to shifts in large-scale tropical atmospheric circulation cells, such as the position of the inter-tropical convergence zone (ITCZ) and the strength of the Hadley cell (Atwood & Sachs, 2014; Sachs et al., 2018; Konecky et al., 2019). Strong convective activity in the region of the ITCZ most often results in rainfall with low δ_p. Monsoon-ITCZ dynamics complicate these matters, and some authors suggest that monsoon location and timing is inherently tied to the seasonal migration of the ITCZ (Fleitmann et al., 2007; Maloney & Shaman, 2008; Nicholoson, 2009; Sachs et al., 2018). Finally, changes in δ_p have been attributed to shifts in ENSO variability through atmospheric teleconnections with the Walker Cell (Cobb et al., 2013; Chen et al., 2016). In this interpretation, paleo-monsoon δ_p is an indicator of global shifts in atmospheric circulation via the meridional Hadley Cell and zonal Walker Cell, empowering the climatological scope of monsoon δ_p.

The MH has been included as a baseline paleoclimate simulation of the Paleoclimate Model Intercomparison Project (PMIP) for several decades (Joussaume et al., 1999; Braconnot et al., 2007a; Braconnot et al., 2012). Now in its 4th iteration (Otto-Bliesner et al., 2017), the synthesis of MH simulations has revealed a few key areas where model results do not align with proxies. These areas are further complicated by the need to translate between proxy space and model space. Traditional output of a general circulation model (GCM) often does not directly match proxy variables. For example, tree ring width is a proxy of precipitation and sunlight, but models do not normally output a tree ring width variable, thus the need for a transformation from proxy space to model space, adding in convoluting errors (Hughes, 2002). Recently, however, many cutting-edge model institutions have implemented an “isotope-enabled” version of their model to directly simulate δ_p. Doing so allows a more direct comparison with model output and δ_p-based proxies and enables the quantification of relationships between atmospheric fields and simulated δ_p, although complications exist when translating from the model’s spatial grid to the specific position of proxies.

Many questions remain about the relationship between δ_p and climate. Answering these questions is critical for interpretation of δ_p-based proxies – without an understanding of the role that climate processes have on δ_p, one fails to accurately reconstruct paleohydrology. To address some of these key unknowns, a new simulation of the MH using the water isotope-enabled Community Atmosphere Model (iCAM), the atmospheric component of the Community Earth System Model v1.2 (CESM) is presented. Particular attention is focused on the tropical hydrology during the MH as it compares to a pre-Industrial control climate simulation. By comparing the MH to the PI, intrinsic linear model biases are removed, and the climate change signals of the MH forcing are isolated specifically. We use the letter Δ to denote MH-PI differences.

Objectives

The following sections aim to answer 2 main questions. First, what is the relationship between zonal- and meridional-mean large-scale atmospheric circulation, and simulated δ_p? Second, how accurately does the model reproduce the proxy-suggested spatial distribution of δ_p, and, as a follow-up, can the cause of large model-proxy discrepancies be explained where they may exist? These goals are accomplished with a 3-pronged approach.

1. An overview of the MH-PI climatology is presented, confirming that model results are a reasonably accurate simulation of the MH anomalies compared to publicly available MH simulations from the PMIP archive.
2. Zonally-averaged $\Delta\delta_p$ is compared to diagnostics of changes to the Walker Cell, and meridionally-averaged $\Delta\delta_p$ with diagnostics of changes to the Hadley Cell, representing the large-scale zonal- and meridional-mean tropical circulations, respectively.
3. A model-proxy comparison analysis between the simulated δ_p and 17 speleothem proxies from the tropics is presented. Among the ensemble of MH simulations, the years with the lowest RMSE for the model minus proxy δ_p difference are selected. From this selection process, climatological factors that influence simulated δ_p by improving model-proxy errors are evaluated.

Methods and materials

Isotope-enabled CESM (iCESM)

This study utilizes an atmosphere-only modeling setup of the Community Earth System Model v 1.2 (CESM 1.2, Hurrell et al. 2013) with isotope-enabled Community Atmosphere Model (iCAM 5, Nusbaumer et al. 2017) and Community Land Model (iCLM 4.5, Lawrence et al. 2011; Wong et al. 2017) active. The grid resolution is nominal 2-degree finite-volume. Isotope-related results from iCESM are well-verified in simulations of the modern climate against the Global Network of Isotopes in Precipitation (GNIP), and iCESM is considered one of the best iGCMs for water isotope simulation (Hu et al., 2018). A total of 200 years are simulated for each simulation; the first 50 are removed to allow ample model spin-up, and the last 150 years are averaged to calculate equilibrium climate states for two experiments: the MH and PI.

The PI run is specified to the CMIP6 DECK experimental design for the pre-Industrial control (Eyring et al. 2016), and uses Hadley Sea Surface Temperatures and Sea Ice extent (HadSST, Deser et al., 2010; Rayner et al., 2003). The MH simulation is also setup in large part by following PMIP4 guidelines (Otto-Bliesner et al. 2016), including orbital parameters and GHG concentrations. The MH simulation uses bias-corrected SSTs from the fully-coupled CCSM4 MH experiment contribution to the PMIP3/CMIP5 database, which are the most recent publicly available MH SSTs from CCSM4, the predecessor to CESM 1.2. MH SSTs are bias-corrected to remove the presence of the "double-ITCZ". CESM bias is calculated by:

$$\textit{CESM SST bias} = \textit{CESM PI SSTs} - \textit{HadSST}$$

Here, the HadSST data is considered the closest approximation to the "observational" PI SSTs. *CESM SST bias* contains the necessary bias correction to remove the double-ITCZ problem. Using the calculated model bias, and assuming that bias is the same in the MH simulations, the equivalent "observational" MH SSTs are calculated by removing the CESM SST bias from the simulated MH SSTs:

$$\textit{"Observational MH SSTs"} = \textit{CCSM4 MH SSTs} - \textit{CESM SST bias}$$

The MH and PI simulations use the above calculated "observational MH SSTs" and the HadSST data set for SSTs, respectively. Somewhat dissimilar to PMIP specifications, the MH simulation includes prescribed vegetation fields for the regions of north Africa and the Arabian Peninsula, approximately mimicking the proxy-suggested floral assemblages of the African Humid Period (AHP, approximately 5-8 kya, Pausata et al. 2020). Vegetation fields are from Tabor et al., 2020; briefly, average PI vegetation conditions from 11°N were extended northward through the Sahara and Arabian peninsula, except where vegetation coverage already exceeded 10%. In both simulations dynamic vegetation is turned off to prevent the death of the prescribed vegetation (C. Tabor, personal communication).

Speleothem proxy records

All speleothem proxy data were downloaded from the National Centers for Environmental Information. Only speleothems in the tropics or in monsoon regions were selected. Additionally, speleothems were required to have $\delta^{18}O$ data at least 100 years before and after 1850 CE and 6ka to allow for a robust measurement. Data were averaged over these 200-year windows, centered on 1850 CE and 6ka, to calculate the PI and MH $\delta^{18}O$. Figure 1 shows the location of all speleothem proxies that met the above criteria, with an accompanying table (Table 1) for metadata and citations.

Results

General overview of MH-PI hydrology

Figure 2 shows the change in 2-meter air temperature (T2m) and precipitation for the annual mean (ANN) and summertime (MJJAS in the NH and NDJFM in the SH) to generally evaluate the model results. Both ΔT2m and ΔP patterns generally resemble the PMIP4 multi model mean (mmm) for most tropical rainfall, with a few minor exceptions (Brierley et al., 2020 fig. 2 for ΔT, fig. 6 for ΔP). In east China and northern SE Asia, our results indicate negative or approximately zero ΔP, whereas the mmm has non-zero, spatially heterogenous ΔP; in mainland SE Asia our results indicate approximate zero change in ΔP, whereas PMIP4 is considerably drier in the MH compared to the PI; and in northern Africa, our positive ΔP contours extend further north compared to PMIP4. Concerning ΔP, considerable change in key

areas in the tropics has been recently highlighted in PMIP4 compared to earlier versions of PMIP. In the PMIP 2 and 3 mmm, ΔP is positive or near zero (depending on the months used to define summer) in the regions of India south of 20° N, east China, and northern SE Asia (Zheng et al., 2013; Jiang et al., 2014; Tian et al., 2018), whereas PMIP4 exhibits a generally drier climate in these regions (Brierley et al., 2020). The PMIP4 mmm is also wetter than PMIP3 in the region of the West African Monsoon. In summary, the model results are consistent with the most recent PMIP ensemble mean, with only a few minor differences.

Figure 3 shows the simulated $\Delta\delta^{18}O_p$ for the same ANN and summertime climatologies from Fig. 2. The annual mean resembles the summertime mean over land tropical oceans, indicating that annual mean $\Delta\delta^{18}O_p$ patterns are driven primarily by summertime $\Delta\delta^{18}O_p$ for both hemispheres. Most of the $\Delta\delta^{18}O_p$ occurs in the NH, with SH changes considerably smaller. Land surfaces tend to have negative $\Delta\delta^{18}O_p$ compared to the positive $\Delta\delta^{18}O_p$ of the oceans, although some exceptions do exist. For example, the northern near-tropical Atlantic Ocean has a band of negative $\Delta\delta^{18}O_p$ off the coast of West Africa; and the Arabian Sea, Bay of Bengal, and West Pacific Warm Pool ocean are weakly depleted. The strongest depletion occurs over northern Africa in the region of the modern day Sahel and Sahara, as well as the southern Arabian peninsula. These negative $\delta^{18}O_p$ anomalies extend through much of Africa and penetrate to approximately 25°N at the most northern extent. Weaker but widespread depletion occurs in India, SE Asia, and western China. At approximately longitude 105°E, the negative contours associated with the largescale depletion near India and SE Asia to the west are weaker.

Figure 4 shows the correlation between the mean simulated $\Delta\delta^{18}O_p$ and ΔP, with average values from each CESM grid point represented by a dot on the figure. Only land units between latitudes 30°S and 30°N are included, and regions are colored to represent shared geography and, in some cases, a single monsoon system. The amount-effect slope for all data is -1.10 ‰ $(\text{mm d}^{-1})^{-1}$, with an r^2 of 0.34. These results indicate that land units that became wetter during the MH (positive ΔP) also tended to have more depletion of isotopes (negative $\Delta\delta^{18}O_p$), and this relationship is relatively consistent across all land units, with 34% of variance in $\Delta\delta^{18}O_p$ explained by variability in ΔP. Slopes and r^2 values for individual regions are closer to zero than

the mean slope (except for the r^2 of the India region, which is 0.39), indicating that amount-effect statistics are strongest over large spatial areas.

The amount effect anticorrelation between $\Delta\delta^{18}O_p$ and ΔP is present in the model simulations, and is a good first-order approximation (i.e. the sign of $\Delta\delta^{18}O_p$ is often the opposite of the sign of ΔP) but minor exceptions exist. In tropical and northern subtropical Africa, for example, the widespread positive ΔP is coupled with an equally-widespread negative $\Delta\delta^{18}O_p$. This widespread depletion anomaly persists over small nearby areas where ΔP (Fig. 4) is negative, e.g. near the Gulf of Guinea. In southern India, negative ΔP persist between the Arabian Sea and the Bay of Bengal, including the southern portion of the continent, but $\Delta\delta^{18}O_p$ is negative over the same region. This behavior demonstrates a common theme among the contours of $\Delta\delta^{18}O_p$ from these simulations – isotopes tend to "smear" rainfall amount anomalies over a larger and more general space. Beyond a first-order approximation, the relationship between $\Delta\delta_p$ and ΔP begins to show its weakness. For example, near lake Chad (15° N, 13° E), rainfall isotopes are depleted by about a further 4‰ during the MH and continental rainfall is increased by 2 mm/day, a ratio of 2 ‰$(mm*d^{-1})^{-1}$. On the other hand, isotopes over the Himalaya are depleted by an additional 2‰, and rainfall is increased by 3 mm/day, a ratio of 0.66 ‰$(mm*d^{-1})^{-1}$. Rainfall isotopes in southern China change by about -0.8 permil, whereas rainfall amount changes are close to zero.

Hadley and Walker circulation relationship to $\Delta\delta^{18}O_p$

Figure 5 shows the MH-PI near-surface mean zonal moisture flux, averaged over the tropics (30S – 30N), with positive numbers indicating westerly moisture transport. There is a clear convergence signal, approximately bounded by longitudes 325 on the west and 130 on the east. Within these longitudes, net moisture convergence anomalies occur, and moisture divergence anomalies occur outside these longitudes. This indicates a clear signal of enhanced moisture flux from the general Pacific and Atlantic oceans, onto tropical Africa, Asia, and the Indian Ocean. This divergence pattern, centered in the central tropical Pacific, resembles a "Niña-like" response in the atmosphere, or a westward shift in the Walker Cell, despite forcing our model with SSTs that are in the neutral phase of the El Nino Southern Oscillation (ENSO),

the main mode of climate variability linked to shifts in the Walker Cell. This suggests an ENSO-like atmospheric response in the Walker circulation to MH forcing. A Niña-like mean-state shift and a reduction in ENSO variability, is thought to have occurred during the MH (Cobb et al., 2013), which is supported by the Walker anomalies shown here. Additionally, the thin blue line shows the meridional mean, amount-weighted $\Delta\delta^{18}O_p$, plotted along the same longitudes, for all precipitation (oceanic and continental). Regions of convergence correspond to regions of low isotope ratio, and vice versa, suggesting a Walker circulation-control on $\Delta\delta^{18}O_p$ at the zonal mean.

To approximate the influence of the Hadley circulation on tropical $\Delta\delta^{18}O_p$, the seasonal cycle of the latitude of the center of the ITCZ is calculated, which is shown in figure 6. Following the methodology of Kang & Polvani, (2010), the zero-crossings of the 500 mb zonal mean meridional streamfunction, ψ_{500}, are used to denote the edges of the Hadley cells. Moving north from the south pole, the first zero-crossing represents the southern edge of the SH Hadley cell, the second represents the center of the ITCZ, and the third represents the northern edge of the NH Hadley cell. Thus, the latitude at the middle zero-crossing of ψ_{500} is the approximate center of the ITCZ. Figure 5a shows a plot of ψ_{500} over several NH summertime months for the MH (dashed lines) and PI (solid lines). During these months, the southern Hadley cell is the main cell, which is located at the minima of the ψ_{500} curves, centered around the equator. Moving north, the southern cell weakens until the zero-crossing is reached, denoting the ITCZ. In all months, the ITCZ is positioned further north in the MH than the PI. In addition, the PI ITCZ position lags the MH by a month during the NH spring, summer, and fall, i.e. the MH ITCZ reaches approximate latitude 20°N in June, whereas the PI doesn't get that far north until July. At their most northern position, the MH ITCZ is situated 5° further north than the PI. Figure 6b shows the position of the ITCZ over the seasonal cycle (the latitude of the middle zero-crossing for each month), further demonstrating the lagging PI ITCZ as well as the 5° northward-shifted maximum position during the NH summer.

Figure 7 shows Hovmöller diagrams in latitude and time of the zonal mean $\Delta\delta^{18}O_p$, averaged over longitudes 0° - 180°, with the ITCZ position. These longitudes encapsulate roughly the "convergence zone" (fig. 5), or the general continental regions of Africa, the Middle

East, India, and East and SE Asia. Large negative values of $\delta^{18}O_p$ appear to roughly follow the ITCZ position in both the PI and MH (fig 7A). Concerning the MH-PI, shown in fig. 7B, $\Delta\delta^{18}O_p$ contours are shifted north during the NH summer, in concert with the northward-shifted ITCZ. In NH non-summer months, the position of the ITCZ during the MH is not discernibly different from the PI, and the $\Delta\delta^{18}O_p$ contours are consequently near zero. Negative contours of $\Delta\delta^{18}O_p$ do not reach the northern extent of the MH ITCZ until September-October, which occurs after the timing of the northernmost position of the MH ITCZ, suggesting a lag between the $\Delta\delta^{18}O_p$ response and the timing of the ITCZ in northern latitudes. Figure 8 shows the same diagram as fig, 7, but averaged over longitudes 180° - 360° instead. These longitudes generally encompass the Pacific and Atlantic Oceans, or roughly the "divergence zone" from fig. 5. While isotopes seem to follow the ITCZ position (fig 8A) as they did in fig. 7, $\Delta\delta^{18}O_p$ is not as strongly shifted northward during the NH summer.

Model-proxy comparison

The model-proxy comparison for water isotopes compares precipitation isotopes from the model ($\delta^{18}O_p$) directly to the speleothem calcite oxygen isotope ratio ($\delta^{18}O_{calcite}$). The transformation from $\delta^{18}O_p$ to $\delta^{18}O_{calcite}$ is impacted by two fractionating steps. 1) rainfall hitting the surface percolates into the surface and eventually becomes cave drip water (DW). DW has a selection bias for low-intensity rainfall because surface water runoff increases during high intensity precipitation events, reducing the fraction of total P that becomes DW. Likewise, $\delta^{18}O_{DW}$ is biased towards the average $\delta^{18}O_p$ from low-intensity P events (Hu et al., 2021). 2) DW H_2O is incorporated into the speleothem calcite minerology, which is a temperature dependent fractionation (Baker et al., 2013; Wong and Breecker, 2015). Figure 9 shows the correlation between changes in the 10cm soil water (SW) and precipitation isotope ratio. The presence of an intensity bias in soil water isotope ratio would manifest as significant and consistent deviations from the 1:1 line, shown in black, but the correlation suggests a good fit. Relative humidity change appears to play a role in the rainfall-SW differences, with $\Delta\delta^{18}O_{SW\text{-}10cm}$ more positive than $\Delta\delta^{18}O_p$ in areas with increased RH (blue dots), and more negative in areas with decreased RH (red dots). RH acts as the mediator of the fractionation of evaporation acting on

surface waters. In the high-ΔRH case (the red dots), fractionating effects during evaporation on standing water are strong, resulting in enrichment of standing water compared to the precipitation that created it. The opposite is true for the low-ΔRH case. In summary, the good fit between $\Delta\delta^{18}O_{SW}$ and $\Delta\delta^{18}O_p$ indicates that $\Delta\delta^{18}O_p$ is a sufficiently good approximation of cave drip water isotope ratio.

Figures 10 and 11 characterize the model-speleothem proxy $\delta^{18}O$ comparison. Figure 10 shows the iCAM simulated annual mean, amount-weighted PI $\delta^{18}O_p$ and $\Delta\delta^{18}O_p$ (as in fig. 3, with different color bar limits), with the 17 speleothem $\delta^{18}O$ values overlain as circles. Model-proxy differences in are larger for the PI climate than for the MH-PI difference, indicating that biases exist in the mean climates that are removed when calculating Δs. In 13 out of 17 speleothem locations, the sign of simulated $\Delta\delta^{18}O_p$ matches the sign of the proxy $\Delta\delta^{18}O$. Standout areas of model-proxy mismatch are in the speleothems from Northwest Africa, where simulated $\Delta\delta^{18}O_p$ contours form a zonally-aligned band of positive $\Delta\delta18O_p$, buttressed on the north and south by negative $\Delta\delta18O_p$, but the two speleothem $\Delta\delta^{18}O$ records, Chaara (2) and Wintimdouine (3), suggest moderate to strong depletion.

Figure 11 shows histograms of simulated annual mean $\Delta\delta^{18}O_p$, with proxy speleothem $\Delta\delta^{18}O$ values included as vertical dashed bars. Green dots indicate the simulated mean $\Delta\delta^{18}O_p$, and horizontal bars extending from the green dots show +- $2\sigma^2$, or the approximate 95% confidence interval on the histogram mean. Histograms were constructed using every possible MH-PI year pairing for years 51-200 from the equilibrium simulations, i.e. $\Delta\delta^{18}O_p$ for MH year 51 minus PI year 51, 52, 53, …, 200, MH year 52 minus PI year 51, 52, 53, …, 200, and so forth, for a total of 150^2 year-pairings. Despite good first-order model-proxy agreement, less success is found in the model's ability to accurately simulate the proxy-predicted magnitude of $\Delta\delta^{18}O$. In only 5 of 17 speleothems do the 95% confidence intervals of the model mean $\Delta\delta^{18}O_p$ intersect the proxy $\Delta\delta^{18}O$ value.

Best-fit composite analysis

Each post-spin up year from an equilibrium general circulation model simulation can be thought of like an ensemble member, in that year-to-year similarity is low. The ability for iCAM

(or any atmospheric model) to "remember" previous climate states is very low. In other words, individual years of an equilibrium simulation are statistically independent samples of the true equilibrium mean. The histograms in fig. 11 demonstrate that, while simulated $\Delta\delta^{18}O_p$ is often poorly representative of proxy $\Delta\delta^{18}O$, there are years in which the simulated difference is more similar to the proxy difference than others. In order to better understand the cause of model-proxy discrepancies, the following question is posed: what does the model "look like" during those years when model-proxy errors are low?

To answer this, the best-fit composite climate state was identified and compared to the overall climate. Best-fit composites were identified (or created, etc.) by computing the root-mean-square of the $\Delta\delta_{model}$ - $\Delta\delta_{proxy}$ errors (RMSE) for all 17 speleothems, and for each possible MH-PI year pairing ($N = 150^2$). The first 5% (N = 1125) of year pairings, ordered from low to high RMSE, were selected, which are referred to as the best-fit composite. Doing so creates a climatology that preferentially selects the model years in which the $\Delta\delta_{model}$ most closely resembles $\Delta\delta_{proxy}$.

Results of the best-fit composite approach begin with figure 12, which shows $\Delta\delta^{18}O_p$ and ΔP contours for the A&D) best-fit composite mean, B&E) all data mean, and C&F) best-fit minus all data difference. Together with figure 13, this demonstrates the function of the best-fit composite approach: the best-fit is forced to have the lowest model-proxy RMSE, which is evident in the isotope results. To denote the difference between the best-fit composite mean and the all data mean, which are themselves differences, the symbol Δ' is used, i.e. $\Delta'\delta^{18}O_p$ is equal to [best fit composite mean $\Delta\delta^{18}O_p$] – [all data mean $\Delta\delta^{18}O_p$]. $\Delta'\delta^{18}O_p$ is positive in India and the southern Arabian peninsula, which corrects the over depletion of Qunf (4) $\Delta\delta^{18}O$ in the all data mean; negative in northwest Africa, which corrects the original large model-proxy error for Chaara (2) and Wintimdouine (3); negative in east China, correcting the under-depletion of all Chinese speleothems; and positive in North Australia, correcting the under-enrichment of the KNI speleothem location. Overall general improvement is shown in figure 13 as the red dots (best fit composite mean) vs. green dots (all data mean, as in fig. 10). In East China and India, these $\Delta'\delta$ changes are accompanied by anticorrelated shifts in $\Delta'P$, shown in figure 12 D-F.

However, in northwest African and northern Australia, there is very little Δ'P shift despite large shifts in $\Delta'\delta^{18}O_p$, suggesting a non-amount-effect control on $\Delta\delta^{18}O_p$ in those regions.

Figures 14 – 16 show 6 additional climate variables for the best-fit composite mean, all data mean, and the Δ' difference. A narrative overview of the results found in these figures on a region-by region basis is presented below, covering east China, northwest Africa, India and the Arabian peninsula (focusing on the region of the Qunf cave in Oman), and finally northern Australia.

East China best-fit composite mean climatology

Figure 14 shows Δ' for 2 meter air temperature (T2m) and sea-level pressure (PSL) with column integrated vapor transport (IVT, as barbs). The Δ'PSL and Δ'IVT results suggest that increases in east China precipitation (fig. 12) are influenced by increased IVT from the nearby Pacific onto the Asian continent, forced by an anomalous high pressure cell directly offshore of east China. This suggest non-monsoonal precipitation increases on east China – an intensification of monsoon circulation in east China would be associated with a decrease in PSL over the East Asian continent, but Δ'PSL is higher. In fact, IVT direction in most of eastern China is offshore; the increases in IVT blows onshore near the east coast of Vietnam at approximately 15°N, which then turns northward towards east China. This is reminiscent of shoulder season rainfall patterns in east and southeast China, but the high pressure over the continent makes linking the Δ'IVT to a change in monsoon intensification difficult. Figure 15 shows Δ' of evaporation (right) and evaporation isotope ratio (left), $\delta^{18}O_E$. These figures further connect the nearby Pacific ocean to increased rainfall and more depleted isotope ratios, by linking the enhanced Pacific-to-east China IVT with an initial-condition increase in nearshore Pacific Ocean evaporation. Finally, Figure 16 shows the Δ' of vapor isotope ratio ($\delta^{18}O_v$) and 500 hPa vertical velocity (ω_{500}). Combined, a diagram of what drives the negative $\Delta'\delta^{18}O_p$ is apparent: increased evaporative flux in the nearby Pacific provides increased IVT onto east China via onshore winds near latitude 15°N. The enhanced convergence increases vapor availability, and increased negative (upward) vertical velocity, ω_{500}, over east China increases the potential for deep convective activity, which results in increased rainfall amount. Increases in deep convective

activity and associated increases in precipitation amount results in the negative $\Delta'\delta^{18}O_p$ found in eastern China.

Northwest Africa best-fit composite mean climatology

Northwest African $\Delta'\delta^{18}O_p$ is negative, but $\Delta'P$ does not change. Likewise, $\Delta'T2m$ and $\Delta'IVT$ are also near-zero. However, $\Delta'PSL$ is negative, and notable increases in evaporation amount are found over the land surface and nearby coastal Atlantic, similar in magnitude to the $\Delta'E$ in the nearby Pacific for east China. $\Delta'\delta^{18}O_E$ is negative as well, although this is not surprising – a common relationship in iCAM is the consistent similarity between $\delta_{evaporation}$ and $\delta_{precipitation}$. $\Delta'\delta^{18}O_{vapor}$ is near zero, despite non-zero changes in $\Delta'\delta^{18}O_p$ and $\Delta'\delta18O_E$. This indicates that precipitation is strongly locally sourced, such that whatever is put in by evaporation is removed quickly by precipitation, resulting in no change in vapor isotope ratio. Finally, $\Delta'\omega_{500}$ is negative, indicating increased upward vertical velocity. Combined, increased upward vertical velocity and decreased pressure suggest stronger convective activity, and increases in $\Delta'E$ alongside decreases in $\Delta'\delta^{18}O_E$ and $\Delta'\delta^{18}O_p$ suggest an increase in locally sourced vapor.

Oman (Qunf cave) best-fit composite mean climatology

$\Delta'\delta^{18}O_p$ is positive in the region of the Qunf cave, which improves the slight over-depletion seen in fig. 11. $\Delta'P$ is negative and $\Delta'T$ is positive in this region, with little change in local $\Delta'IVT$, although there is a strong southerly influence in the nearby Indian Ocean. $\Delta'E$ is negative and $\Delta'\delta^{18}O_E$ is positive, indicating that local evapotranspiration is reduced in the best fit composite, and that the evaporation is more enriched. In the best-fit composite and all data means (subfigures A, B, D, and E), this region is one of increased evaporative flux and more negative evaporation isotope ratio, suggesting that the all data mean is evaporating too much and the isotope ratio of evaporation is too low. There is little change in $\Delta'\omega_{500}$, suggesting that no change in atmospheric instability exists. The result is twofold: first, $\Delta'E$ is negative and $\Delta\delta^{18}O_{vapor}$ is negative, which results in a decrease in a depleted source of vapor. Second, the $\Delta'\delta^{18}O_{vapor}$ itself increases, which makes the evaporation that does occur provide more isotopically positive vapor to the atmosphere. Negative $\Delta'P$ is probably associated with reduced

cloudiness, as T2m is well correlated with approximations of cloudiness in these iCAM results (not shown). In conclusion, positive $\Delta'\delta^{18}O_p$ at Qunf is driven by weakened evaporation, and less negative $\Delta\delta^{18}O_E$.

Northern Australia best-fit composite mean climatology

Results from northern Australia are similar to Qunf. Positive $\Delta'\delta^{18}O_p$ occurs alongside positive $\Delta'T$, and positive $\Delta'\delta^{18}O_E$. The only difference is a near-zero $\Delta'E$, whereas Qunf had a large negative $\Delta'E$. However, unlike at Qunf, the best-fit and all data mean $\Delta\delta^{18}O_E$ are also near-zero for northern Australia (i.e. Fig. 15A and B), and so changes in evaporation amount are not important for this region. Put another way, because the $\Delta\delta^{18}O_E$ for all data and best fit is approximately zero (Figs 15A and B), it doesn't matter if evaporation amount increases or decreases, because such changes will supply the atmosphere with evaporation with a $\Delta\delta^{18}O_E$, = 0‰, which will have no effect on $\Delta\delta^{18}O_{vapor}$. In summary, northern Australia experiences positive $\Delta'\delta^{18}O_p$ because the isotope ratio of evaporation increases.

Discussion

Several well-known MH tropical climate anomalies were present in our model simulations, suggesting good overall model validation (fig. 2, 5, and 6). When spatially averaged, rainfall isotope ratios appear to be related to shifts in both large scale zonal (i.e. the Walker Cell) and meridional (the Hadley Cell) atmospheric circulation. A quasi-nina-like mean state shift in the atmosphere suggested a controlling influence on land-based isotope ratios by means of large-scale convergence. In the oceanic sector (i.e. the Pacific and Atlantic), widespread zonal divergence anomalies were present, whereas in the continental sector (i.e. Africa and Asia) zonal convergence anomalies were found. Likewise, in the divergence zone, isotope of rainfall were enriched, and in the convergence zone, depleted. In the meridional direction, it was seen that the MH ITCZ is shifted north by approximate 5° at its northernmost extent, and leads the PI ITCZ by at least a month in the NH summer. This shift coincides with a northward shift in depleted isotope ratios in the continental sector, between longitudes 0° and 180°; but in the oceanic sector, between longitudes 180° and 360°, the northward shift was weaker. This suggests an isotopic response to the interaction between monsoons and the ITCZ

– as the ITCZ shifts north, so too does the location of intense monsoon rainfall. Thus, large-scale spatial patterns of tropical precipitation isotope ratios have the potential to provide information on large-scale patterns of zonal and meridional atmospheric circulation. Results here highlight the potential benefit for specifically manipulation the location, timing, and strength of meridional and zonal overturning via fored numerical experiments to help constrain or otherwise address poorly understood uncertainty about the relationship between large-scale overturning circulation and local monsoon isotope ratios.

To first order, model-proxy validation is good, and the model more often than not captures the sign of $\Delta\delta_p$. At higher orders, dissimilarities between the model results and proxies become more evident. For instance, although the correct negative sign for the simulated $\Delta\delta_p$ over eastern China was achieved, proxy $\Delta\delta_p$ were far more negative than the simulated fields, indicating that the model underestimated $\Delta\delta_p$ for this region, despite getting the right sign.

The best-fit approach highlighted areas in which the all-data model run was faltering. For example, eastern China precipitation was increased by increased onshore vapor transport, increased upward vertical velocity, and increased regional evaporation. This was all forced by the presence of a high pressure anomaly over China and in the nearby Pacific, suggesting that the all-data simulation is producing too-low pressures in the deep continental interior. This is surprising considering that increased rainfall in eastern China is typically associated with increased monsoon strength, however this result indicates that by weakening the ocean-land pressure gradient, east China rainfall increases.

The best-fit approach highlights the role of vegetation in north African and the Arabian Peninsula. This induced vegetation field for the MH simulation extends PI vegetation northward throughout the Sahara and Arabian Peninsula. In northwest Africa, simulated $\Delta\delta_p$ contours are too enriched. Using the best-fit approach, this was revealed to be related to too little and too enriched evapotranspiration in northwestern Africa. By increasing the amount of and depleting the isotope ratio of the evaporative flux in the best-fit composite mean, this resulted in more depleted isotope ratios, reducing the model-proxy discrepancy. Perhaps the vegetation fields are not accurate for this region, and more vegetation is necessary to increase evaporative

loading to the necessary rates. Additionally, no changes are made to the dust loading of the atmosphere, but some authors have suggested is necessary to accurately simulate the African Humid Period of the MH (Pausata et al., 2017; Thompson et al., 2019). This could result in further model-proxy improvements by increase rainfall even further. In Qunf, however, the story is the opposite. The all data model results suggest that too much evaporation is occurring, and that the evaporation is too depleted. In the best-fit composite mean, less evaporation occurs and it is more enriched, which results in more enriched precipitation isotope ratios, improving model-proxy accuracy. This could indicate that the vegetation fields extending into the Arabian Peninsula is an inaccurate estimate of vegetative expanse, because removing vegetation and returning to the deserted land surface of the PI simulation would reduce evapotranspiration dramatically and increase the isotope ratio of said evaporation, which would likely drive increased $\Delta\delta_p$.

While useful, the best-fit approach is a narrative depiction of the role of various climactic phenomenon on precipitation isotopes. Further work is needed to quantify the effect of these variables. For instance, by experimentally inducing the SW-NE oriented pressure anomaly in eastern China and the north Pacific (fig. 14C), do the isotope ratios of eastern China become more depleted? If so, this provides the possibility to interpret the Chinese speleothems as indicators of shifts in north Pacific pressure anomalies, and related circulation patterns. Nonetheless, these results indicate that the all-data MH simulation is generally underestimating the climate response, because the best-fit composite climate usually makes the pre-existing climate changes stronger. Put another way, the simulated precipitation response to MH forcing is dampened relative to what the proxies suggest. While not universally true, this finding indicates that precipitation results of paleoclimate simulations using CESM most likely underestimate the expected signal, and that extrapolating the model to warmer climates than the modern may carry these insufficiencies.

Bibliography

Ait Brahim, Y., Wassenburg, J. A., Sha, L., Cruz, F. W., Deininger, M., Sifeddine, A., Bouchaou, L., Spötl, C., Edwards, R. L., & Cheng, H. (2019). North Atlantic Ice-Rafting, Ocean and Atmospheric Circulation During the Holocene: Insights From Western Mediterranean Speleothems. In Geophysical Research Letters (Vol. 46, Issue 13, pp. 7614–7623). American Geophysical Union (AGU). https://doi.org/10.1029/2019gl082405

Aizen, V., Aizen, E., Melack, J., & Martma, T. (1996). Isotopic measurements of precipitation on central Asian glaciers (southeastern Tibet, northern Himalayas, central Tien Shan). *Journal of Geophysical Research: Atmospheres*, *101*(D4), 9185–9196. https://doi.org/10.1029/96JD00061

Andrews, J. E., Carolin, S. A., Peckover, E. N., Marca, A., Al-Omari, S., & Rowe, P. J. (2020). Holocene stable isotope record of insolation and rapid climate change in a stalagmite from the Zagros of Iran. *Quaternary Science Reviews*, *241*, 106433. https://doi.org/10.1016/j.quascirev.2020.106433

Atwood, A. R., & Sachs, J. P. (2014). Separating ITCZ- and ENSO-related rainfall changes in the Galápagos over the last 3 kyr using D/H ratios of multiple lipid biomarkers. *Earth and Planetary Science Letters*, *404*, 408–419. https://doi.org/10.1016/j.epsl.2014.07.038

Ayliffe, L. K., Gagan, M. K., Zhao, J., Drysdale, R. N., Hellstrom, J. C., Hantoro, W. S., Griffiths, M. L., Scott-Gagan, H., Pierre, E. S., Cowley, J. A., & Suwargadi, B. W. (2013). Rapid interhemispheric climate links via the Australasian monsoon during the last deglaciation. *Nature Communications*, *4*(1), 2908. https://doi.org/10.1038/ncomms3908

Baker, A., Bradley, C., & Phipps, S. J. (2013). Hydrological modeling of stalagmite δ18O response to glacial-interglacial transitions. *Geophysical Research Letters*, *40*(12), 3207–3212. https://doi.org/10.1002/grl.50555

Braconnot, P., Harrison, S. P., Kageyama, M., Bartlein, P. J., Masson-Delmotte, V., Abe-Ouchi, A., Otto-Bliesner, B., & Zhao, Y. (2012). Evaluation of climate models using palaeoclimatic data. *Nature Climate Change*, *2*(6), 417–424. https://doi.org/10.1038/nclimate1456

Braconnot, P., Otto-Bliesner, B., Harrison, S., Joussaume, S., Peterchmitt, J.-Y., Abe-Ouchi, A., Crucifix, M., Driesschaert, E., Fichefet, Th., Hewitt, C. D., Kageyama, M., Kitoh, A., Laîné, A., Loutre, M.-F., Marti, O., Merkel, U., Ramstein, G., Valdes, P., Weber, S. L., … Zhao, Y. (2007). Results of PMIP2 coupled simulations of the Mid-Holocene and Last Glacial Maximum – Part 1: Experiments and large-scale features. *Clim. Past*, *3*(2), 261–277. https://doi.org/10.5194/cp-3-261-2007

Brierley, C. M., Zhao, A., Harrison, S. P., Braconnot, P., Williams, C. J. R., Thornalley, D. J. R., Shi, X., Peterschmitt, J.-Y., Ohgaito, R., Kaufman, D. S., Kageyama, M., Hargreaves, J. C., Erb, M. P., Emile-Geay, J., D'Agostino, R., Chandan, D., Carré, M., Bartlein, P. J., Zheng, W., … Abe-Ouchi, A. (2020). Large-scale features and evaluation of the PMIP4-CMIP6 *midHolocene* simulations. *Climate of the Past*, *16*(5), 1847–1872. https://doi.org/10.5194/cp-16-1847-2020

Cai, Y., Tan, L., Cheng, H., An, Z., Edwards, R. L., Kelly, M. J., Kong, X., & Wang, X. (2010). The variation of summer monsoon precipitation in central China since the last deglaciation. *Earth and Planetary Science Letters*, *291*(1), 21–31. https://doi.org/10.1016/j.epsl.2009.12.039

Chen, S., Hoffmann, S. S., Lund, D. C., Cobb, K. M., Emile-Geay, J., & Adkins, J. F. (2016). A high-resolution speleothem record of western equatorial Pacific rainfall: Implications for Holocene ENSO evolution. *Earth and Planetary Science Letters*, *442*, 61–71. https://doi.org/10.1016/j.epsl.2016.02.050

Clement, A. C., Seager, R., & Cane, M. A. (2000). Suppression of El Niño during the Mid-Holocene by changes in the Earth's orbit. *Paleoceanography*, *15*(6), 731–737. https://doi.org/10.1029/1999PA000466

Cobb, K. M., Westphal, N., Sayani, H. R., Watson, J. T., Di Lorenzo, E., Cheng, H., Edwards, R. L., & Charles, C. D. (2013). Highly Variable El Niño–Southern Oscillation Throughout the Holocene. *Science*, *339*(6115), 67–70. https://doi.org/10.1126/science.1228246

Cosford, J., Qing, H., Eglington, B., Mattey, D., Yuan, D., Zhang, M., & Cheng, H. (2008). East Asian monsoon variability since the Mid-Holocene recorded in a high-resolution, absolute-dated aragonite speleothem from eastern China. *Earth and Planetary Science Letters*, *275*(3), 296–307. https://doi.org/10.1016/j.epsl.2008.08.018

Cruz, F. W., Burns, S. J., Karmann, I., Sharp, W. D., Vuille, M., Cardoso, A. O., Ferrari, J. A., Silva Dias, P. L., & Viana, O. (2005). Insolation-driven changes in atmospheric circulation over the past 116,000 years in subtropical Brazil. *Nature*, *434*(7029), 63–66. https://doi.org/10.1038/nature03365

Cruz, F. W., Vuille, M., Burns, S. J., Wang, X., Cheng, H., Werner, M., Lawrence Edwards, R., Karmann, I., Auler, A. S., & Nguyen, H. (2009). Orbitally driven east–west antiphasing of South American precipitation. *Nature Geoscience*, *2*(3), 210–214. https://doi.org/10.1038/ngeo444

Dansgaard, W. (1964). Stable isotopes in precipitation. *Tellus*, *16*(4), 436–468. https://doi.org/10.3402/tellusa.v16i4.8993

Denniston, R. F., Ummenhofer, C. C., Wanamaker, A. D., Lachniet, M. S., Villarini, G., Asmerom, Y., Polyak, V. J., Passaro, K. J., Cugley, J., Woods, D., & Humphreys, W. F. (2016). Expansion and Contraction of the Indo-Pacific Tropical Rain Belt over the Last Three Millennia. *Scientific Reports*, *6*(1), 34485. https://doi.org/10.1038/srep34485

Deser, C., Phillips, A. S., & Alexander, M. A. (2010). Twentieth century tropical sea surface temperature trends revisited. *Geophysical Research Letters*, *37*(10). https://doi.org/10.1029/2010GL043321

Dong, J., Wang, Y., Cheng, H., Hardt, B., Edwards, R. L., Kong, X., Wu, J., Chen, S., Liu, D., Jiang, X., & Zhao, K. (2010). A high-resolution stalagmite record of the Holocene East Asian monsoon from Mt Shennongjia, central China. *The Holocene*, *20*(2), 257–264. https://doi.org/10.1177/0959683609350393

Dykoski, C. A., Edwards, R. L., Cheng, H., Yuan, D., Cai, Y., Zhang, M., Lin, Y., Qing, J., An, Z., & Revenaugh, J. (2005). A high-resolution, absolute-dated Holocene and deglacial Asian monsoon record from Dongge Cave, China. *Earth and Planetary Science Letters*, *233*(1), 71–86. https://doi.org/10.1016/j.epsl.2005.01.036

Eyring, V., Bony, S., Meehl, G. A., Senior, C. A., Stevens, B., Stouffer, R. J., & Taylor, K. E. (2016). Overview of the Coupled Model Intercomparison Project Phase 6 (CMIP6) experimental design and organization. *Geoscientific Model Development*, *9*(5), 1937–1958. https://doi.org/10.5194/gmd-9-1937-2016

Fleitmann, D., Burns, S. J., Mudelsee, M., Neff, U., Kramers, J., Mangini, A., & Matter, A. (2003). Holocene Forcing of the Indian Monsoon Recorded in a Stalagmite from Southern Oman. In Science (Vol. 300, Issue 5626, pp. 1737–1739). American Association for the Advancement of Science (AAAS). https://doi.org/10.1126/science.1083130

Fleitmann, D., Burns, S. J., Mangini, A., Mudelsee, M., Kramers, J., Villa, I., Neff, U., Al-Subbary, A. A., Buettner, A., Hippler, D., & Matter, A. (2007). Holocene ITCZ and Indian monsoon dynamics recorded in stalagmites from Oman and Yemen (Socotra). *Quaternary Science Reviews*, *26*(1), 170–188. https://doi.org/10.1016/j.quascirev.2006.04.012

Frumkin, A., Ford, D. C., & Schwarcz, H. P. (1999). Continental Oxygen Isotopic Record of the Last 170,000 Years in Jerusalem. *Quaternary Research*, *51*(3), 317–327. https://doi.org/10.1006/qres.1998.2031

Holmgren, K., Lee-Thorp, J. A., Cooper, G. R. J., Lundblad, K., Partridge, T. C., Scott, L., Sithaldeen, R., Siep Talma, A., & Tyson, P. D. (2003). Persistent millennial-scale climatic variability over the past 25,000 years in Southern Africa. *Quaternary Science Reviews*, *22*(21), 2311–2326. https://doi.org/10.1016/S0277-3791(03)00204-X

Hu, C., Henderson, G. M., Huang, J., Xie, S., Sun, Y., & Johnson, K. R. (2008). Quantification of Holocene Asian monsoon rainfall from spatially separated cave records. *Earth and Planetary Science Letters*, *266*(3), 221–232. https://doi.org/10.1016/j.epsl.2007.10.015

Hu, J., Dee, S. G., Wong, C. I., Harman, C. J., Banner, J. L., & Bunnell, K. E. (2021). Assessing proxy system models of cave dripwater δ18O variability. *Quaternary Science Reviews*, *254*, 106799. https://doi.org/10.1016/j.quascirev.2021.106799

Hu, J., Emile-Geay, J., Nusbaumer, J., & Noone, D. (2018). Impact of Convective Activity on Precipitation δ18O in Isotope-Enabled General Circulation Models. *Journal of Geophysical Research: Atmospheres*, *123*(23), 13,595-13,610. https://doi.org/10.1029/2018JD029187

Hughes, M. K. (2002). Dendrochronology in climatology – the state of the art. *Dendrochronologia*, *20*(1), 95–116. https://doi.org/10.1078/1125-7865-00011

Hurrell, J. W., Holland, M. M., Gent, P. R., Ghan, S., Kay, J. E., Kushner, P. J., Lamarque, J.-F., Large, W. G., Lawrence, D., Lindsay, K., Lipscomb, W. H., Long, M. C., Mahowald, N., Marsh, D. R., Neale, R. B., Rasch, P., Vavrus, S., Vertenstein, M., Bader, D., … Marshall, S. (2013). The Community Earth System Model: A Framework for Collaborative Research. *Bulletin of the American Meteorological Society*, *94*(9), 1339–1360. https://doi.org/10.1175/BAMS-D-12-00121.1

Jiang, D., Tian, Z., & Lang, X. (2015). Mid-Holocene global monsoon area and precipitation from PMIP simulations. *Climate Dynamics*, *44*(9), 2493–2512. https://doi.org/10.1007/s00382-014-2175-8

Joussaume, S., Taylor, K. E., Braconnot, P., Mitchell, J. F. B., Kutzbach, J. E., Harrison, S. P., Prentice, I. C., Broccoli, A. J., Abe-Ouchi, A., Bartlein, P. J., Bonfils, C., Dong, B., Guiot, J., Herterich, K., Hewitt, C. D., Jolly, D., Kim, J. W., Kislov, A., Kitoh, A., … Wyputta, U. (1999). Monsoon changes for 6000 years ago: Results of 18 simulations from the Paleoclimate Modeling Intercomparison Project (PMIP). *Geophysical Research Letters*, *26*(7), 859–862. https://doi.org/10.1029/1999GL900126

Kang, S. M., & Polvani, L. M. (2010). The Interannual Relationship between the Latitude of the Eddy-Driven Jet and the Edge of the Hadley Cell. *Journal of Climate*, *24*(2), 563–568. https://doi.org/10.1175/2010JCLI4077.1

Konecky, B. L., McKay, N. P., Churakova (Sidorova), O. V., Comas-Bru, L., Dassié, E. P., DeLong, K. L., Falster, G. M., Fischer, M. J., Jones, M. D., Jonkers, L., Kaufman, D. S., Leduc, G., Managave, S. R., Martrat, B., Opel, T., Orsi, A. J., Partin, J. W., Sayani, H. R., Thomas, E. K., … Iso2k Project Members. (2020). The Iso2k database: A global compilation of paleo-$\delta^{18}O$ and $\delta^{2}H$ records to aid understanding of Common Era climate. *Earth System Science Data*, *12*(3), 2261–2288. https://doi.org/10.5194/essd-12-2261-2020

Konecky, B. L., Noone, D. C., & Cobb, K. M. (n.d.). The Influence of Competing Hydroclimate Processes on Stable Isotope Ratios in Tropical Rainfall. *Geophysical Research Letters*, *0*(0). https://doi.org/10.1029/2018GL080188

Lawrence, D. M., Oleson, K. W., Flanner, M. G., Thornton, P. E., Swenson, S. C., Lawrence, P. J., Zeng, X., Yang, Z.-L., Levis, S., Sakaguchi, K., Bonan, G. B., & Slater, A. G. (2011). Parameterization improvements and functional and structural advances in Version 4 of the Community Land Model. *Journal of Advances in Modeling Earth Systems*, *3*(1). https://doi.org/10.1029/2011MS00045

Maloney, E. D., & Shaman, J. (2008). Intraseasonal Variability of the West African Monsoon and Atlantic ITCZ. In Journal of Climate (Vol. 21, Issue 12, pp. 2898–2918). American Meteorological Society. https://doi.org/10.1175/2007jcli1999.1

Moerman, J. W., Cobb, K. M., Adkins, J. F., Sodemann, H., Clark, B., & Tuen, A. A. (2013). Diurnal to interannual rainfall δ18O variations in northern Borneo driven by regional hydrology. *Earth and Planetary Science Letters*, *369–370*, 108–119. https://doi.org/10.1016/j.epsl.2013.03.014

Nicholson, S. E. (2009). A revised picture of the structure of the "monsoon" and land ITCZ over West Africa. *Climate Dynamics*, *32*(7), 1155–1171. https://doi.org/10.1007/s00382-008-0514-3

Noone, D., Galewsky, J., Sharp, Z. D., Worden, J., Barnes, J., Baer, D., Bailey, A., Brown, D. P., Christensen, L., Crosson, E., Dong, F., Hurley, J. V., Johnson, L. R., Strong, M., Toohey, D., Van Pelt, A., & Wright, J. S. (2011). Properties of air mass mixing and humidity in the subtropics from measurements of the D/H isotope ratio of water vapor at the Mauna Loa Observatory. *Journal of Geophysical Research: Atmospheres*, *116*(D22). https://doi.org/10.1029/2011JD015773

Nusbaumer, J., Wong, T. E., Bardeen, C., & Noone, D. (n.d.). Evaluating hydrological processes in the Community Atmosphere Model Version 5 (CAM5) using stable isotope ratios of water. *Journal of Advances in Modeling Earth Systems*, *9*(2), 949–977. https://doi.org/10.1002/2016MS000839

Otto-Bleisner, B. L., Braconnot, P., Harrison, S. P., Lunt, D. J., Abe-Ouchi, A., Albani, S., Bartlein, P. J., Capron, E., Carlson, A. E., Dutton, A., Fischer, H., Goelzer, H., Govin, A., Haywood, A., Joos, F., Legrande, A. N., Lipscomb, W. H., Lohmann, G., Mahowald, N., … Renssen, H. (2016). The PMIP4 contribution to CMIP6 – Part 2: Two interglacials, scientific objective and experimental design for Holocene and last interglacial simulations. *Geoscientific Model Development Discussions*, *10.5194/gmd-2016–279*. http://centaur.reading.ac.uk/68688/

PAGES2k Consortium, Emile-Geay, J., McKay, N. P., Kaufman, D. S., Gunten, L. von, Wang, J., Anchukaitis, K. J., Abram, N. J., Addison, J. A., Curran, M. A. J., Evans, M. N., Henley, B. J., Hao, Z., Martrat, B., McGregor, H. V., Neukom, R., Pederson, G. T., Stenni, B., Thirumalai, K., … Zinke, J. (2017). A global multiproxy database for temperature reconstructions of the Common Era. *Scientific Data*, *4*, 170088. https://doi.org/10.1038/sdata.2017.88

Partin, J. W., Cobb, K. M., Adkins, J. F., Clark, B., & Fernandez, D. P. (2007). Millennial-scale trends in west Pacific warm pool hydrology since the Last Glacial Maximum. *Nature*, *449*(7161), 452–455. https://doi.org/10.1038/nature06164

Pausata, F. S. R., Gaetani, M., Messori, G., Berg, A., Maia de Souza, D., Sage, R. F., & deMenocal, P. B. (2020). The Greening of the Sahara: Past Changes and Future Implications. *One Earth*, *2*(3), 235–250. https://doi.org/10.1016/j.oneear.2020.03.002

Rayner, N. A., Parker, D. E., Horton, E. B., Folland, C. K., Alexander, L. V., Rowell, D. P., Kent, E. C., & Kaplan, A. (2003). Global analyses of sea surface temperature, sea ice, and night marine air temperature since the late nineteenth century. *Journal of Geophysical Research: Atmospheres*, *108*(D14). https://doi.org/10.1029/2002JD002670

Rhawn F. Denniston, Karl-Heinz Wyrwoll, Victor J. Polyak, Josephine R. Brown, Yemane Asmerom, Alan D. Wanamaker, Zachary LaPointe, Rebecca Ellerbroek, Michael Barthelmes, Daniel Cleary, John Cugley, David Woods, William F. Humphreys**.** A Stalagmite record of Holocene Indonesian–Australian summer monsoon variability from the Australian tropics, Quaternary Science Reviews, Volume 78, 2013, Pages 155-168, ISSN 0277-3791, https://doi.org/10.1016/j.quascirev.2013.08.004.

Risi, C., Bony, S., & Vimeux, F. (2008). Influence of convective processes on the isotopic composition (δ18O and δD) of precipitation and water vapor in the tropics: 2. Physical interpretation of the amount effect. *Journal of Geophysical Research: Atmospheres*, *113*(D19). https://doi.org/10.1029/2008JD009943

Rozanski, K. (2005). Isotopes in Atmospheric Moisture. In P. K. Aggarwal, J. R. Gat, & K. F. O. Froehlich (Eds.), *Isotopes in the Water Cycle* (pp. 291–302). Springer-Verlag. https://doi.org/10.1007/1-4020-3023-1_18

Sachs, J. P., Blois, J. L., McGee, T., Wolhowe, M., Haberle, S., Clark, G., & Atahan, P. (2018). Southward Shift of the Pacific ITCZ During the Holocene. *Paleoceanography and Paleoclimatology*, *33*(12), 1383–1395. https://doi.org/10.1029/2018PA003469

Saravana Kumar, U., Kumar, B., Rai, S. P., & Sharma, S. (2010). Stable isotope ratios in precipitation and their relationship with meteorological conditions in the Kumaon Himalayas, India. *Journal of Hydrology*, *391*(1), 1–8. https://doi.org/10.1016/j.jhydrol.2010.06.019

Sha, L., Ait Brahim, Y., Wassenburg, J. A., Yin, J., Peros, M., Cruz, F. W., Cai, Y., Li, H., Du, W., Zhang, H., Edwards, R. L., & Cheng, H. (2019). How Far North Did the African Monsoon Fringe Expand During the African Humid Period? Insights From Southwest Moroccan Speleothems. *Geophysical Research Letters*, *46*(23), 14093–14102. https://doi.org/10.1029/2019GL084879

Steig, E. J. (1999). Mid-Holocene Climate Change. *Science*, *286*(5444), 1485–1487. https://doi.org/10.1126/science.286.5444.1485

Tabor, C., Otto-Bliesner, B., & Liu, Z. (2020). Speleothems of South American and Asian Monsoons Influenced by a Green Sahara. *Geophysical Research Letters*, *47*(22), e2020GL089695. https://doi.org/10.1029/2020GL089695

Tian, Z., Li, T., & Jiang, D. (2018). Strengthening and Westward Shift of the Tropical Pacific Walker Circulation during the Mid-Holocene: PMIP Simulation Results. *Journal of Climate*, *31*(6), 2283–2298. https://doi.org/10.1175/JCLI-D-16-0744.1

Wang, Y., Cheng, H., Edwards, R. L., He, Y., Kong, X., An, Z., Wu, J., Kelly, M. J., Dykoski, C. A., & Li, X. (2005). The Holocene Asian Monsoon: Links to Solar Changes and North Atlantic Climate. *Science*, *308*(5723), 854–857. https://doi.org/10.1126/science.1106296

Wanner, H., Beer, J., Bütikofer, J., Crowley, T. J., Cubasch, U., Flückiger, J., Goosse, H., Grosjean, M., Joos, F., Kaplan, J. O., Küttel, M., Müller, S. A., Prentice, I. C., Solomina, O., Stocker, T. F., Tarasov, P., Wagner, M., & Widmann, M. (2008). Mid- to Late Holocene climate change: An overview. *Quaternary Science Reviews*, *27*(19), 1791–1828. https://doi.org/10.1016/j.quascirev.2008.06.013

Wei, Z., Lee, X., Liu, Z., Seeboonruang, U., Koike, M., & Yoshimura, K. (2018). Influences of large-scale convection and moisture source on monthly precipitation isotope ratios observed in Thailand, Southeast Asia. *Earth and Planetary Science Letters*, *488*, 181–192. https://doi.org/10.1016/j.epsl.2018.02.015

Wong, C. I., & Breecker, D. O. (2015). Advancements in the use of speleothems as climate archives. *Quaternary Science Reviews*, *127*, 1–18. https://doi.org/10.1016/j.quascirev.2015.07.019

Wong, T. E., Nusbaumer, J., & Noone, D. C. (n.d.). Evaluation of modeled land-atmosphere exchanges with a comprehensive water isotope fractionation scheme in version 4 of the Community Land Model. *Journal of Advances in Modeling Earth Systems*, *9*(2), 978–1001. https://doi.org/10.1002/2016MS000842

Yang, X., Yang, H., Wang, B., Huang, L.-J., Shen, C.-C., Edwards, R. L., & Cheng, H. (2019). Early-Holocene monsoon instability and climatic optimum recorded by Chinese stalagmites. *The Holocene*, *29*(6), 1059–1067. https://doi.org/10.1177/0959683619831433

Yao, T., Masson-Delmotte, V., Gao, J., Yu, W., Yang, X., Risi, C., Sturm, C., Werner, M., Zhao, H., He, Y., Ren, W., Tian, L., Shi, C., & Hou, S. (2013). A review of climatic controls on δ18O in precipitation over the Tibetan Plateau: Observations and simulations. *Reviews of Geophysics*, *51*(4), 525–548. https://doi.org/10.1002/rog.20023

Zheng, W., Wu, B., He, J., & Yu, Y. (2013). The East Asian Summer Monsoon at mid-Holocene: Results from PMIP3 simulations. *Clim. Past*, *9*(1), 453–466. https://doi.org/10.5194/cp-9-453-2013

Figures & Tables

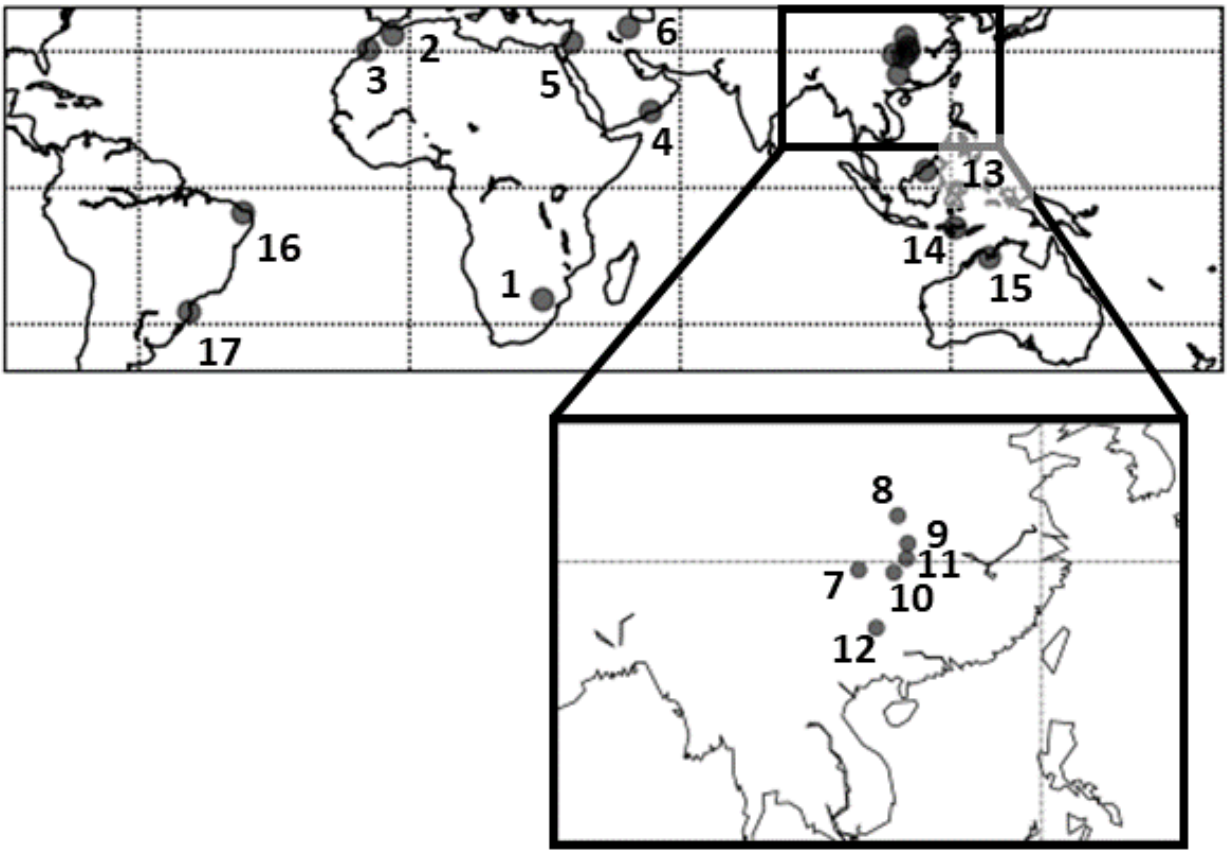

Figure 1.1 Proxy speleothem locations. Metadata in Table 1.1

Africa				
Name	**Location**	**Lat (°)**	**Lon (°)**	**$\Delta\delta^{18}O$**
Makapansgat Valley[1]	S. Africa	-24.1	29.11	0.244
Chaara[2]	N. Morocco	33.85	-4.246	-0.41
Wintimdouine[3]	Morocco	30.77	-9.49	-1.51
Middle East				
Name	**Location**	**Lat**	**Lon**	**$\Delta\delta^{18}O$**
Qunf[4]	Oman	17.17	54.3	-1.726
Jerusalem West[5]	Jerusalem	32.47	35.9	-0.395
Katalekhor[6]	Iran	35.83	48.16	-1.235
China				
Name	**Location**	**Lat**	**Lon**	**$\Delta\delta^{18}O$**
Chongqing[7]	China	29.5	106.8	-0.413
Jiuxian[8]	China	33.34	109.6	-0.959
Sanbao[9]	China	31.4	110.26	-1.395
Lianhua[10]	China	29.29	109.32	-1.61
Heshang[11]	China	30.27	110.25	-0.83
Dongge[12]	China	25.28	108.08	-0.946
SE Asia, Warm Pool, and Pacific				
Name	**Location**	**Lat**	**Lon**	**$\Delta\delta^{18}O$**
Gunung Buda[13]	N. Borneo	4.03	114.8	-0.314
Liang Luar[14]	Indonesia	-8.533	120.43	-0.183
KNI-51[15]	W. Australia	-15.18	128.37	0.085
Americas				
Name	**Location**	**Lat**	**Lon**	**$\Delta\delta^{18}O$**
Rio Grande Norte[16]	Brazil	-5.36	-37.44	-3.5
Botuvera[17]	Brazil	-27.22	-49.15	-0.23

Table 1-1 Speleothem metadata. All data accessed through NCEI paleoclimate data archives (https://www.ncdc.noaa.gov/data-access/paleoclimatology-data/datasets/speleothem). Citations: [1]Holmgren et al., 2003; [2]Ait Brahim et al., 2019; [3]Sha et al., 2019; [4]Fleitmann et al., 2003; [5]Frumkin et al., 1999; [6]Andrews et al., 2020; [7]Yang et al., 2019; [8]Cai et al., 2010; [9]Dong et al., 2010; [10]Cosford et al., 2008; [11]Hu et al., 2008; [12]Dykoski et al., 2005; Wang et al., 2005; [13]Partin et al., 2007; [14]Ayliffe et al., 2013; [15]Denniston et al., 2013; [16]Cruz et al., 2009 [17]Cruz et al., 2005

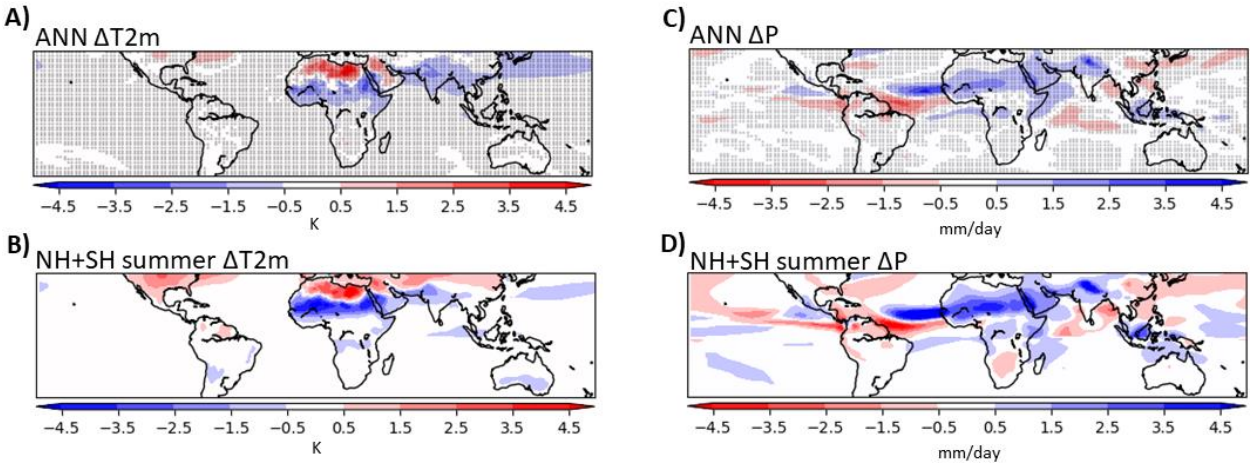

Figure 1.2 Annual and summertime change in 2-meter air temperature and precipitation rate for MH-PI. A) Annual mean change in 2m T; B) change in 2m T, with May through September mean (MJJAS) plotted in the NH and November through March mean (NDJFM) plotted in the SH; C) and D) as in A and B, but for change in total precipitation.

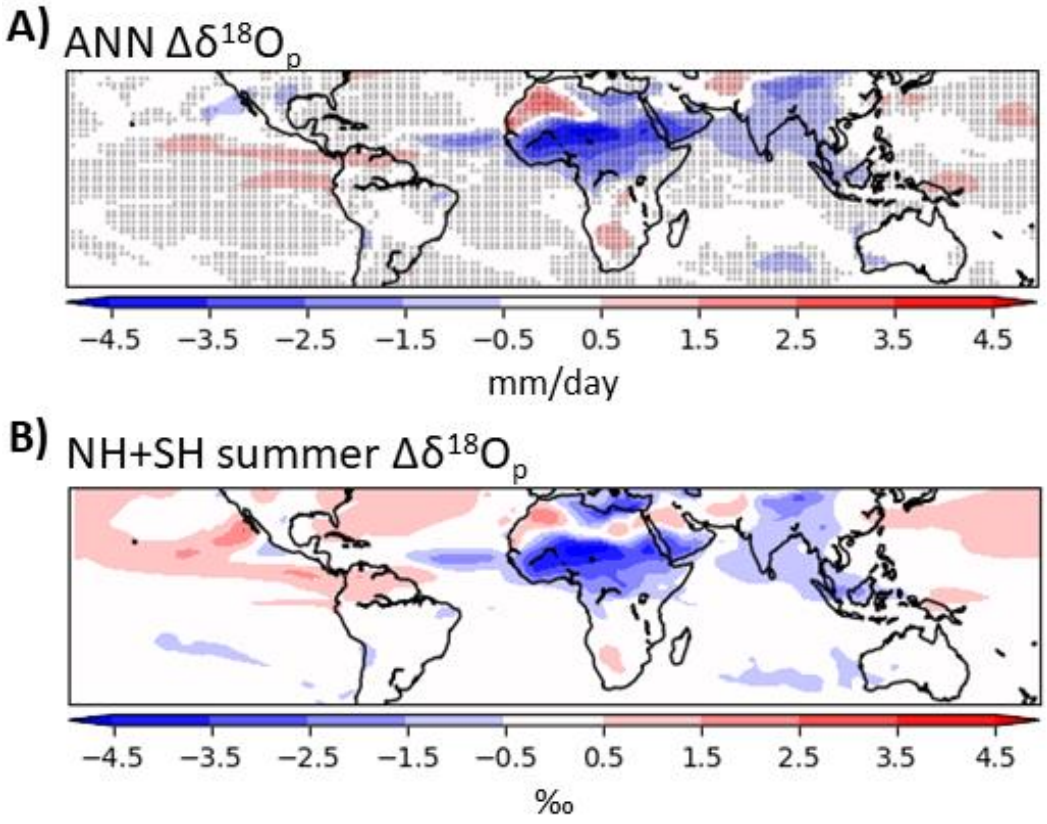

Figure 1.3 Change in simulated precipitation isotope ratio, $\Delta\delta^{18}O_p$. A) annual mean $\Delta\delta^{18}O_p$ (ANN); B) summertime $\Delta\delta^{18}O_p$, with summers defined as in Fig. 1.1

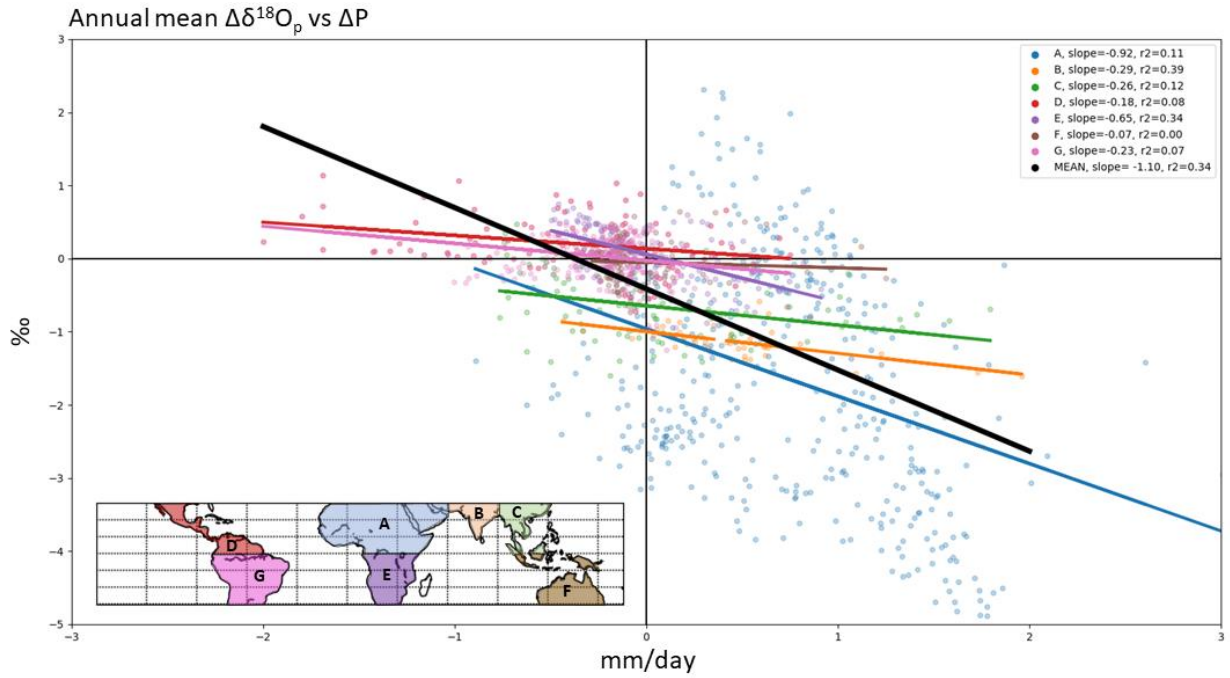

Figure 1.4 $\Delta\delta^{18}O_p$ vs ΔP for annual mean land-based precipitation between latitudes 30° S and 30° N. Dots are colored by shared location, generally assembled around monsoon regions, shown in the map inlay in the bottom left. Colored lines are the linear regressions of $\Delta\delta^{18}O_p$ on ΔP spanning the domain of the region. Black line represents the linear regression of all data.

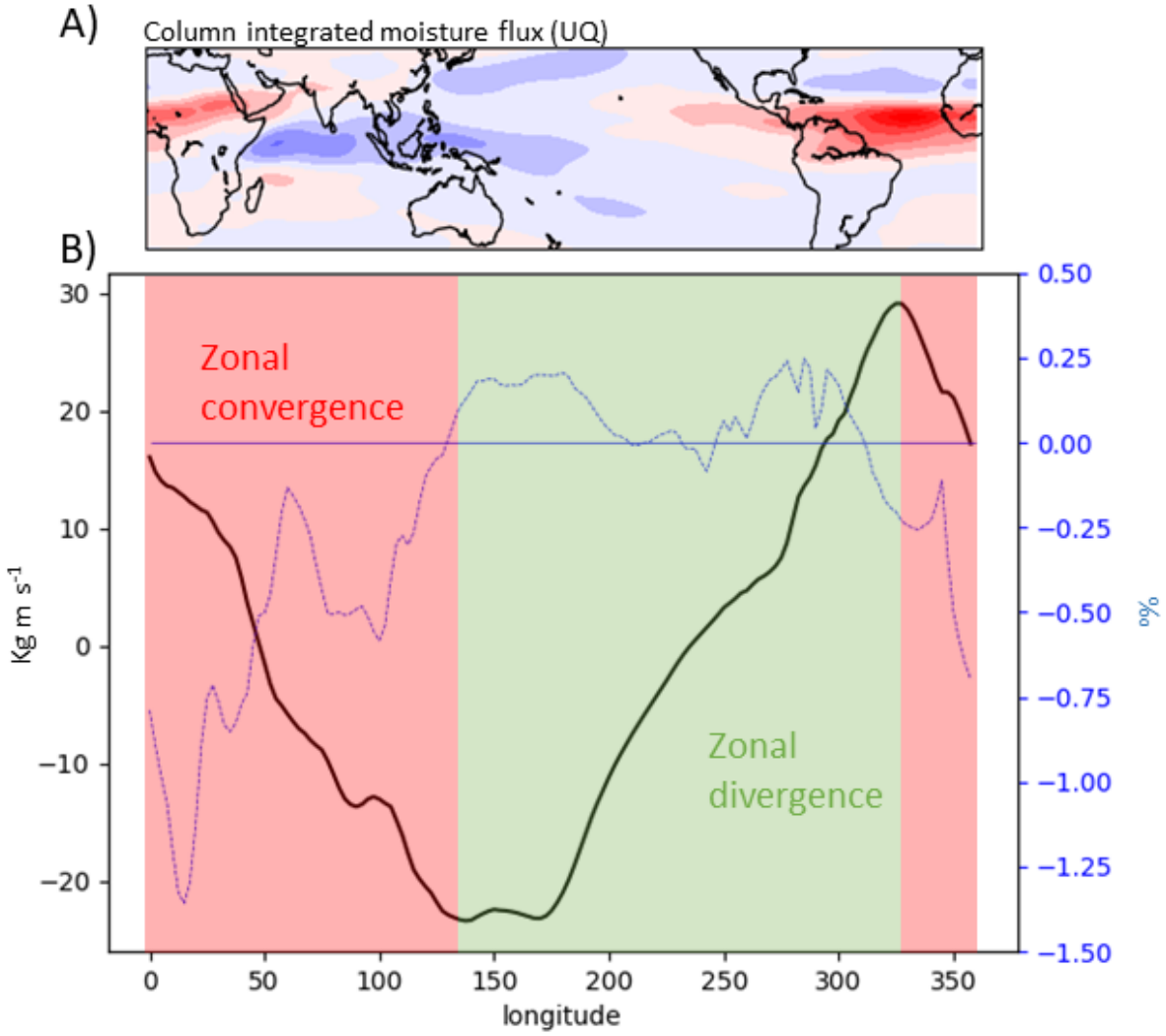

Figure 1.5 Zonal mean vapor transport and precipitation isotope ratio. A) MH-PI map of column integrated zonal moisture flux, UQ. B) MH –PI zonal mean, column integrated moisture flux, averaged over 30°S – 30°N (solid black line) and zonal mean isotope precipitation isotope ratio (blue dotted line). Background colors highlight regions of negative (red, convergence) and positive (green, divergence) slope.

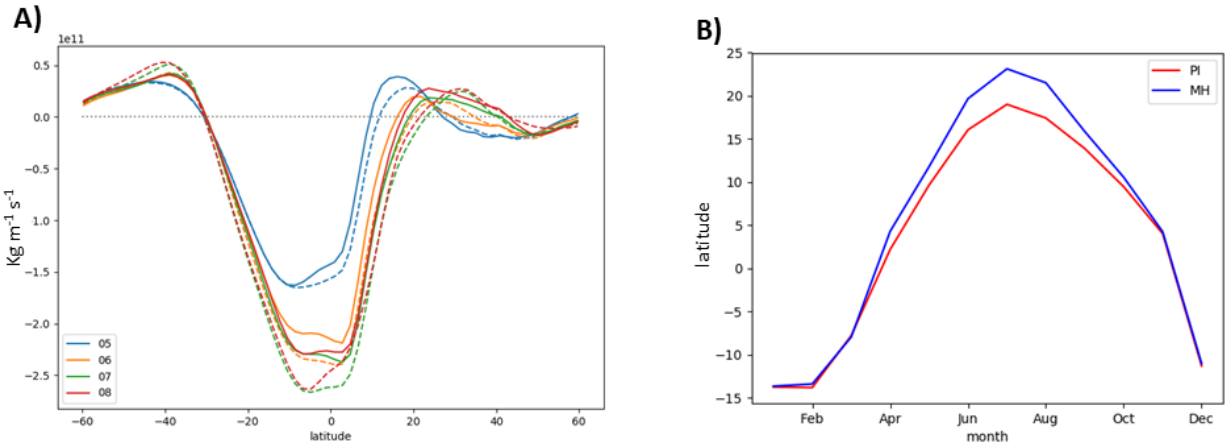

Figure 1.6 Estimations of changes to the Hadley Cell and ITCZ position during the MH. A) 500mb meridional mass stream function for months May-August, averaged across all longitudes. Solid lines are PI and dashed lines are MH stream functions. B) Seasonal cycles of the latitude of ITCZ center. ITCZ center latitude during NH summer is determined as the first zero-crossing in the NH of the 500mb isobar stream function.

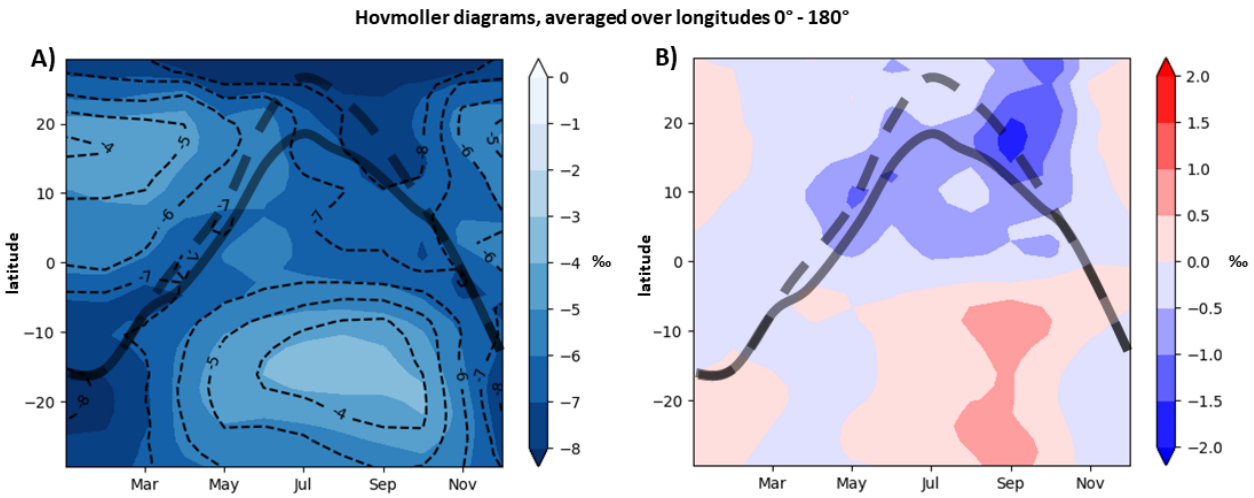

Figure 1.7 Hovmoller diagrams of $\delta^{18}O_p$ and $\Delta\delta^{18}O_p$ in latitude and month, averaged over longitudes 0° - 180°. A) Blue filled contours of PI $\delta^{18}O_p$ and black line contours of MH $\delta^{18}O_p$; B) $\Delta\delta^{18}O_p$. In both plots, the thick black line tracers the position of the center of the ITCZ in the PI (solid) and MH (dashed). ITCZ center location is calculated as in fig. 1.6.

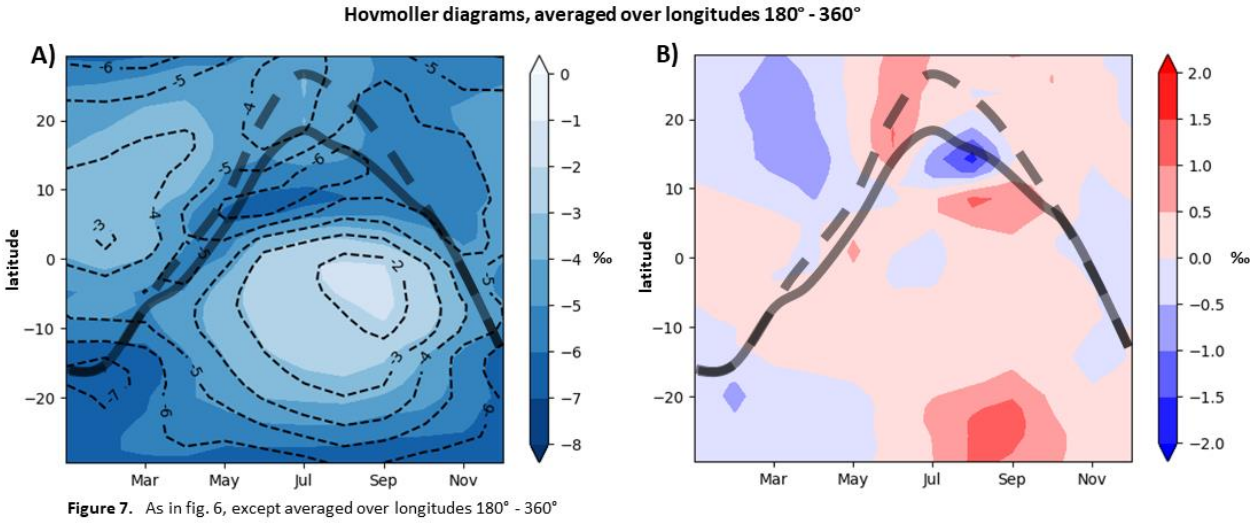

Figure 7. As in fig. 6, except averaged over longitudes 180° - 360°

Figure 1.8 As in Fig. 1.7, except averaged over longitudes 180° - 360°

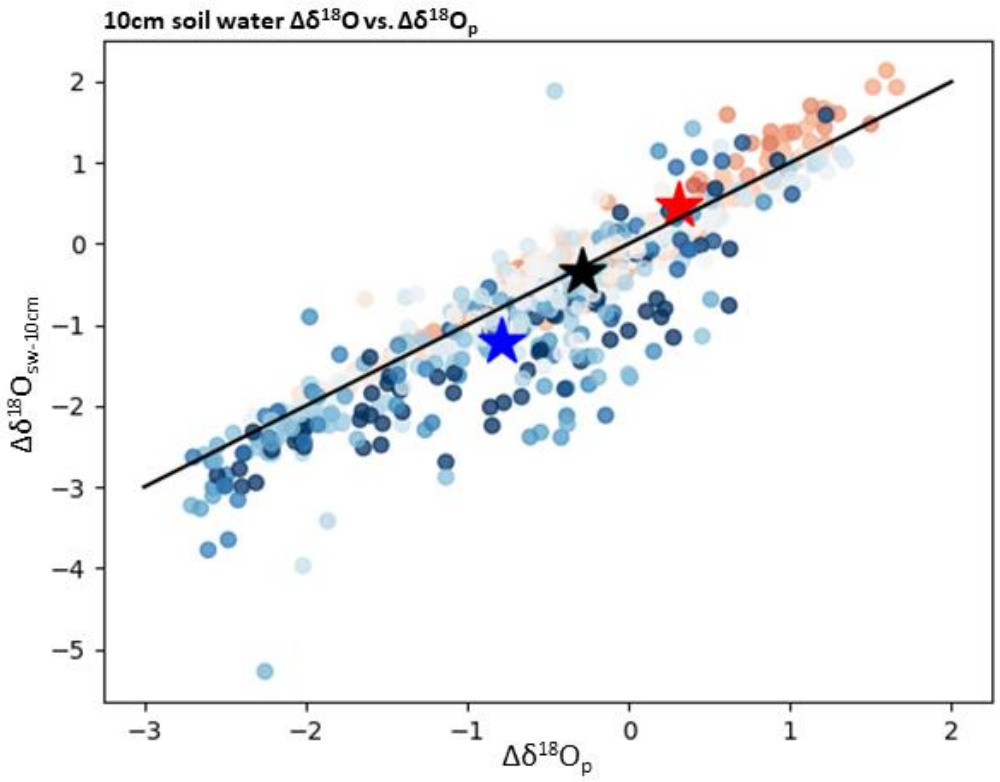

Figure 1.9 $\Delta\delta^{18}O$ of 10 cm soil water vs $\Delta\delta^{18}O_p$, colored by Δrelative humidity (RH) at 2m above surface (red < 0, blue > 0). The red, blue, and black stars are the means of ΔRH < -5% and ΔRH > 5%, and -5% < ΔRH < 5% composites, respectively. Black line is 1:1.

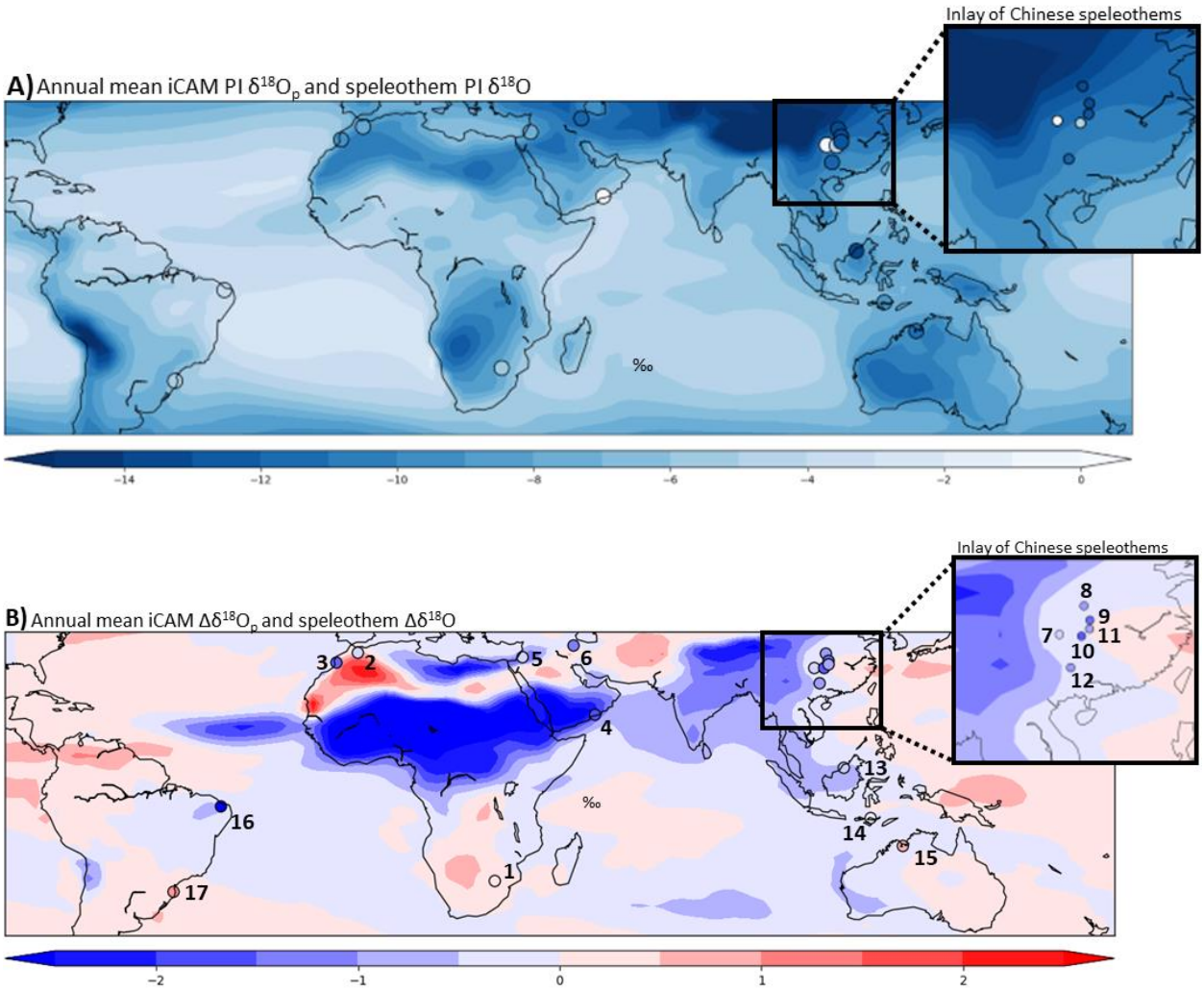

Figure 1.10 Model-proxy comparison of $\delta^{18}O$. A) Filled contours are iCAM simulated annual mean, amount-weighted PI $\delta^{18}O_p$, and dots are the 17 speleothem proxies presented in this study, filled in using the same coloring scale as the contours. Speleothem locations are numbered according to Table 1.1. B) Same as in A, but for the MH-PI difference.

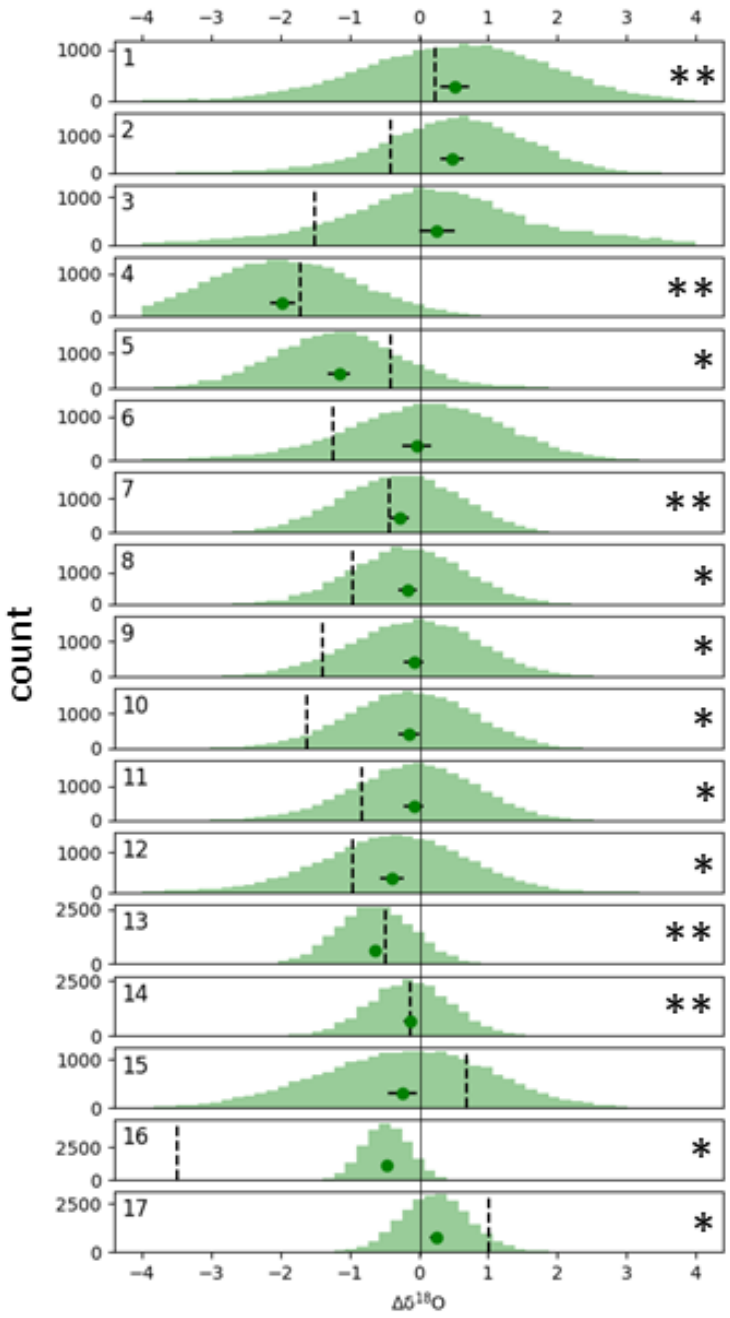

Figure 1.11 Histograms of simulated iCAM $\Delta\delta^{18}O_p$ linearly interpolated to speleothem locations. Histograms are calculated using every combination of MH-PI years (total of 150^2 differences). Green dots are the speleothem location iCAM annual and amount-weighted mean $\Delta\delta^{18}O_p$, shown with +- $2\sigma^2$ bars. Short vertical dashed lines are the proxy speleothem $\Delta\delta^{18}O$ value. The thin vertical dotted line marks the $\Delta\delta$=0 line for clarity. Stars denote proxy-model fit, where 1 star indicates the sign of $\Delta\delta$ is the same for model and proxy, and two stars indicating model-proxy differences are not significantly different than zero.

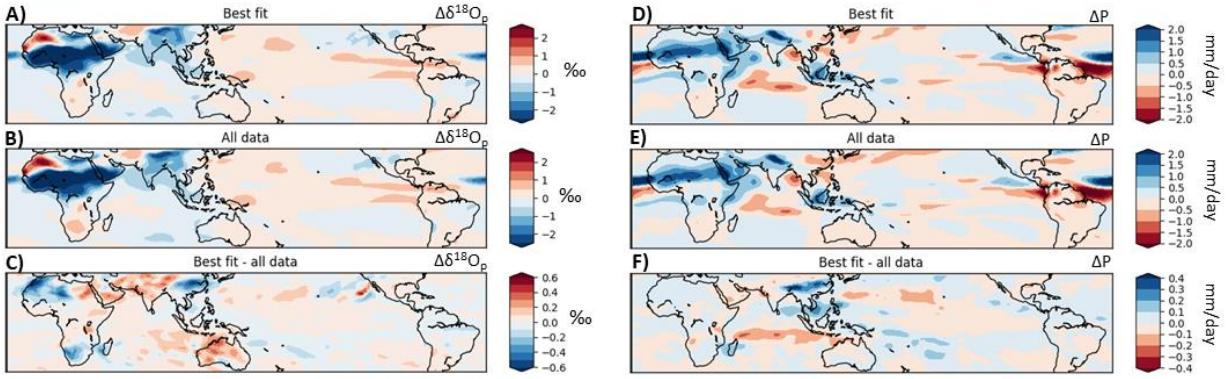

Figure 1.12 Best-fit composite results. A) Best-fit composite mean $\Delta\delta^{18}O_p$; B) All data mean $\Delta\delta^{18}O_p$; C) Best-fit composite – all data $\Delta\delta^{18}O_p$; D-F) As in A-C but for ΔP**.**

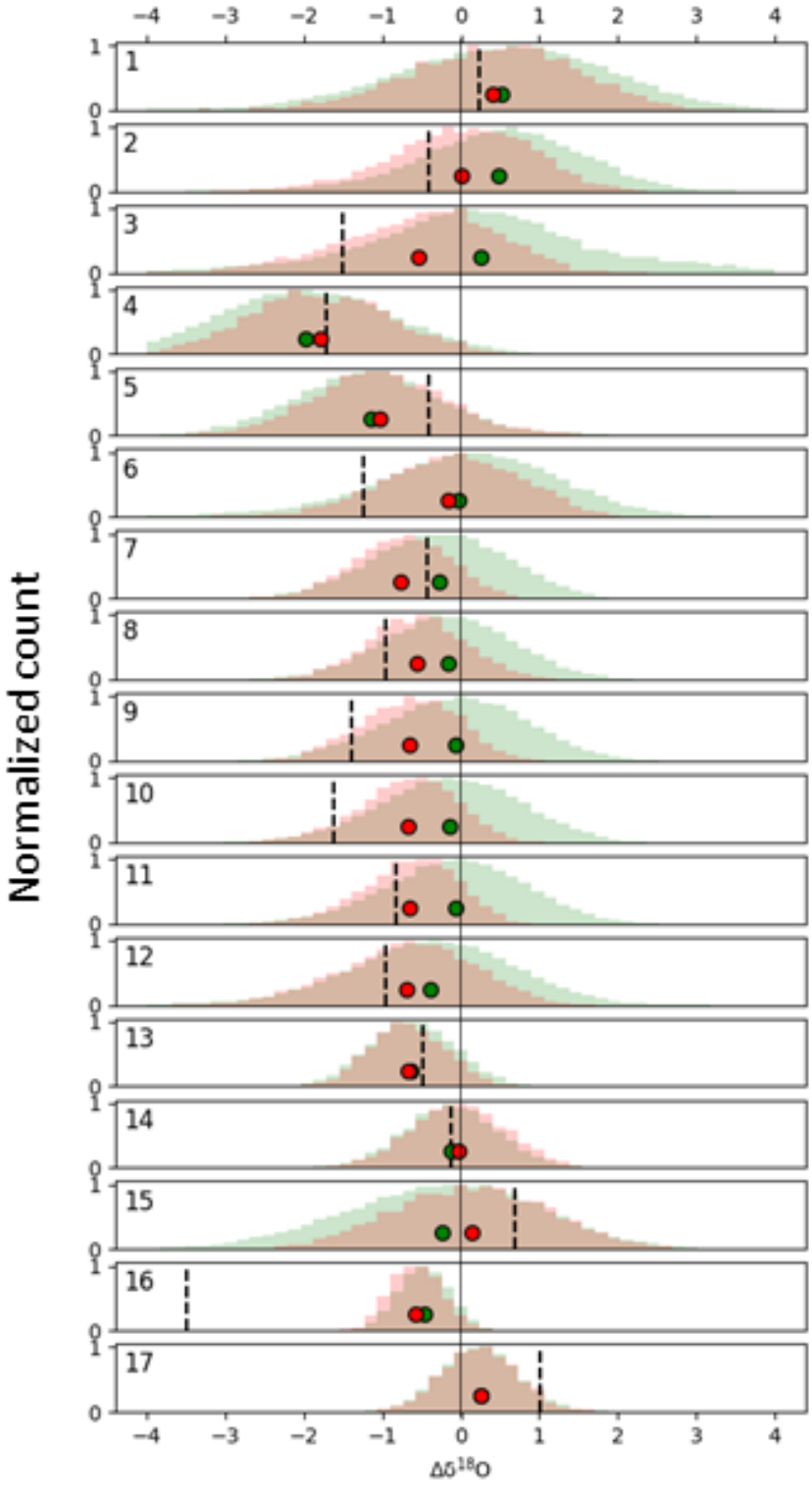

Figure 1.13 Proxy-model comparison using best-fit composite data. Red histograms represent the best-fit composite data, and red dots the best-fit composite mean. Green histograms and dots, short vertical dashed bars, and thin vertical dotted bar are all as in fig. 1.10

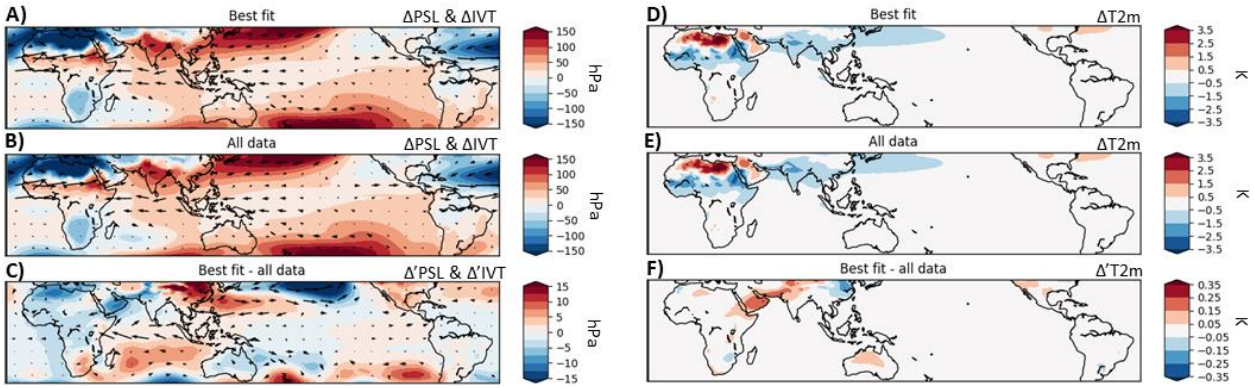

Figure 1.14 Best-fit composite results for PSL, IVT, and T, as in Fig. 1.11. A-C) change in pressure at sea level (ΔPSL) with column-integrated vapor transport vectors (ΔIVT); D-F) ΔT2m.

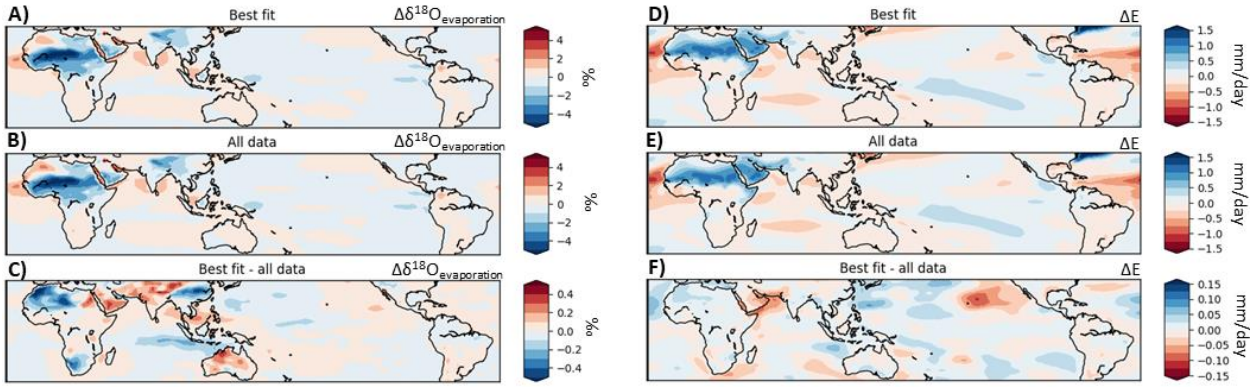

Figure 1.15 Best-fit composite results for $\delta^{18}O_E$ and E, as in Fig. 1.11. A-C) change in isotope ratio of evaporation ($\Delta\delta^{18}O_{evaporation}$); D-F) Δevaporation (ΔE).

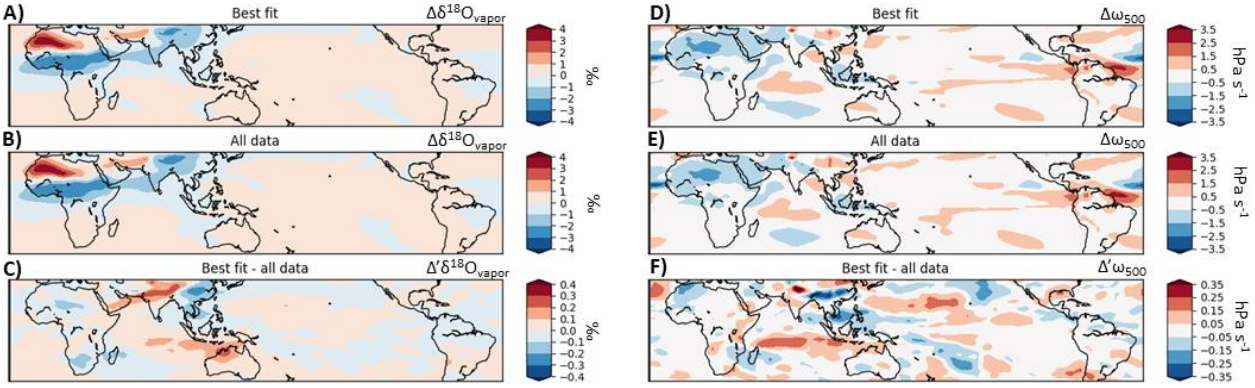

Figure 1.16 Best-fit composite results for $\delta^{18}O_V$ and ω_{500}, as in Fig. 1.11. A-C) change in isotope ratio of column-integrated vapor ($\Delta\delta^{18}O_{vapor}$); D-F) change in vertical velocity at 500 hPa ($\Delta\omega_{500}$).

Chapter 2: Targeted tagging experiments reveal a Pacific Ocean influence on East Asian Summer Monsoon $\delta^{18}O_p$ in green-Sahara simulations.

Kyle Niezgoda*
Clay Tabor
Rich Fiorella
David Noone

Abstract

The Sahara, currently the largest desert in the world, was covered in woody shrubs and grasses during the mid-Holocene (MH, 6 kya), a climate phenomenon sometimes referred to as the "green Sahara". Climate model simulations forced with the orbital characteristics of the MH often fail to recreate the hydrology response necessary to support the vegetation, lake level, and human societies that existed during this time, but this model-proxy mismatch is improved when proxy-appropriate vegetation in northern Africa is included in the MH simulation. Further studies have demonstrated that MH vegetation simulations improve model-proxy agreement in distant tropical areas, such as in the East Asian Summer Monsoon (EASM). In this paper, the relationships between vegetation in northern Africa and the isotope ratio of rainfall, δ_p, of the EASM are explained using simulations from the isotope-enabled Community Atmosphere Model (iCAM). Water tracers, or tags, are added to iCAM to enable a full detailing of shifts in moisture source that occur during high vegetation MH simulations. This is achieved with a tag-based decomposition of EASM rainfall. The decomposition quantifies the contribution of two distinct factors to vegetation-related changes in EASM δ_p (or $\Delta\delta_p$): 1) changes in moisture source contribution to total EASM rainfall, and 2) changes to the isotope ratio of EASM moisture originating from different sources. The results reveal that shifts in moisture sourcing have a much larger contribution to $\Delta\delta_p$ than changes in the isotope ratio of moisture sources. It is shown that intra-tag differences in isotope ratio (i.e. the spatial distribution of isotopes) are more important than inter-tag difference (i.e. the vegetated minus non-vegetated difference in isotope ratio) for determining EASM $\Delta\delta_p$. In the vegetated Sahara simulation, moisture of Pacific origin makes up a larger fraction of total EASM rainfall than in the non-vegetated simulation, resulting in negative EASM $\Delta\delta_p$ because Pacific vapor that reaches the EASM has a

relatively low value of δ_p compared to other vapor sources. The Pacific contribution to EASM rainfall increases in the vegetated climate because there is increased concentration of transport pathways between the Pacific and EASM. The implication of these results is twofold. First, moisture sources that contribute a relatively small fraction of total EASM rainfall (e.g. < 5% of total rainfall) are shown to have meaningful impacts on EASM $\Delta\delta_p$, suggesting that canonically defined EASM moisture sources (e.g. the Bay of Bengal and the South China Sea) are not including important isotopic contributions from regions with low total moisture contributions. Second, when intra-tag differences in the isotope ratio of EASM rainfall are large, changes in the spatial pattern of moisture sourcing will outweigh changes to the isotope ratio of the sources. This is likely to be true for rainfall that is composed of vapor from many isotopically distinct sources, such as the Pacific Ocean, the Indian Ocean, and continental evapotranspiration.

Introduction

The mid-Holocene (MH, 6 *kya*) is marked by many significant climate differences from the modern day (Wanner et al. 2009; Wang et al. 2013). One such climate anomaly is the Holocene African Humid period, sometimes known as the green Sahara (GS), which occurred between 15-5 *kya*, peaking around the MH (Klees & Kuper 1992; Pachur & Hoelzmann, 2000; Gasse, 2000; Kuper & Kröpelin, 2006; Pausata et al., 2020). During this time, it is thought that northern hemisphere ecosystems of Africa migrated north, resulting in warm grasses and woody shrubs in the region of the modern-day Sahara, and species of tropical or near-tropical origin in the modern-day Sahel (Watrin et al. 2009). Human societies repopulated the newly vegetated Sahara, and the subsequent desertification during the late Holocene influenced human migration patterns out of Africa (Larrasoaña et al. 2013). The presence of a vegetated Sahara during the MH is supported by an abundance of proxy evidence in a variety of geologic forms (deMenocal and Tierney 2012). Examples include: paleo lake level reconstructions (Ritchie et al. 1985; Damnati 2000), fossilized pollen samples in lakebed sediments (Amaral, et al. 2013), leaf-wax isotope ratios (Tierney et al., 2017), terrigenous sediment concentration in near-shore ocean cores (Adkins et al. 2006), archaeological evidence of human societies in modern inhospitable areas (Hoelzmann et al. 2001; Stojanowski and Knudson 2014), and a

plethora of general circulation model (GCM) simulations of the MH, the latter of which is the focus of this paper.

GCM simulations of the MH have become a paleoclimate modeling benchmark due, in large part, to continued efforts of the Paleoclimate Model Intercomparison Project (PMIP). Per PMIP specification, the default model setup for the MH experiment does not require a dynamically evolving vegetation model or a prescribed vegetation field that is different from the pre-Industrial control (PI, 1850 CE) experiment (Otto-Bliesner et al. 2016). However, MH simulations forced with the same vegetation as the PI fail to simulate a precipitation response capable of sustaining the proxy-suggested vegetation and surface waters of the GS by at least an order of magnitude, and often fail to reproduce the northward advancement of West-African Monsoon rainfall (Joussaume et al., 1999; Doherty et al., 2000; Boos & Korty, 2016). The presence of a dynamic vegetation model sometimes improves model-proxy agreement (e.g. Claussen and Gayler 1997; Hu et al., 2018), but not always (e.g. Tierney et al 2017) because the high albedo and negligible soil moisture of the modern Sahara presents a barrier to new vegetation formation even in the presence of supporting rainfall (Knorr and Schnitzler, 2006).

Despite these shortcomings, advances have been made in improving the simulated reconstructions of the GS. Several studies have identified model-proxy precipitation improvements by simulating the MH with prescribed north African vegetation reconstructions derived from evidence from the MH proxy evidence (Brovkin et al., 1998; Levis et al., 2004; Patricola & Cook, 2007; Braconnot et al. 2012; Skinner & Poulsen, 2016; see Claussen et al., 2017 for a general overview) and prescribed dust reductions thought to co-occur with increased vegetation and soil moisture of the MH Sahara (Pausata et al., 2017; Thompson et al. 2019). More recently, other experiments have further identified model-proxy improvements in non-Saharan regions under GS conditions, driven by tropical teleconnections forced by the introduction of vegetation in north Africa. For example, GS simulations have shown increased accuracy in northern hemisphere monsoon precipitation (Sun et al. 2019), improved suppression of ENSO variability thought to occur during the MH (Pausata et al., 2017), reproduced droughts in SE Asia (Griffiths et al., 2020), and improved Asian Monsoon precipitation isotope ratios (Tabor et al., 2020).

Physical links between different monsoon systems are firmly established (Rodwell and Hoskins, 1996). Monsoon onset causes local anomalous atmospheric heating, which increases vertical velocity and reduces surface pressure. These signals are propagated horizontally via Rossby waves and can interact with other regions of the Tropical Rain Belt. In the case of the GS, anomalous heating is the result of increases in local evapotranspiration as well as increases in the convergence of Atlantic vapor onto the continent, both of which increases the amount of precipitable vapor over Africa, resulting in more precipitation, and therefore more latent heating of the atmosphere. With these additional sources of heat, the GS atmosphere expands and propagates a Rossby wave.

Asian Monsoon response to the green Sahara

Several recent studies have identified a link between GS forcings and rainfall in tropical or tropically-influenced eastern Asia. Using a green Sahara plus reduced dust simulation of the MH, Pausata et al. (2017) showed how the GS can induce a suppression of ENSO variability via intensification of West African Monsoon (WAM) rainfall. In short, enhanced zonal convergence from the tropical Atlantic onto north Africa (westerly flow) forced a weakening of the trade winds (easterly flow) in the Eastern Pacific. This reduced upwelling on the west coast of South America and weakened the ocean-atmosphere feedbacks required for large ENSO variability. Consequently, trade winds in the west Pacific were strengthened, and the Walker circulation shifted westward (see fig. 8 from Pausata et al., 2017). This established a physical basis for a connection between GS-induced forcing and the hydroclimate of tropical Asia via shifts in the Walker cell. Expanding on this GS-Walker relationship, Griffiths et al. 2020 showed that the collapse of the GS coincided with mega droughts in Southeast Asia (Griffiths et al., 2020). Using a conceptual framework similar to Pausata 2017, Griffiths 2020 identified the teleconnection in reverse – that the *removal* of the GS shifted the Walker circulation *east*, which forced a more "niño-like" mean state in the tropical Pacific, reduced surface convergence and convective activity in the Indo-Pacific Warm Pool, and eventually lead to megadroughts in SE Asia. The precipitation response in SE Asia from the collapse of the GS closely resembles the precipitation anomalies associated with strong El Niño events (see figure 1 in Griffiths et al., 2020).

Tabor et al., 2020 (T20) showed that model-proxy agreement was improved for the precipitation isotope ratios ($\delta^{18}O_p$) of several speleothem proxies in the East Asian Summer Monsoon (EASM) when GS vegetation was included in northern Africa. Because many proxies of tropical hydroclimates are based on $\delta^{18}O_p$, this provides a direct model-proxy comparison for evaluating the impacts of the GS. T20 found that Green Sahara – dry Sahara $\delta^{18}O_p$ averaged over the EASM was -0.67‰, which improved the agreement between the speleothem isotope data and the modelled isotope fields. This isotopic depletion occurs despite near zero change in precipitation amount in the same region, seemingly in contrast to the often-induced "amount-effect" anticorrelation, which would predict that decreases in $\delta^{18}O_p$ coincide with increases in seasonal mean precipitation totals. Simulated near zero changes in precipitation in the MH EASM is not a novel finding - simulations of the MH often predict an EASM that is drier than the proxies suggest, regardless of the type of vegetation used in northern Africa (Zhao & Harrison, 2012; Braconnot et al., 2012). T20 offer an explanation for the isotopic depletion that is based on moisture source dynamics: the newly vegetated Sahara introduces a large amount of highly depleted water vapor during the northern hemisphere summer monsoon season; concurrently, the North Pacific subtropical high is enhanced and shifted south, increasing the vapor contribution from the south and west of the Asian monsoon; the combination results in depleted $\delta^{18}O$ of water vapor (and thus precipitation) in the EASM. While this narrative is plausible, it was not quantitatively shown to drive changes in EASM monsoon $\delta^{18}O_p$.

Although recent advances in the realm of GS-EASM teleconnections have been achieved, key physical mechanisms remain understudied. T20 showed that GS-induced shifts in EASM $\delta^{18}O_p$ occur without a complementary shift in precipitation, which begs the question: what, if not ΔP, causes the simulated $\Delta\delta^{18}O_p$? The GS almost certainly increases the amount of available vapor from north Africa, India, and generally western sources to the EASM, but the extent to which these distant sources contribute to ΔP and $\Delta\delta^{18}O_p$ in the EASM is unknown. Results from Pausata and Griffiths indirectly imply a Pacific influence on the EASM via GS-induced shifts in the Walker Cell, suggesting that shifts in the convergence of Pacific vapor could occur and could result in changes to EASM hydrology, but the extent to which this occurs

has also not been quantified. Addressing these unknowns is a fundamental step towards a complete, accurate, and useful interpretations of isotope proxies from the EASM.

Objectives

This paper expands on GS-EASM teleconnections identified previously by exploring the links between vapor sourcing and isotope ratio changes for EASM rainfall under GS forcing. Specifically, the isotope-focused approach of T20 is utilized, because the unique utility of simulated isotopes allows for direct model-proxy comparison. Using results from an isotope-enabled climate model simulation of the MH forced with a Green Sahara, two questions are addressed: first, does the relative contribution of vapor sources to EASM rainfall change, and do the isotope ratios of the contributing sources change? Second, what dynamical changes are established by the GS that force these shifts in moisture sourcing and/or isotope ratio? These questions are answered by adding water tracers to a climate model setup closely resembling that used by T20, to directly calculate the change in vapor contribution for various moisture source regions, as well as the change in isotope ratio of those sources. The green Sahara – dry Sahara (referred to as gs-dry) EASM precipitation isotope ratio change, $\Delta\delta^{18}O_{ASM}$, is deconstructed into a component driven by changes in the relative contribution of vapor sources to the total EASM rainfall, and a component driven by changes in the isotope ratio of the vapor sources. Finally, these results are explained as a function of dynamical changes in the climate that occur because of the GS, using a vapor budget.

Methods and materials

Isotope-enabled, tracer-enabled CAM

As in T20, the GCM used in this study is an atmosphere-only setup of the Community Earth System Model v 1.2 (CESM 1.2, Hurrell et al. 2013) with isotope-enabled Community Atmosphere Model (iCAM 5, Nusbaumer et al. 2017) and Community Land Model (iCLM 4.5, Lawrence et al. 2011; Wong et al. 2017) active. 200 years are simulated, with the first 50 removed to allow ample model spin-up of deep soil water, and the last 150 years are averaged to calculate equilibrium climate states. Two mid-Holocene simulations are performed, in which all boundary conditions are held constant except for the vegetation coverage over northern

Africa and the Arabian peninsula. In the control run (MHdry), the MH in simulated using pre-Industrial vegetation. In the green Sahara experiment (MHgs), the MH is simulated using a reasonable approximation of proxy-suggested vegetation for northern African and the Arabian Peninsula. Vegetation fields for the MHgs experiment are from T20; briefly, average PI vegetation conditions from 11°N were extended northward through the Sahara and Arabian peninsula, except where vegetation coverage already exceeded 10%. Orbital parameters and greenhouse gas concentrations follow the PMIP4 guidelines for both MH experiments (Otto-Bliesner et al. 2016). Both simulations use mean monthly, post-spin-up SSTs from the fully-coupled Community Climate System Model v4 (CCSM4) MH experiment contribution to the PMIP3/CMIP5 database, which are the most recent publicly available MH SSTs from CCSM4, the predecessor to CESM 1.2. In both MH experiments, dynamic vegetation is turned off to prevent the growth or death of new plant species. In addition to the MH simulations, a pre-Industrial (PI) control run is also carried out to characterize MH climate anomalies. The PI run is specified to the CMIP6 experimental design for the pre-Industrial control (Eyring et al. 2016) and uses mean Hadley Sea Surface Temperatures and Sea Ice extent (Deser et al., 2010; Rayner et al., 2003)

Tagging setup

In all simulations, iCESM is modified to include 18 location-based water tracers, or tags, shown in figure 1. Location-based tags utilize iCAM's existing hydrologic framework by assigning a new named "type" of water to the atmospheric vapor budget that results from surface evaporation within the tag region (referred to as "evaporation-based tracers" in Fiorella et al. 2021, see also Nusbaumer et al., 2017). These tags are preserved as vapor is moved horizontally and vertically along advection pathways, altered through phase changes, and condenses into precipitation, upon which point the tag is reset (Singh et al., 2016a, b). Tags are purely passive tracers – they do not interact with or alter the solutions to the physics and dynamics calculated by the model, but they do faithfully follow the hydrological cycle.

Each tag is defined by one or more rectangular boxes which are determined using a few criteria. Because of the high computational cost of adding tracers to the model, the tag layout

strikes a balance between relatively high-resolution near the area of interest (in this case, the East Asian Summer Monsoon, shown in figure 2) and lower resolution further away. Tag regions are assigned based on shared geographic and climatological features. Coordinates for large bodies of water (e.g. the Bay of Bengal, the South China Sea) and continents/land regions (e.g. India, South East Asia) are approximated to the nearest grid cell edge, defined by the model resolution. Tags correspond to either completely continental evapotranspiration or oceanic evaporation; the tagged evaporative flux into the model's atmosphere is masked by the relevant surface fraction to account for this. The tag layout shown in figure 1 accounts for 99.9% of rainfall at the EASM.

Tag decomposition of $\Delta\delta^{18}O_{total}$

To decompose the total Δδ18O signal of the EASM, an approach like Tabor et al., 2018, is utilized with some slight modifications. This study seeks to specifically identify independent changes in moisture source contribution and moisture source isotope ratio. Total EASM precipitation, P_{ASM}, is considered composed of a mixture of water originating from multiple vapor sources, P_{tag}. Each P_{tag} constitutes a fraction, f_{tag}, of the total rainfall, i.e. $f_{tag} = P_{tag} / P_{ASM}$. Further, this analysis defines the adjusted isotope ratio of each tag region, D_{tag}, in terms of the difference between the isotope ratio of precipitation water originating from that tag, $\delta^{18}O_{tag}$, and the $\delta^{18}O_{ASM}$ of the base MH experiment (MH_{dry}), i.e. for each tag, $D_{tag} = \delta^{18}O_{tag} - \delta^{18}O^{dry}_{EASM}$. Here the subscript "EASM" indicates the total, untagged rainfall that occurs at the EASM region used in this study. This provides the convenient numerical property that positive values of D_{tag} indicate that the tagged rainfall has a higher isotope ratio than the control isotope ratio, and negative values indicate the tag has a lower isotope ratio. Note that by using this definition of D_{tag}, the following is true:

$$D^{dry}_{EASM} = 0‰$$

and

$$D^{gs}_{EASM} = \delta^{18}O^{gs}_{EASM} - \delta^{18}O^{dry}_{EASM} = \Delta\delta^{18}O_{EASM}$$

Therefore,

$$\Delta D_{EASM} = D^{gs}_{EASM} - D^{dry}_{EASM} = \Delta\delta^{18}O_{EASM}$$

Because of numerical imprecision in the model transport scheme, a closure term is calculated as the "rest of the world" tag (ROW):

$$f_{ROW} = 1 - \sum_{i \in tags} f_i$$

By including the ROW tag, the combination of all tags is guaranteed to account for 100% of the rainfall occurring at any given location. In tropical locales, including the two shown in the results section, the ROW tag accounts for approximately .1% or less of total rainfall, indicating that the non-ROW tags used in this study accounts for ~99.9% of total rainfall.

Given f_{tag} and D_{tag} the adjusted isotope ratio of total rainfall, D_{total}, is:

$$D_{total} = \sum_{i \in tags} f_i * D_i$$

Here, D_{EASM} is the sum of the tagged isotope ratios weighted by their fractional contribution to total rainfall. The MHgs-MHdry difference is denoted by the letter Δ such that:

$$\Delta D_{total} = \sum_{i \in tags} (f_i^{gs} * D_i^{gs} - f_i^{dry} * D_i^{dry})$$

where superscripts gs and dry denote the MHgs and MHdry experiments respectively. Terms within the summation can be expanded and rearranged in terms of differences in the moisture fraction Δf and the isotopic delta values, ΔD, to reveal:

$$\Delta D_{total} = \sum_{i \in tags} [\Delta f_i * D_i^{dry}] + [\Delta D_i * f_i^{dry}] + [\Delta f_i * \Delta D_i]$$

This partitions the total isotope ratio change into three physically distinct terms: 1) gs-dry changes in f_{tag} with D_{tag} held constant at the control (dry) value; 2) gs-dry changes in D_{tag} with f_{tag} held constant at the control (dry) value; 3) gs-dry changes in D_{tag} and f_{tag} combined, which are referred to as 1) the f-effect, 2) the D-effect, and 3) the covariance.

The decomposition is computed for rainfall occurring in the East Asian Summer Monsoon (May-September, MJJAS). For the purposes of this study, the EASM is defined as the box bounded by latitudes 23°N-35°N and longitudes 105°E-113°E, which is a smaller region than canonically defined regions of the EASM. Our results (e.g. figure 4a) suggest an equal influence of classic vapor sources from the ISM (Indian Ocean) and EASM (Pacific Ocean) for this region. The boxed region was selected because it is loosely organized around the collection of southern and central Chinese speleothem records, and model-guided proxy interpretations is a main objective of this study.

Moisture streamlines

Tagged vapor streamlines are calculated for the mean flow of vapor between the respective tag region and the center of the Asian Monsoon box (Figure 1, 25° N, 110° E). Starting at the center of the EASM, column integrated tagged vapor flux vectors, linearly interpolated to the point 25° N, 110° E, are used to calculate the speed and direction of the tagged vapor parcel. Parcel speed and direction is calculated as the vapor-normalized vapor fluxes, or $\overline{UQ}/\overline{Q}$, where $\overline{UQ}$ is the seasonal mean, column integrated U*Q, and $\overline{Q}$ is the seasonal mean, column-integrated vapor amount. The upstream streamline coordinate is calculated using the speed and upstream direction over a time step of 1 hour with a simple cartesian approximation for change in latitude and longitude over the surface of the Earth. By using a time step of 1 hour, the distances traveled are on the order of 10^1 – 10^2 kms, which is small enough to allow for a plane-parallel approximation of the Earth's surface. Values of $\overline{UQ}/\overline{Q}$ are then linearly interpolated to the new upstream coordinate, and the processes is repeated until the backward trajectory reaches the tagged region.

Speleothem data

This study uses proxy data from central Chinese speleothems that have a MH and PI value, resulting in 6 records: Chongqing cave (Yang et al., 2019), Jiuxian cave (Cai et al., 2010), Sanbao cave (Dong et al., 2010), Lianhua cave (Cosford et al., 2008), and Dongge cave (Dykoski et al., 2005; Wang et al., 2005). Data are averaged along the speleothem record 100 years before and after the year 1850 CE for the PI and 4050 BCE for the MH.

Results

Model Validation

Model results are compared to the isotope and precipitation fields over the EASM from T20. There is little to no change in precipitation, and a negative change in precipitation isotope ratio, both of which are similar to T20 (Fig 2). While T20 does not specifically identify EASM mean $\Delta\delta^{18}O_p$, the analysis here indicates a change of -0.35‰ for the MHgs-MHdry in the EASM region, which is quantitatively similar to T20 contours over the same region. Figure 3 shows the MHdry (control), MHgs (experiment), and proxy values of $\Delta\delta^{18}O$ for the 5 speleothems shown in fig 2. While statistically significant changes between MHdry and MHgs are found in only 1 of 5 speleothem locations, all values for the MHgs experiment are more negative the MHdry values, indicating that the response to the GS forcing improves the model-proxy accuracy in the EASM. In the case of $\Delta\delta^{18}O_p$, our model-proxy RMSE decreases by 0.22‰ from the MHdry to the MHgs case.

$\Delta\delta^{18}O_{total}$ decomposition

Figure 4a shows f_{tag} for the gs (green dots) and dry (brown dots) experiments. Rainfall in the EASM is composed of a relatively even distribution of tags spanning the Indian and Pacific oceans, as well as continental tagged vapor from India, Africa and the Middle East, and China. This relatively even distribution of source vapor sets it apart from other northern hemisphere monsoons, which, generally speaking, source vapor from one prominent basin. In the EASM, the largest tag contributor is local evapotranspiration from the China tag (CHN), making up around 25% of the rainfall for both gs and dry cases, while the Arabian Sea (ARS), Bay of Bengal (BOB), Indian Ocean (INO), South China Sea (SCS), Philippine Sea (PPS), North Pacific (NPA), South East Asia (SEA), and India (IND) each make up anywhere from 5% to 12% of total EASM rainfall. For the gs-dry experiment difference, there is a general vapor sourcing shift away from Indian Ocean-adjacent tags (e.g. BOB, ARS, INO) and towards Pacific and continental sources (e.g. NPA, IND, AME,).

Figure 4b shows D_{tag}, the adjusted isotope ratio of the tagged precipitation. To first order, D_{tag} is negatively correlated with the nominal distance between tag location and

endpoint location. For example, vapor from the north Pacific tag (NPA), a distant source region, is more depleted than vapor from the South China Sea (SCS), a nearby source region. This is likely due to increased rainout-driven distillation on longer vapor transport paths. Additionally, almost all oceanic tags are more enriched during the gs and almost all continental tags are more depleted. Isotope ratio differences between different tags are an order of magnitude larger than the MHgs-MHdry differences for any individual tag. For example, the difference between the MHgs or MHdry NPA and SCS is approximately 10‰, whereas the difference between the MHgs NPA and MHdry NPA is approximately 1‰ (and equally true for SCS and all other tags). This suggests that vapor source location plays a larger role than the gs-dry climate changes in driving EASM isotope ratios. As such, one should expect that changes in the vapor source distribution (Δf_{tag}) play a larger role in shaping overall EASM $\Delta\delta^{18}O_p$.

Figure 4c shows the 3-term decomposition of the gs-dry $\Delta\delta^{18}O_{ASM}$, i.e. the f-effect (red dots), D-effect (blue dots), and covariance (black dots). The figure shows that the majority of $\Delta\delta^{18}O_{total}$ is driven by the f-effect for two tags, NPA and SPA, indicated by the relatively large negative value of the f-effect (red points) for these tags. Additionally, the local tag, CHN, has a large negative influence in both the f- and D-effects, and the BOB tag has a positive influence in the D-effect.

NPA and SPA tags

The NPA and SPA tags drive the overall EASM $\Delta\delta^{18}O_p$ towards the negative via the f-effect only. This result comes from the combined effect of positive values of Δf_{tag} and depleted values for the control (MHdry) D_{tag} for the NPA and SPA. Importantly, the value of ΔD_{tag} is not considered in the f-effect. The values for f_{NPA} increase from approximately 7.25% in the MHdry to 8.75% in the MHgs, for a fractional change of approximately 20.6%. For f_{SPA}, values increase from 2.12% to 2.63%, for a fractional change of 24%. Meanwhile, the values of D_{NPA} and D_{SPA} are negative in the MHdry control case (they are similarly negative in the MHgs case, but this value is not considered in the f-term calculation). Large negative values of D_{tag} "pull" the total isotope ratio towards the negative. By *greatly increasing* the vapor contribution of a *highly depleted* tag, the result is a strongly negative f-effect for these two tags, regardless of gs-dry

changes to the isotope ratios of these tags. The sum of the NPA and SPA f-effect values contribute -0.28‰ to the EASM $\Delta\delta^{18}O_{total}$ signal, which is achieved by shifting the distribution of vapor sourcing during the gs towards the relatively depleted Pacific, with no change in the isotope ratio of those sources and no other vapor source shifts. These findings are referred to as *f-driven* responses.

Physical interpretation of *f*-driven response for NPA

The tagging decomposition shown in Fig 4c indicates that a large portion of the EASM $\delta^{18}O_p$ signal is driven by a moisture source shift towards the highly depleted, non-coastal Pacific, specifically our NPA and SPA tags. The following addresses the question of what green Sahara-induced climate changes caused this shift by further inspection of the NPA tag. Fig. 5 shows the MH_{gs} - MH_{dry} fractional change in NPA column integrated vapor, $\Delta qfrac_{NPA} = (q_{gs,NPA} - q_{dry,NPA}) / q_{dry,NPA}$. $\Delta qfrac_{NPA}$ is approximately 28% over the proxy region, which resembles the approximate 20.6% increases in f_{NPA}. Positive $\Delta qfrac_{NPA}$ contours overlying the proxy region in central and eastern China are evidence that increases in f_{tag} for NPA (fig. 4a) are a direct result of an increase in column-integrated vapor of NPA origin. Quantifying the source of the positive $\Delta qfrac_{NPA}$ will provide the answer to why f_{NPA} increased in the tag decomposition.

Three possible shifts in the mean transport between the NPA tag region and the EASM proxy region are considered that could result in the positive $\Delta qfrac_{NPA}$ contours near the EASM found in fig. 5. First, an increase in source vapor supply, q_0, would result in increased Pacific vapor downstream of vapor transport pathways. Second, a decrease in cumulative precipitation of the tagged vapor, P_{NPA}, during vapor transport from the Pacific to the EASM would result in more downstream NPA vapor in the atmospheric column. Third, an increase in convergence of NPA vapor downstream of the tag region would increase the amount of vapor that makes it to the EASM. Convergence, in this case, is not the classic dynamical moisture flux convergence, $-\nabla\mathbf{U}\cdot q$, but instead a representation of the way that individual moisture trajectories combine into the MJJAS-mean trajectory used in this analysis. Positive convergence numerically represents the extent to which individual moisture trajectories tend to not spread out and tend to slow down, downstream of the tag region.

The three terms, q_0, P_{NPA}, and C_{NPA}, combine to form an analytical definition for the equilibrium q_{NPA}:

$$q_{NPA} \equiv q_0 + \sum_{l} [\, -P_{NPA}*\Delta t + C_{NPA}*\Delta t \,]$$

where "l" is the number of steps in the trajectory between evaporation source and precipitation location, calculated using the back trajectory algorithm. By summing -P*Δt and C*Δt over the streamline, the cumulative vapor removal via precipitation flux and the cumulative vapor addition by convergence is summed. Because evaporation of tagged vapor only occurs within the respective tag regions, there is no additional source of q_{NPA} along our defined vapor trajectories since they are defined to start at the moment the parcel of air leaves the tag region.

Table 2 shows MHdry, MHgs, and gs-dry difference for q_0, cumulative upstream rainfall, cumulative upstream convergence, and q_{final}, all in $Kg*m^{-2}$, for NPA. The table shows values at the point the trajectory leaves the NPA region, the EASM region, and the difference. For NPA, q_0 starts out 1.86 $Kg*m^{-2}$ higher during the gs, indicating an increase in initial vapor source availability. While increases in SSTs could induce increases in evaporation and therefor initial vapor source availability, this increase is specifically *not* driven by changes in SSTs because the only difference between the MHgs and MHdry simulations is the presence of vegetation in the MHgs experiment. Thus, the MHgs experiment increases q_0 for NPA via atmospheric forcing. Between the NPA region and the EASM, removal of NPA vapor via NPA rainout is greater in the MHgs case – 2.05 $Kg*m^{-2}$ more vapor is removed due to rainout. This effect offsets the q_0 signal – although there is more NPA vapor to begin with during the MHgs, the difference in removed during vapor transport because of increased rainout. Finally, there is more convergence (less divergence) during the MHgs along vapor transport pathways. The offsetting Δq_0 and ΔP_{NPA} signals, combined with the positive ΔC_{NPA}, results in the final positive $\Delta qfrac_{NPA}$ signal at the EASM of 1.3 $Kg*m^{-2}$.

Western vapor source influences on the CHN tag

For the CHN tag, changes to both the f- and D-effects are addressed because of their shared importance, unlike the NPA and SPA tags, where only the f-effect was important.

Because the EASM region is encompassed by the CHN tag region, answering why the CHN tag D-term decreases during the MHgs was already partially answered with the findings from of preceding section. However, the EASM region is only a subset of the CHN tag region. Changes to the D-effect of CHN are further identified by focusing on regions of CHN that do not include the EASM region. In west China there are large negative ΔD values, indicating that this region is of particular importance for further understanding why ΔD_{CHN} is negative. Figure 5 shows the tag decomposition for western China $\Delta\delta^{18}O_p$, which is defined as the EASM box shifted 7° west, such that the eastern edge of the original EASM box is placed at the western longitude. These results suggest that, in addition to patterns from figure 2, western China $\Delta\delta^{18}O_p$ is also reduced by the D-effect from IND (India) and AME (Africa and the Middle East) tags. This finding indicates that western China isotopes are partially driven by the depletion of rainfall composed of land-based evapotranspiration from west of western China (India, the Arabian peninsula, and Africa). ΔD_{IND} is -0.42‰ and ΔD_{AME} is -1.85‰; this, combined with the large relative importance of control f_{IND} and f_{AME}, results in the large negative D-effect (blue dots) for IND and AME. Fig 5 also indicates that western China $\Delta\delta^{18}O_p$ is strongly increased by the D-effect of BOB, but this increase is offset by more decreases in other tag regions and is not enough to result in positive $\Delta\delta^{18}O_p$ for western China.

For the f-effect of the CHN tag in the EASM decomposition, *decreases* in the amount of a *relatively enriched* tag result in the negative f-effect for CHN seen in figure 2c. That is to say, the vapor that the CHN tag supplies to the EASM in the control is relatively enriched compared to the total $\delta^{18}O_p$. When EASM rainfall is composed of less of this relatively enriched vapor during the MHgs, the $\Delta\delta^{18}O_p$ will subsequently be more negative, all else equal.

Discussion

A growing body of literature over the last few decades has agreed that the presence of a vegetated Sahara in simulations of the MH improves overall model-proxy fidelity in north Africa

and surrounding areas. In northern African and the Arabian peninsula, rainfall strongly increases as a result of increased flux of evapotranspiration due to the presence of plants, warming of the surface due to decreased albedo, and increased convergence of Atlantic vapor, all of which increase the likelihood for rainfall production. The West African Monsoon shifts north and intensifies as the newly vegetated Sahara shifts the latitude of maximum convergence north and increases the convergence of Atlantic evaporation onto the continent. Our results add to this body of literature, supporting the expected finding that a vegetated Sahara leads to increased Sahel, Sahara, and Arabian peninsula rainfall.

vegetation in the Sahara has also been shown to have teleconnected influences on much of the tropics. This study extended the work of Tabor et al. (2020) to investigate the influence of the green Sahara on the EASM by comparing the simulated $\delta^{18}O_p$ to isotope ratios of oxygen from speleothem calcite from the EASM. Our model results mimic those of T20 in rainfall isotope ratio depletion over the EASM associated with the green Sahara. These results partially support the mechanism proposed in T20: the depletion of EASM rainfall is partially attributable to an increase in highly depleted vapor from Africa and the Arabian Peninsula due to the newly vegetated land surface, as seen in figure 7 for the D-term of the AME tag. However, this influence is felt most strongly west of the speleothem region, which, while still in the EASM, is too far west to strongly influence the Chinese speleothems used in this study. A large part of the $\delta^{18}O_p$ signal came from the f-terms for the NPA and SPA tags, indicating that shifts in moisture source towards the Pacific Ocean and away from the Indian Ocean that occurred because of the GS were of prime importance. The influence of the f-term for NPA and SPA at the EASM highlights the potential role of seemingly negligible vapor sources. The vapor contribution of the SPA tag, for example, is 2.1% and 2.6% of the total EASM rainfall in the MHdry and MHgs simulations, respectively. Without the tag decomposition analysis, one may be inclined to ignorethis contribution. However, because SPA is highly depleted, small increases to its contribution can have a large impact on total isotope ratios. This was evident in the NPA and SPA tags, which were among the relatively depleted tags in the MH experiments.

The importance of the f-term found in figure 4 also demonstrates the strong influence that the dimension of space has on EASM isotope ratios, as opposed to the climate changes

that drive, for instance, the MHgs - MHdry isotope ratio differences for the same tag. In this sense, one could imagine a situation in which every tag becomes more enriched during the MHgs compared to the MHdry, i.e. $\Delta\delta_{tag} < 0$ for all tags. However, by changing the EASM vapor sourcing towards tags with relatively low $\delta^{18}O_p$ and away from tags with relatively high $\delta^{18}O_p$ (i.e. by changing f_{tag} to preferentially sample from tags that have negative D on average), $\Delta\delta_{ASM}$ will be negative. Thus, these results suggest that changes to the isotope ratios of rainfall in the EASM encode information about shifts in moisture sourcing, even for very distant and low-contributing regions like the eastern North Pacific. While only identified with the one model used in this study, the increased convergence of far-away Pacific vapor should introduce a negative isotope anomaly in other isotope-enabled GCM simulations because such vapor will have undergone large amounts of rainfall along moisture trajectories, and by increasing the relative fraction that a far-away, highly negative source contributes to total rainfall at the EASM, total isotope ratios will be more negative.

Increased values of the f-effect for NPA and SPA resemble the expected "niña-like" mean state shift induced by previous GS studies (Pausata et al., 2017; Giffiths et al., 2020). In a niña-like mean state, the Walker cell is shifted west, establishing anomalously high surface convergence over the Indo-Pacific Warm Pool and enhanced easterly flow from the central Pacific (i.e. the region shared by the NPA and SPA tags) to Asia. This paradigm sets up a shift in vapor sourcing for Pacific-adjacent regions, like East and South East Asia, towards more Pacific and less Indian vapor contribution. The large contribution of the NPA and SPA f-effect to total EASM $\delta^{18}O_p$ indicates that a shift towards a niña-like mean state (or, equivalently, a westward shift in the Walker cell), amplified by the presence of the GS, is a major contributing factor in increased model-proxy agreement for EASM $\delta^{18}O_p$. Thus, Pacific-influenced proxies of $\delta^{18}O_p$, such as the speleothem records used in this study, can provide the paleoclimate context for northern African vegetation via physical teleconnections with ENSO variability in the Pacific.

The EASM response to GS forcing offers a unique and powerful opportunity to understand model-proxy mismatch during the MH. Proxy $\delta^{18}O_p$ records from the EASM are depleted during the MH compared to the PI, which is often interpreted by proxy paleoclimatologists using the amount effect, which suggests, to first order, that EASM

precipitation increased during the MH (Hu et al., 2008; Cossford et al., 2008; Liu et al., 2014; Liu et al., 2015; Yang et al., 2020), although the best interpretation of EASM isotope proxies is still debated (Maher, 2008; Maher & Thompson, 2012; Chen et al., 2016), and the physical mechanisms that create the amount effect are poorly understood (Risi et al., 2009; Field et al., 2010, Moore et al., 2014; Konecky et al., 2019). On the other hand, most PMIP models do not simulate increased EASM precipitation during the MH (Zhao & Harrison, 2012; Braconnot et al., 2012), even with proxy-appropriate GS and reduced dust forcing applied. In fact, in many cases GS and reduced dust experiments lead to reduced EASM rainfall relative to the control MH (e.g. Sun et al., 2019; Tabor et al., 2020).

Simulations of stable isotope distributions by T20 showed a GS conditions resulted in decreased $\delta^{18}O_p$ in the EASM, and brings model estimates into better agreement with the majority of EASM isotope proxies. However, the classic interpretation of $\delta^{18}O_p$-based proxies, i.e. that decreases in isotope ratio correspond with increases in rainfall amount, is not validated by the model's precipitation results (i.e. Sun et al., 2019). Here it was found that MH simulations without GS vegetation have larger model-proxy mismatches than those that include GS vegetation in EASM $\delta^{18}O_p$ because the presence of the GS increases the easterly flux of Pacific vapor onto Asia. Even though model results were improved compared to the proxies when GS vegetation is included, there are still obvious errors (e.g. Fig. 2.2). By adding GS vegetation, model-proxy $\delta^{18}O_p$ differences improved by approximately 0.33‰, but the model is still anywhere from approximately 0.2‰, – 1.5‰ higher than the proxy $\delta^{18}O$. This suggests that the EASM isotope response to GS forcing is still too weak, but further research is needed to identify the source of these continued model-proxy discrepancies. For instance, by increasing the precipitation response in northern Africa as a response to GS forcing, one may expect to see a coincident decrease in EASM $\delta^{18}O$. If this were the case then the response to GS forcing in northern Africa is poorly simulated by CESM, or the prescribed vegetation is not sufficient to induce the necessary feedbacks to support the wetter environment. Other aspects of the MH simulation may be restricting the proxy-suggested simulation of EASM rainfall despite providing correct GS vegetation. Finally, EASM speleothem proxies may not be a faithful recorder of the

actual summertime average climate. For instance, if the cave specimens preferentially incorporate rainfall from a month where $\delta^{18}O_p$ is very negative, this would bias the speleothems away from the annual mean.

Bibliography

Adkins, J., deMenocal, P., & Eshel, G. (2006). The “African humid period” and the record of marine upwelling from excess 230Th in Ocean Drilling Program Hole 658C. *Paleoceanography*, *21*(4). https://doi.org/10.1029/2005PA001200

Amaral, P. G. C., Vincens, A., Guiot, J., Buchet, G., Deschamps, P., Doumnang, J.-C., & Sylvestre, F. (2013). Palynological evidence for gradual vegetation and climate changes during the African Humid Period termination at 13°N from a Mega-Lake Chad sedimentary sequence. *Climate of the Past*, *9*(1), 223–241. https://doi.org/10.5194/cp-9-223-2013

Boos, W. R., & Korty, R. L. (2016). Regional energy budget control of the intertropical convergence zone and application to mid-Holocene rainfall. *Nature Geoscience*, *9*(12), 892–897. https://doi.org/10.1038/ngeo2833

Braconnot, P., Harrison, S. P., Kageyama, M., Bartlein, P. J., Masson-Delmotte, V., Abe-Ouchi, A., Otto-Bliesner, B., & Zhao, Y. (2012). Evaluation of climate models using palaeoclimatic data. *Nature Climate Change*, *2*(6), 417–424. https://doi.org/10.1038/nclimate1456

Brovkin, V., Claussen, M., Petoukhov, V., & Ganopolski, A. (1998). On the stability of the atmosphere-vegetation system in the Sahara/Sahel region. *Journal of Geophysical Research: Atmospheres*, *103*(D24), 31613–31624. https://doi.org/10.1029/1998JD200006

Cai, Y., Tan, L., Cheng, H., An, Z., Edwards, R. L., Kelly, M. J., Kong, X., & Wang, X. (2010). The variation of summer monsoon precipitation in central China since the last deglaciation. *Earth and Planetary Science Letters*, *291*(1), 21–31. https://doi.org/10.1016/j.epsl.2009.12.039

Chen, J., Rao, Z., Liu, J., Huang, W., Feng, S., Dong, G., Hu, Y., Xu, Q., & Chen, F. (2016). On the timing of the East Asian summer monsoon maximum during the Holocene—Does the speleothem oxygen isotope record reflect monsoon rainfall variability? *Science China Earth Sciences*, *59*(12), 2328–2338. https://doi.org/10.1007/s11430-015-5500-5

Claussen, M., Dallmeyer, A., & Bader, J. (2017, March 29). *Theory and Modeling of the African Humid Period and the Green Sahara*. Oxford Research Encyclopedia of Climate Science. https://doi.org/10.1093/acrefore/9780190228620.013.532

Claussen, M., & Gayler, V. (1997). The Greening of the Sahara during the Mid-Holocene: Results of an Interactive Atmosphere-Biome Model. *Global Ecology and Biogeography Letters*, *6*(5), 369–377. https://doi.org/10.2307/2997337

Cosford, J., Qing, H., Eglington, B., Mattey, D., Yuan, D., Zhang, M., & Cheng, H. (2008). East Asian monsoon variability since the Mid-Holocene recorded in a high-resolution, absolute-dated aragonite speleothem from eastern China. *Earth and Planetary Science Letters*, *275*(3), 296–307. https://doi.org/10.1016/j.epsl.2008.08.018

Damnati, B. (2000). Holocene lake records in the Northern Hemisphere of Africa. *Journal of African Earth Sciences*, *31*(2), 253–262. https://doi.org/10.1016/S0899-5362(00)00089-0

Demenocal, P., & Tierney, J. E. (2012). African Humid Periods paced by Earth's orbital changes. *Nature Education*, *3*, 12.

Deser, C., Phillips, A. S., & Alexander, M. A. (2010). Twentieth century tropical sea surface temperature trends revisited. *Geophysical Research Letters*, *37*(10). https://doi.org/10.1029/2010GL043321

Doherty, R., Kutzbach, J., Foley, J., & Pollard, D. (2000). Fully coupled climate/dynamical vegetation model simulations over Northern Africa during the mid-Holocene. *Climate Dynamics*, *16*(8), 561–573. https://doi.org/10.1007/s003820000065

Dong, J., Wang, Y., Cheng, H., Hardt, B., Edwards, R. L., Kong, X., Wu, J., Chen, S., Liu, D., Jiang, X., & Zhao, K. (2010). A high-resolution stalagmite record of the Holocene East Asian monsoon from Mt Shennongjia, central China. *The Holocene*, *20*(2), 257–264. https://doi.org/10.1177/0959683609350393

Dykoski, C. A., Edwards, R. L., Cheng, H., Yuan, D., Cai, Y., Zhang, M., Lin, Y., Qing, J., An, Z., & Revenaugh, J. (2005). A high-resolution, absolute-dated Holocene and deglacial Asian monsoon record from Dongge Cave, China. *Earth and Planetary Science Letters*, *233*(1), 71–86. https://doi.org/10.1016/j.epsl.2005.01.036

Eyring, V., Bony, S., Meehl, G. A., Senior, C. A., Stevens, B., Stouffer, R. J., & Taylor, K. E. (2016). Overview of the Coupled Model Intercomparison Project Phase 6 (CMIP6) experimental design and organization. *Geoscientific Model Development*, *9*(5), 1937–1958. https://doi.org/10.5194/gmd-9-1937-2016

Fiorella, R. P., Siler, N., Nusbaumer, J., & Noone, D. C. (2021). Enhancing Understanding of the Hydrological Cycle via Pairing of Process-Oriented and Isotope Ratio Tracers. *Journal of Advances in Modeling Earth Systems*, *13*(10), e2021MS002648. https://doi.org/10.1029/2021MS002648

Griffiths, M. L., Johnson, K. R., Pausata, F. S. R., White, J. C., Henderson, G. M., Wood, C. T., Yang, H., Ersek, V., Conrad, C., & Sekhon, N. (2020). End of Green Sahara amplified mid- to late Holocene megadroughts in mainland Southeast Asia. *Nature Communications*, *11*(1), 4204. https://doi.org/10.1038/s41467-020-17927-6

Harrison, S. P., Bartlein, P. J., Brewer, S., Prentice, I. C., Boyd, M., Hessler, I., Holmgren, K., Izumi, K., & Willis, K. (2014). Climate model benchmarking with glacial and mid-Holocene climates. *Climate Dynamics*, *43*(3), 671–688. https://doi.org/10.1007/s00382-013-1922-6

Hoelzmann, P., Keding, B., Berke, H., Kröpelin, S., & Kruse, H.-J. (2001). Environmental change and archaeology: Lake evolution and human occupation in the Eastern Sahara during the Holocene. *Palaeogeography, Palaeoclimatology, Palaeoecology*, *169*(3), 193–217. https://doi.org/10.1016/S0031-0182(01)00211-5

Hu, C., Henderson, G. M., Huang, J., Xie, S., Sun, Y., & Johnson, K. R. (2008). Quantification of Holocene Asian monsoon rainfall from spatially separated cave records. *Earth and Planetary Science Letters*, *266*(3), 221–232. https://doi.org/10.1016/j.epsl.2007.10.015

Hu, H., & Dominguez, F. (2015). Evaluation of Oceanic and Terrestrial Sources of Moisture for the North American Monsoon Using Numerical Models and Precipitation Stable Isotopes. In Journal of Hydrometeorology (Vol. 16, Issue 1, pp. 19–35). American Meteorological Society. https://doi.org/10.1175/jhm-d-14-0073.1

Hurrell, J. W., Holland, M. M., Gent, P. R., Ghan, S., Kay, J. E., Kushner, P. J., Lamarque, J.-F., Large, W. G., Lawrence, D., Lindsay, K., Lipscomb, W. H., Long, M. C., Mahowald, N., Marsh, D. R., Neale, R. B., Rasch, P., Vavrus, S., Vertenstein, M., Bader, D., … Marshall, S. (2013). The Community Earth System Model: A Framework for Collaborative Research. *Bulletin of the American Meteorological Society*, *94*(9), 1339–1360. https://doi.org/10.1175/BAMS-D-12-00121.1

Joussaume, S., Taylor, K. E., Braconnot, P., Mitchell, J. F. B., Kutzbach, J. E., Harrison, S. P., Prentice, I. C., Broccoli, A. J., Abe-Ouchi, A., Bartlein, P. J., Bonfils, C., Dong, B., Guiot, J., Herterich, K., Hewitt, C. D., Jolly, D., Kim, J. W., Kislov, A., Kitoh, A., … Wyputta, U. (1999). Monsoon changes for 6000 years ago: Results of 18 simulations from the Paleoclimate Modeling Intercomparison Project (PMIP). *Geophysical Research Letters*, *26*(7), 859–862. https://doi.org/10.1029/1999GL900126

Knorr, W., & Schnitzler, K.-G. (2006). Enhanced albedo feedback in North Africa from possible combined vegetation and soil-formation processes. *Climate Dynamics*, *26*(1), 55–63. https://doi.org/10.1007/s00382-005-0073-9

Larrasoaña, J. C., Roberts, A. P., & Rohling, E. J. (2013). Dynamics of Green Sahara Periods and Their Role in Hominin Evolution. *PLOS ONE*, *8*(10), e76514. https://doi.org/10.1371/journal.pone.0076514

Lawrence, D. M., Oleson, K. W., Flanner, M. G., Thornton, P. E., Swenson, S. C., Lawrence, P. J., Zeng, X., Yang, Z.-L., Levis, S., Sakaguchi, K., Bonan, G. B., & Slater, A. G. (2011). Parameterization improvements and functional and structural advances in Version 4 of the Community Land Model. *Journal of Advances in Modeling Earth Systems*, *3*(1). https://doi.org/10.1029/2011MS00045

Levis, S., Bonan, G. B., & Bonfils, C. (2004). Soil feedback drives the mid-Holocene North African monsoon northward in fully coupled CCSM2 simulations with a dynamic vegetation model. *Climate Dynamics*, *23*(7), 791–802. https://doi.org/10.1007/s00382-004-0477-y

Liu, D., Wang, Y., Cheng, H., Edwards, R. L., & Kong, X. (2015). Cyclic changes of Asian monsoon intensity during the early mid-Holocene from annually-laminated stalagmites, central China. *Quaternary Science Reviews*, *121*, 1–10. https://doi.org/10.1016/j.quascirev.2015.05.003

Liu, Z., Wen, X., Brady, E. C., Otto-Bliesner, B., Yu, G., Lu, H., Cheng, H., Wang, Y., Zheng, W., Ding, Y., Edwards, R. L., Cheng, J., Liu, W., & Yang, H. (2014). Chinese cave records and the East Asia Summer Monsoon. *Quaternary Science Reviews*, *83*, 115–128. https://doi.org/10.1016/j.quascirev.2013.10.021

Maher, B. A. (2008). Holocene variability of the East Asian summer monsoon from Chinese cave records: A re-assessment. *The Holocene*, *18*(6), 861–866. https://doi.org/10.1177/0959683608095569

Maher, B. A., & Thompson, R. (2012). Oxygen isotopes from Chinese caves: Records not of monsoon rainfall but of circulation regime. *Journal of Quaternary Science*, *27*(6), 615–624. https://doi.org/10.1002/jqs.2553

Nusbaumer, J., Alexander, P. M., LeGrande, A. N., & Tedesco, M. (2019). Spatial Shift of Greenland Moisture Sources Related to Enhanced Arctic Warming. *Geophysical Research Letters*, *46*(24), 14723–14731. https://doi.org/10.1029/2019GL084633

Nusbaumer, J., & Noone, D. (2018). Numerical Evaluation of the Modern and Future Origins of Atmospheric River Moisture Over the West Coast of the United States. *Journal of Geophysical Research: Atmospheres*, *123*(12), 6423–6442. https://doi.org/10.1029/2017JD028081

Nusbaumer, J., Wong, T. E., Bardeen, C., & Noone, D. (n.d.). Evaluating hydrological processes in the Community Atmosphere Model Version 5 (CAM5) using stable isotope ratios of water. *Journal of Advances in Modeling Earth Systems*, *9*(2), 949–977. https://doi.org/10.1002/2016MS000839

Otto-Bleisner, B. L., Braconnot, P., Harrison, S. P., Lunt, D. J., Abe-Ouchi, A., Albani, S., Bartlein, P. J., Capron, E., Carlson, A. E., Dutton, A., Fischer, H., Goelzer, H., Govin, A., Haywood, A., Joos, F., Legrande, A. N., Lipscomb, W. H., Lohmann, G., Mahowald, N., … Renssen, H. (2016). The PMIP4 contribution to CMIP6 – Part 2: Two interglacials, scientific objective and experimental design for Holocene and last interglacial simulations. *Geoscientific Model Development Discussions*, *10.5194/gmd-2016–279*. http://centaur.reading.ac.uk/68688/

Patricola, C. M., & Cook, K. H. (2007). Dynamics of the West African Monsoon under Mid-Holocene Precessional Forcing: Regional Climate Model Simulations. *Journal of Climate*, *20*(4), 694–716. https://doi.org/10.1175/JCLI4013.1

Pausata, F. S. R., Gaetani, M., Messori, G., Berg, A., Maia de Souza, D., Sage, R. F., & deMenocal, P. B. (2020). The Greening of the Sahara: Past Changes and Future Implications. *One Earth*, *2*(3), 235–250. https://doi.org/10.1016/j.oneear.2020.03.002

Pausata, F. S. R., Zhang, Q., Muschitiello, F., Lu, Z., Chafik, L., Niedermeyer, E. M., Stager, J. C., Cobb, K. M., & Liu, Z. (2017). Greening of the Sahara suppressed ENSO activity during the mid-Holocene. *Nature Communications*, *8*, ncomms16020. https://doi.org/10.1038/ncomms16020

Ritchie, J. C., Eyles, C. H., & Haynes, C. V. (1985). Sediment and pollen evidence for an early to mid-Holocene humid period in the eastern Sahara. *Nature*, *314*(6009), 352–355. https://doi.org/10.1038/314352a0

Rodwell, M. J., & Hoskins, B. J. (1996). Monsoons and the dynamics of deserts. *Quarterly Journal of the Royal Meteorological Society*, *122*(534), 1385–1404. https://doi.org/10.1002/qj.49712253408

Rodwell, M. J., & Hoskins, B. J. (2001). Subtropical Anticyclones and Summer Monsoons. *Journal of Climate*, *14*(15), 3192–3211. https://doi.org/10.1175/1520-0442(2001)014<3192:SAASM>2.0.CO;2

Singh, H. A., Bitz, C. M., Nusbaumer, J., & Noone, D. C. (2016). A mathematical framework for analysis of water tracers: Part 1: Development of theory and application to the preindustrial mean state. *Journal of Advances in Modeling Earth Systems*, *8*(2), 991–1013. https://doi.org/10.1002/2016MS000649

Singh, H. K. A., Bitz, C. M., Donohoe, A., Nusbaumer, J., & Noone, D. C. (2016). A Mathematical Framework for Analysis of Water Tracers. Part II: Understanding Large-Scale Perturbations in the Hydrological Cycle due to CO2 Doubling. *Journal of Climate*, *29*(18), 6765–6782. https://doi.org/10.1175/JCLI-D-16-0293.1

Skinner, C. B., & Poulsen, C. J. (2016). The role of fall season tropical plumes in enhancing Saharan rainfall during the African Humid Period. *Geophysical Research Letters*, *43*(1), 349–358. https://doi.org/10.1002/2015GL066318

Stojanowski, C. M., & Knudson, K. J. (2014). Changing patterns of mobility as a response to climatic deterioration and aridification in the middle Holocene southern Sahara. *American Journal of Physical Anthropology*, *154*(1), 79–93. https://doi.org/10.1002/ajpa.22474

Sun, W., Wang, B., Zhang, Q., Pausata, F. S. R., Chen, D., Lu, G., Yan, M., Ning, L., & Liu, J. (2019). Northern Hemisphere Land Monsoon Precipitation Increased by the Green Sahara During Middle Holocene. *Geophysical Research Letters*, *46*(16), 9870–9879. https://doi.org/10.1029/2019GL082116

Tabor, C., Otto-Bliesner, B., & Liu, Z. (2020). Speleothems of South American and Asian Monsoons Influenced by a Green Sahara. *Geophysical Research Letters*, *47*(22), e2020GL089695. https://doi.org/10.1029/2020GL089695

Tabor, C. R., Otto-Bliesner, B. L., Brady, E. C., Nusbaumer, J., Zhu, J., Erb, M. P., Wong, T. E., Liu, Z., & Noone, D. (2018). Interpreting Precession-Driven δ18O Variability in the South Asian Monsoon Region. *Journal of Geophysical Research: Atmospheres*, *123*(11), 5927–5946. https://doi.org/10.1029/2018JD028424

Thompson, A. J., Skinner, C. B., Poulsen, C. J., & Zhu, J. (2019). Modulation of Mid-Holocene African Rainfall by Dust Aerosol Direct and Indirect Effects. *Geophysical Research Letters*, *46*(7), 3917–3926. https://doi.org/10.1029/2018GL081225

Tierney, J. E., Pausata, F. S. R., & deMenocal, P. B. (2017). Rainfall regimes of the Green Sahara. *Science Advances*, *3*(1), e1601503. https://doi.org/10.1126/sciadv.1601503

Wang, S., Ge, Q., Wang, F., Wen, X., & Huang, J. (2013). Abrupt climate changes of Holocene. *Chinese Geographical Science*, *23*(1), 1–12. https://doi.org/10.1007/s11769-013-0591-z

Wang, Y., Cheng, H., Edwards, R. L., He, Y., Kong, X., An, Z., Wu, J., Kelly, M. J., Dykoski, C. A., & Li, X. (2005). The Holocene Asian Monsoon: Links to Solar Changes and North Atlantic Climate. *Science*, *308*(5723), 854–857. https://doi.org/10.1126/science.1106296

Wanner, H., Beer, J., Bütikofer, J., Crowley, T. J., Cubasch, U., Flückiger, J., Goosse, H., Grosjean, M., Joos, F., Kaplan, J. O., Küttel, M., Müller, S. A., Prentice, I. C., Solomina, O., Stocker, T. F., Tarasov, P., Wagner, M., & Widmann, M. (2008). Mid- to Late Holocene climate change: An overview. *Quaternary Science Reviews*, *27*(19), 1791–1828. https://doi.org/10.1016/j.quascirev.2008.06.013

Watrin, J., Lézine, A.-M., & Hély, C. (2009). Plant migration and plant communities at the time of the "green Sahara." *Comptes Rendus Geoscience*, *341*(8), 656–670. https://doi.org/10.1016/j.crte.2009.06.007

Wong, T. E., Nusbaumer, J., & Noone, D. C. (n.d.). Evaluation of modeled land-atmosphere exchanges with a comprehensive water isotope fractionation scheme in version 4 of the Community Land Model. *Journal of Advances in Modeling Earth Systems*, *9*(2), 978–1001. https://doi.org/10.1002/2016MS000842

Yang, X., Liu, R., Zhang, R., Wang, B., Zhang, R., & Yan, Y. (2020). A stalagmite δ18O record from Jinfo Cave, southern China reveals early-mid holocene variations in the East Asian Summer Monsoon. *Quaternary International*, *537*, 61–68. https://doi.org/10.1016/j.quaint.2020.01.002

Yang, X., Yang, H., Wang, B., Huang, L.-J., Shen, C.-C., Edwards, R. L., & Cheng, H. (2019). Early-Holocene monsoon instability and climatic optimum recorded by Chinese stalagmites. *The Holocene*, *29*(6), 1059–1067. https://doi.org/10.1177/0959683619831433

Zhao, Y., & Harrison, S. P. (2012). Mid-Holocene monsoons: A multi-model analysis of the inter-hemispheric differences in the responses to orbital forcing and ocean feedbacks. *Climate Dynamics*, *39*(6), 1457–1487. https://doi.org/10.1007/s00382-011-1193-z

Figures & Tables

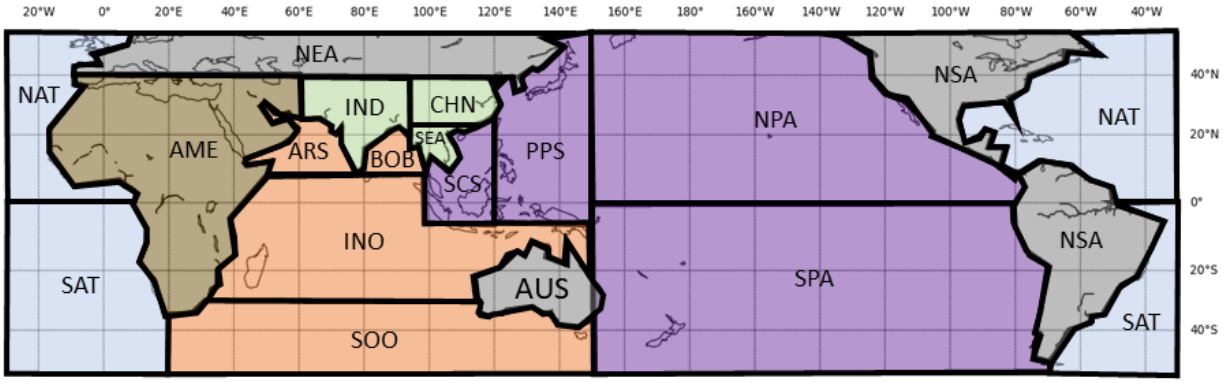

Figure 2.1 The tag layout, colored by shared regions. Several land surfaces are not specifically outlined, but belong to a land-based tag. The maritime continent and the Philippines are included in the SEA tag, New Zealand in the AUS tag, and Madagascar in the AME tag. Tag metadata is shown in Table 2.1.

Tag	Long name	Location (S,N,E,W)	Surface
ARS	Arabian Sea	8, 30, 40, 80	Ocean
BOB	Bay of Bengal	8, 23.5, 80, 100	Ocean
INO	Indian Ocean	-8, 8, 20, 100 -30, -8, 20, 150	Ocean
SOO	Southern Ocean	-90, -20, 20, 150	Ocean
SCS	South China Sea	-8, 45, 100, 120	Ocean
PPS	Philippine Sea	-8, 90, 120, 150	Ocean
NPA	North Pacific	0, 90, 150, 255 0, 15, 255, 285	Ocean
SPA	South Pacific	-90, 0, 150, 290	Ocean
NAT	North Atlantic	20, 90, 260, 40 0, 20, 280, 40	Ocean
SAT	South Atlantic	-90, 0, 290, 20	Ocean
CHN	China	23.5, 40, 95, 160	Land
SEA	Southeast Asia	-8, 23.5, 95, 160	Land
IND	India	5 40, 60, 95	Land
AME	Africa + Mid East	-40, 40, 330, 60	Land
NEA	Northern Eurasia	40, 90, 330, 180	Land
NSA	N+S America	-90, 90, 180, 330	Land
AUS	Australia + NZ	-45, -8, 95, 180	Land

Table 2.1 Tag layout metadata. Locations are sets of 4 numbers, representing the south and north latitude, and east and west longitude, in that order. Locations with two sets of numbers are tag boxes defined by the combination of two boxes due to their irregular shape.

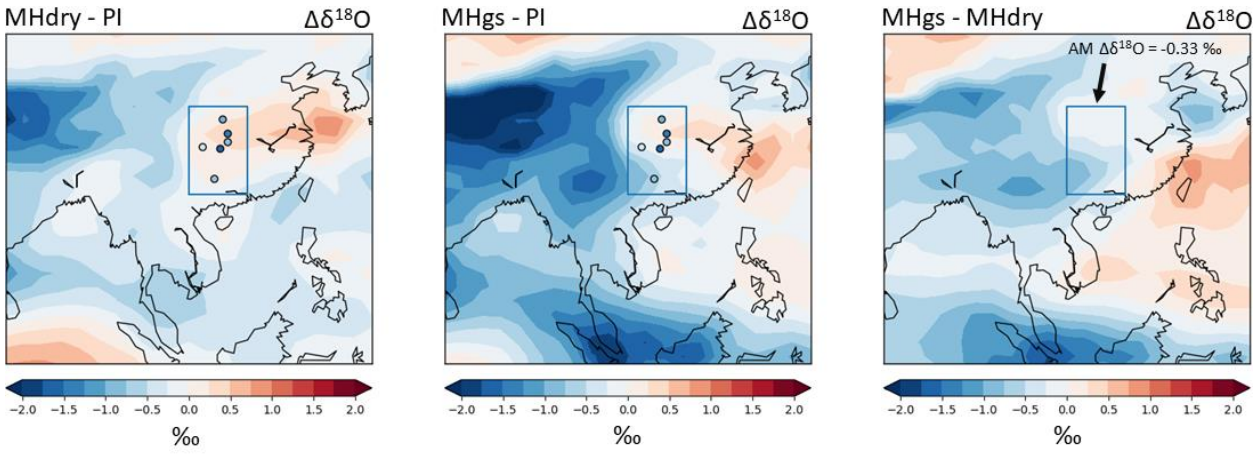

Figure 2.2 MJJAS mean simulated $\Delta\delta^{18}O_p$ with speleothem MH-PI values. Left: Mhdry – PI; center: MHgs – PI; right: MHgs – Mhdry. Colored contours are isotope ratio differences (in ‰). Dots are locations of 5 Chinese speleothems, colored using the same scale, for the MH – PI difference. Blue box outlines the EASM region used in this study. From south to north, speleothem records are: Dongge cave (Dykoski et al., 2005; Wang et al., 2005), Chongqing cave (west, Yang et al., 2019), Lianhua cave (east, Cosford et al., 2008), Sanbao cave (Dong et al., 2010), Jiuxian cave (Cai et al., 2010)

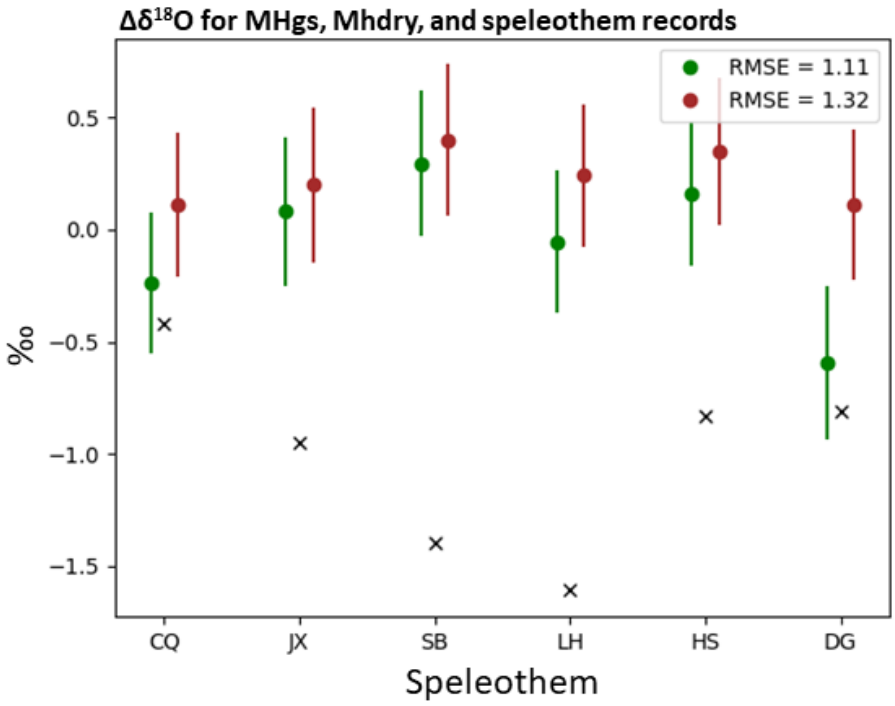

Figure 2.3 MJJAS mean Δδ18Op of the 5 EASM speleothem locations for the MHdry – PI (brown), MHgs – PI (green), and proxy values (black crosses). Simulated results are shown with +- 1.96*σ2 bars. Speleothems abbreviations are Chongqing (CQ), Jiuxian (JX), Sanbao (SB), Lianghua (LH), Heshang (HS), and Dongge (DG)

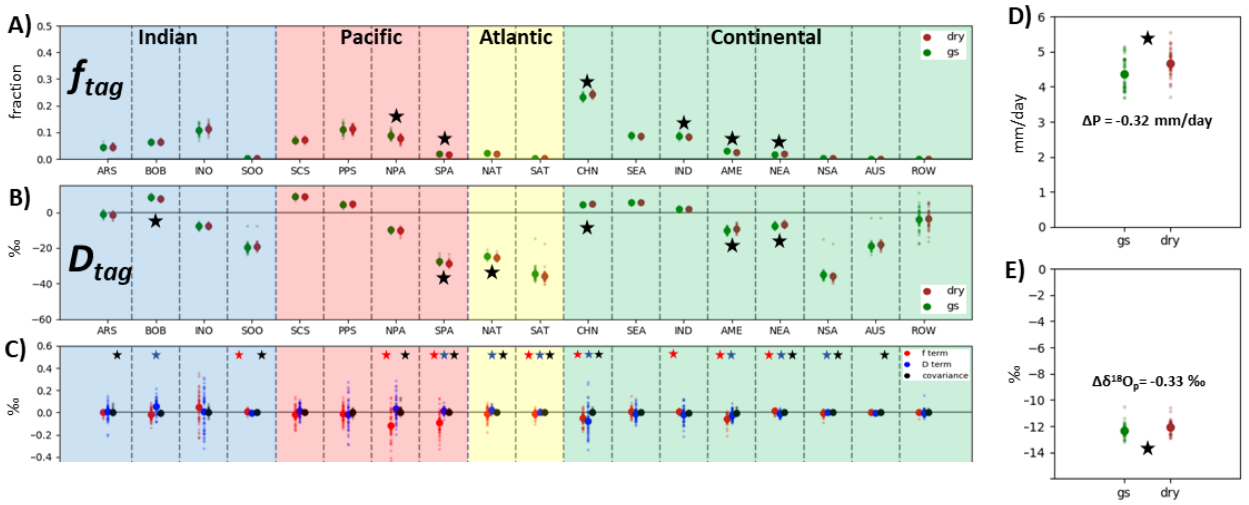

Figure 2.4 The MJJAS mean tag decomposition of $\Delta\delta^{18}O_p$ for the EASM region. A) F_{tag}, B) D_{tag}, and C) the three-term decomposition where f-term are red dots, D-term blue dots, and covariance black dots. D) The precipitation amount, P_{total} for the EASM MHgs and MHdry, and E) the change in $\delta^{18}O_p$ of total EASM precipitation for gs and dry. In all subfigures, the large dot is the 50-year mean value and the smaller background dots are the individual year values. In (A), (B), (D), and (E), black stars denote that the gs-dry difference is statistically significant ($p < 0.05$). In (C) red, blue, and black stars denote when the f-term, D-term, and covariance are significantly different than zero ($p < 0.05$).

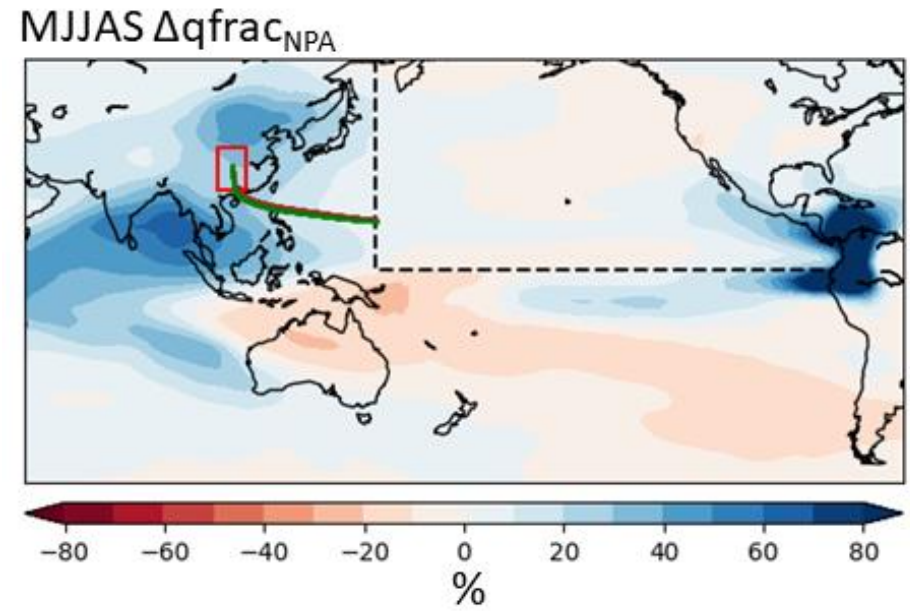

Figure 2.5 MJJAS fractional change in q_{NPA} from the MHdry to MHgs, $\Delta qfrac_{NPA}$. Fractional change is calculated as $(q^{gs}_{NPA} - q^{dry}_{NPA}) / q^{dry}_{NPA}$. Black dashed lines denote the tag region for NPA (north Pacific). Red box indicates the EASM region. Green and brown lines connecting the EASM to the NPA tag region denote the back-trajectory calculated between the two regions.

NPA → EASM trajectory	MHgs	MHdry	gs – dry
q_0 (at exit point of NPA)	38.06	36.20	1.86
Cumulative upstream precipitation	27.96	25.91	2.05
Cumulative upstream convergence	-4.33	-5.82	1.49
q_{final} (at center of EASM region)	5.77	4.47	1.30

Table 2.2 The 3 components of the vapor budget along the NPA vapor transport pathway. Calculated as $q_0 - \sum P + \sum C = q_{final}$. All variables are in $Kg*m^{-2}$.

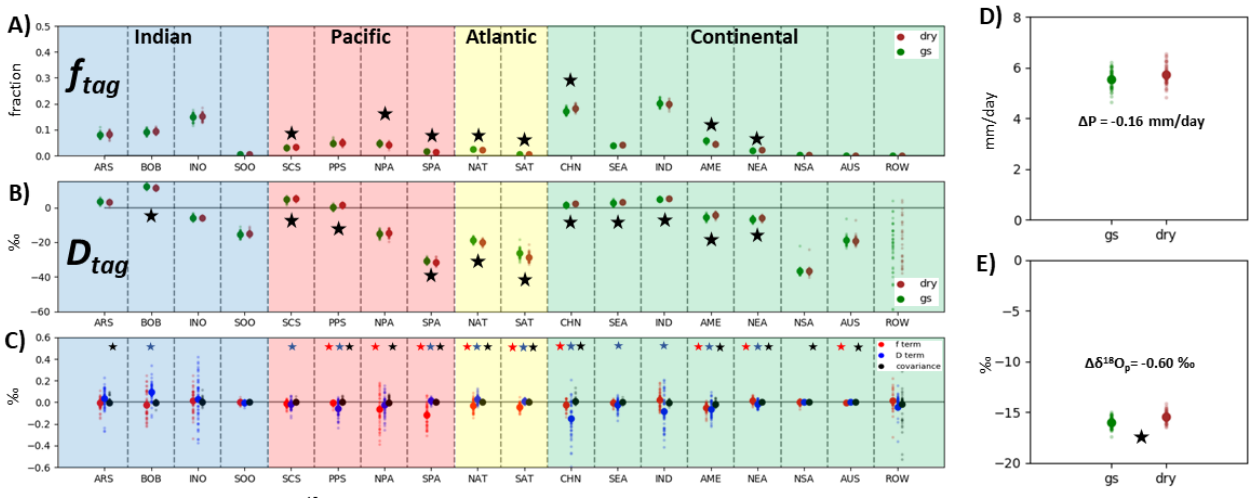

Figure 2.6 The tag decomposition of $\Delta\delta^{18}O_p$ as in Fig. 2.4, but for Western China, defined by the EASM box shifted 8° west.

Chapter 3: D-O variability in Greenland Summit $\delta^{18}O_p$ controlled by southern extent of sea ice in the north Atlantic during the last glacial.

Kyle Niezgoda*
Christo Buizert
Kaden Martin
David Noone

Abstract

Dansgaard-Oeschger (DO) events, also known as Greenland interstadial (GI) events, represent some of the most rapid local warming events in the paleoclimate record, and manifest as 25 distinct peaks in the oxygen and hydrogen isotope ratios of Greenland ice cores ($\delta^{18}O_{ice}$ and δD_{ice}, or δ_{ice} for short). Recent work has linked changes in sea ice concentration in the North Atlantic to paleoclimate changes in Greenland δ_{ice}, but this relationship is still poorly understood. In modern day studies of Greenland, δ_{ice} is strongly correlated to Greenland temperature. However, the δ_{snow} – temperature relationship is complicated in studies of the past because the correlation changes in time, and because large changes in sea ice extent in the north Atlantic can reshape the moisture source distribution for Greenland precipitation. This study constrains the δ_{ice}-sea ice relationship with the use of sea-ice experiments in a climate model setup. Using the isotope-enabled Community Atmosphere Model (iCAM), two sea ice forcing experiments are carried out: a low sea ice, warm, interstadial climate state (LGM_{GI}) and a high sea ice, cold, stadial climate state (LGM_{GS}). Water tracers are added to iCAM to detail the contribution of various moisture source regions to Greenland snowfall. A technique for tag-based decomposition of Greenland precipitation shows how changes in Greenland δ_{ice} during GI events can be largely explained by the dramatic increase of moisture sourcing from the Greenland, Norwegian, and Icelandic (GIN) seas and the north Atlantic during the wintertime (Dec. through Feb., DJF). This increase is modulated by the presence of sea ice in the GIN + north Atlantic region, because sea ice acts as a cap on the ocean, preventing evaporation. These results provide important context for sea-ice reconstructions of the north Atlantic during DO events. This work expands upon previous findings indicating that Greenland ice core DO signals are highly related to the amount of evaporation occurring in the north Atlantic by providing a

quantitative assessment of the role of sea-ice location in the North Atlantic on the isotope ratio of snowfall in Greenland.

Introduction

Greenland ice cores have provided an irreplaceable wealth of knowledge on the state of the climate during the most recent glacial period. Among the most well-known findings is the millennial-scale variability of North Atlantic and Greenland temperature (Bond et al., 1997; Schulz, 2002; Voelker, 2002; Genty et al., 2003), which is punctuated by anomalous warm events known as Dansgaard-Oeschger (DO) events (Dansgaard et al., 1982; Dansgaard et al., 1993). During DO events, Greenland and the North Atlantic experienced rapid warming in as little as a few decades (Severinghaus & Brook, 1999; Lang et al., 1999). DO events have been linked to large scale changes in the Atlantic Meridional Overturning Circulation (AMOC) (Blunier & Brook, 2001) through proxies of ocean salinity (Elliot et al., 2001) and North Atlantic Deepwater formation (NADW) (Rasmussen & Thomsen, 2004). Several landmark ice coring efforts across Greenland have revealed the large-scale geographic context of DO events (Johnson et al., 1992; Grootes et al., 1993; Charles et al., 1996; Johnsen et al., 2001; North Greenland Ice Core Project Members, 2004). D-O events are often considered as synonymous with Greenland interstadials (GI), or the warm excursions from the cold climate of the last ice age (Greenland stadials, GS). GS-GI transitions have been a research area for many decades because these transitions are examples of abrupt climate change events that provide critical context for the modern warming world (Severinghaus et al., 1998; Marcott et al., 2013), the cause of DO events is still unclear (Boers, 2018), and the climate effects of rapid warming during the last glacial have a global fingerprint (Brook & Buizert, 2018).

Climate anomalies associated with GS-GI transitions are most notable in the oxygen isotope ratio of Greenland ice, $\delta^{18}O_{ice}$. Dansgaard first detailed the positive correlation between $\delta^{18}O_{snow}$ and the temperature of clouds during snowfall creation (Dansgaard, 1953; Jouzel & Merlivat, 1984), referred to as the temperature effect, and quantified by the quotient $\alpha = \Delta\delta^{18}O / \Delta T$. Paleotemperature reconstructions that utilize the temperature effect hinge on the assumption that the *spatial* relationship between $\delta^{18}O$ and T in the modern day, $\alpha_{spatial}$,

sufficiently approximates the temporal relationship, $\alpha_{temporal}$, and that $\alpha_{temporal}$ does not change in time. The modern value of $\alpha_{spatial}$ is approximately 0.67‰K^{-1} (Dansgaard, 1964; Johnson et al., 2001). Across several GS-GI transitions and several Greenland ice cores, the $\Delta\delta^{18}O_{ice}$ ranges from approximately 2.5‰ to 5.5‰ (Guillevic et al., 2012 Table 3; Bagniewski et al., 2017), implying an approximate ΔT of 3.7 – 8.2 K (here, and for the rest of this paper, the letter Δ represents the GI minus GS difference, or the GS-to-GI change).

The assumption that the modern $\alpha_{spatial} = \alpha_{temporal}$ was challenged by temperature reconstructions from analytical techniques that are generally agreed to be more accurate paleothermometers, such as borehole temperature inversion (Cuffey et al., 1994; Johnson et al., 1995) and $\delta^{15}N$ diffusion (Severinghaus et al., 1998; Landais et al., 2004; Huber et al., 2006; Buizert et al., 2014). These techniques suggest ΔT of approximately 9 – 16 K, or roughly double that of the water isotope-based reconstruction (Lang et al., 1999; Severinghaus & Brook, 1999, Guillevic et al., 2012). Similar results were found in earlier studies of the LGM-pre Industrial temperature difference (Jouzel et al., 1999; Krinner & Werner, 2003). It is clear that α is not constant in time, and the use of $\delta^{18}O_{ice}$ as a paleothermometer is hindered by an incomplete understanding of the role that different climate regimes (e.g. stadial vs. interstadial) have on α.

While the use of $\delta^{18}O_{ice}$ as a paleothermometer contains known problems, $\delta^{18}O_{ice}$ is thought to have relationships with other paleoclimate variables; of particular interest for this study is the $\delta^{18}O_{ice}$-sea ice relationship and seasonal movements of the sea ice edge. The seasonality of precipitation in Greenland has a large impact on $\delta^{18}O_{precip}$ and therefore $\delta^{18}O_{ice}$, and it is highly likely that the seasonality of precipitation changed between GS and GI periods (Thomas et al., 2008). For example, if most precipitation occurs in the summertime, annually averaged $\delta^{18}O_{precip}$ will have a “warm bias” (Krinner et al., 1997; Werner et al., 2000), which can obfuscate isotope-based temperature reconstructions if the proxy is not seasonally laminated (Johnsen et al., 2001). Additionally, the evaporation source location plays a large role in $\delta^{18}O_{precip}$ by determining the initial condition of the $\delta^{18}O_{vapor}$ that eventually forms into Greenland snowfall. The role of evaporation source location is complicated during the last glacial period by seasonally and climatologically varying sea-ice concentration (SIC) in the nearby Atlantic, which is the primary moisture source for much of central and southern

Greenland. Sea ice acts as a semi-impermeable barrier between the ocean and atmosphere, restricting oceanic evaporation and reducing the vapor availability from regions with large SIC. Furthermore, sea ice has dramatically different surface characteristics compared to the open ocean, including albedo and roughness, which can alter the direction and magnitude of moisture transport through shifts in atmospheric circulation.

Numerous studies have utilized isotope-enabled general circulation model simulations to better understand the role of SIC and precipitation seasonality on Greenland $\Delta\delta^{18}O_{ice}$ (Joussaume et al., 1984; Jouzel et al., 1994; Krinner & Genthon, 1998; Krinner & Werner, 2003; Li et al., 2005; Sime et al., 2019). Results of these efforts have yielded significant improvement in the physical basis for sea ice-forced shifts in $\Delta\delta^{18}O_{ice}$. Other modeling ventures have utilized "tagging" technology to specifically highlight the role of moisture source changes on Greenland paleohydrology (e.g. Werner et al., 2001; Sodemann et al., 2008a; Nusbaumer et al., 2019; Cluett et al., 2021). Generally speaking, tagging experiments (or equivalent methods) revealed that the primary moisture source for Greenland precipitation is the north Atlantic, but there is considerable variability in sourcing for different parts of Greenland. The north Pacific and Eurasia are larger contributions to northern Greenland, whereas the north hemisphere Atlantic Ocean and associated seas compose the overwhelming majority of southern and western Greenland precipitation. Moisture source regions tend to not change under climate change scenarios to first order – that is, evaporation basins that supply large amount of vapor to Greenland continue to do so, even in the context of large climate change events. However, smaller changes in the amount of vapor coming from each evaporation region does change. Atmospheric circulation near Greenland is robust to large scale changes in the climate system (e.g. from the PI to the LGM, Werner et al., 2001). Here we seek to evaluate moisture source location changes attributed to DO/interstadial events.

Objectives

The fundamental question of "what controls GS-GI variability in Greenland ice core $\Delta\delta^{18}O$?" is still unsettled. In the modern day, T is one prominent driver of $\delta^{18}O_p$, but this relationship is known to change in time. Recent advancements have demonstrated that

reasonable estimations of ΔSIC can induce proxy-appropriate climate shifts in Greenland, but these effects are not sufficiently quantified. Quantification of these climate factors is a necessary step towards useful model-guided interpretations of Greenland ice cores. In *Chapter 2* of this dissertation, tag- and isotope-enabled model simulations enabled direct quantification of the role of moisture source changes and vapor source isotope ratio changes on total $\Delta\delta^{18}O_p$. In this chapter, the same approach is utilized to quantify the role of changes in SIC on Greenland $\Delta\delta^{18}O_p$ by simulating high- and low-SIC climates, representative of GS and GI climate states, respectively. All analyses focus on the region of Greenland Summit. First, the tag decomposition of Greenland Summit snowfall is computed, highlighting the Summit moisture budget and the isotopic composition of tagged precipitation. This decomposition indicates that sea ice in the GIN seas (Greenland, Irminger, Norwegian seas) plays a critical role by preventing evaporation during wintertime. This effect alone explains the majority of the Greenland $\Delta\delta^{18}O_p$ signal.

Methods and materials

Isotope-enabled CAM

This study utilizes an atmosphere-only modeling setup of the Community Earth System Model v 1.2 (CESM 1.2, Hurrell et al. 2013) with isotope-enabled Community Atmosphere Model (iCAM 5, Nusbaumer et al. 2017) and Community Land Model (iCLM 4.5, Lawrence et al. 2011; Wong et al. 2017) active. 200 years are simulated, with the first 50 removed to allow ample model spin-up, and the last 150 years are averaged to calculate equilibrium climate states. Three simulations are carried out in total: a pre-Industrial control (PI), an interstadial 21 ka with low sea ice fraction (LGM_{GI}), and a stadial 21 ka with high sea ice fraction (LGM_{GS}). The PI experiment follows protocols of the CMIP6 piControl experiment (Otto-Bliesner et al. 2016).

LGM sea-ice setup and experimental design

For the interstadial climate state, the LGM_{GI}, the simulation uses mean annually cycling sea ice concentration (SIC) and sea surface temperatures (SST) from a previously run, fully coupled simulation of the LGM with the Community Climate System Model v4 (CCSM4), the most recent predecessor to CESM. This simulation was forced with PMIP3 specifications for the

LGM, including orbital, greenhouse gas, and vegetation, and have a different continental border, topography, and land ice extent than the PI, to more accurately reflect the LGM. The SIC from the LGM_{GI} simulation is augmented to simulate a colder (stadial) climate by adding sea ice to the Irminger and Labrador seas, as well as the northern Atlantic Ocean just south of Greenland (Sarnthein et al., 2003; Li et al., 2010). Mean annual SST and SIC southern extent are shown in figure 1. SSTs are changed to reflect the changing sea ice boundary – as sea ice is progressively moved southward, the surrounding sea surface must get colder to realistically support the presence of sea ice. Southern boundaries of the sea ice extent for the LGM_{GS} simulation were chosen among a series of sensitivity experiments that added sea ice further south until the cooling consistent with GI-GS transitions was achieved. An assessment of the direct temperature and isotope ratio response relative to the guiding proxy records is given below. While the southern extent of GS sea ice is appropriate based on some proxy assemblages, the seasonality of sea ice is probably overstating the sea ice retreat during stadial summers. In the eastern north Atlantic, the simulated sea ice edge is approximately the same latitude as in the western north Atlantic, whereas the real sea ice edge has longitudinal variability, with sea ice in the eastern north Atlantic being displaced far to the north compared to the western. Currently, the sea ice edge retreats to the same latitude as in the GI experiment during JJA, which is probably not the case for the real GS climate.

Tagging setup

In all simulations, iCESM is modified to include 8 location-based water tracers, or tags, shown in figure 2. Location-based tags utilize iCAM's existing hydrologic framework by assigning a new named "type" of water to the atmospheric vapor budget that results from surface evaporation within the tag region (referred to as "evaporation-based tracers" in Fiorella et al. 2021, see also Nusbaumer et al., 2017). These tags are preserved as vapor is moved horizontally and vertically along advection pathways, altered through phase changes, and as vapor condenses into precipitation, upon which point the tag is reset (Singh et al., 2016a; Singh et al., 2016b). Tags are purely passive tracers – they do not interact with or alter the solutions to the physics and dynamics calculated by the model.

Each tag is defined by one or more rectangular boxes, which are determined using a few criteria. Because of the high computational cost of adding tracers to the model, the tag layout first strikes a balance between relatively high-resolution near the area of interest, and lower resolution further away. Tag regions are then assigned based on shared geographic and climatological features. Coordinates for large bodies of water (e.g. the Greenland, Icelandic, and Norwegian Seas) and continents/land regions (e.g. Northern Eurasia) are approximated to the nearest 2.5 degree. Tags are composed of either completely continental evapotranspiration or oceanic evaporation; the tagged evaporative flux into the model's atmosphere is masked by the relevant surface fraction to account for this.

Decomposition of Greenland Summit $\Delta\delta^{18}O$

The tagging decomposition is thoroughly described in *Chapter 2 Methods and materials*, and is briefly described here. Two variables are calculated: 1) f_{tag}, the fraction of total precipitation that each tag composes; 2) D_{tag}, the base-case-adjusted isotope ratio of tagged precipitation ($D_{tag} = \delta^{18}O_{tag} - \delta^{18}O^{GS}_{total}$; here the LGM_{GS} experiment is our base-case). The isotope ratio change of total rainfall, ΔD_{total}, is:

$$\Delta D_{total} = \sum_{i \in tags} f_i^{GI} * D_i^{GI} - f_i^{GS} * D_i^{GS}$$

which can be rearranged to show

$$\Delta D_{total} = \Delta\delta^{18}O_{total} = \sum_{i \in tags} [\Delta f_i * D_i^{GS}] + [\Delta D_i * f_i^{GS}] + [\Delta f_i * \Delta D_i]$$

This partitions the total isotope ratio change into three physically distinct terms: 1) GI-GS changes in f_{tag} with D_{tag} held constant at the control (GS) value; 2) GI-GS changes in D_{tag} with f_{tag} held constant at the control value; 3) GI-GS changes in D_{tag} and f_{tag} combined, referred to as 1) the f-effect, 2) the D-effect, and 3) the covariance. The decomposition is computed for the model grid cell nearest to the Summit ice core location.

In addition to the tag-based decomposition, the above equations are modified to a time-based scheme, where time is represented by 3-month averages (DJF, MAM, JJA, and SON, referred to as seasons). In the above derivations, the subscript "tag" is substituted for the

subscript “season”. This restructures the decomposition to reflect total precipitation at Greenland as the sum of different seasonal contributions. Both f_{season} and D_{season} are calculated the same way as f_{tag} and D_{tag}.

Results

Model results for ΔT, $\Delta\delta^{18}O_p$

The simulated changes in LGM_{GI} - LGM_{GS} ΔT and $\Delta\delta^{18}O_p$ are compared to proxy-approximated (and isotope-independent) Greenland ΔT and ice core records of $\Delta\delta^{18}O_{ice}$. While no single ΔT or $\Delta\delta^{18}O_{ice}$ value for GI-GS difference exists, this study surveys and averages from the existing literature to assign an appropriate range of values for the ΔT and $\Delta\delta^{18}O_p$ (e.g. Johnsen et al., 2001; NGRIP Project Members, 2004; table 2 from Wolff et al., 2010 and references therein; table 3 from Guillevic et al., 2013; Seierstad et al., 2014; Buizert et al., 2015; Sime et al., 2019). In doing so, this project attempts to compare an approximation of a general stadial climate to a general interstadial climate forced by changes to sea ice concentration plus some small changes in SSTs alone; we do not seek to reconstruct any one interstadial/DO event in particular. The sea ice forcing what chosen to characterize typical GS-GI transitions that occurred during the last glacial period. The model results fall within the suite of available proxy-based reconstructions and paleoclimate datasets: within the ranges of 5.5 – 14 K for ΔT, and 2.5 – 5.5 ‰ for $\Delta\delta^{18}O$. Figure 3 shows the simulated ΔT and $\Delta\delta^{18}O_p$. Both ΔT and $\Delta\ \delta^{18}O$ fall within acceptable ranges. For the approximate location of Summit (72.5° N, 37° W), the interpolated values for ΔT and $\Delta\delta^{18}O_p$ are 7.97 K and 3.17 ‰ respectively.

Summit tag $\Delta\delta^{18}O$ decomposition

Figure 4 shows the annual mean tag decomposition of Greenland Summit $\Delta\delta^{18}O_p$ and figure 4a shows the tagged precipitation amount in mm/day, P_{tag}, for the GI (green dots) and GS (brown dots) experiments at the point 72.5° N, 37° W, the approximate location of Summit Greenland. In the interstadial climate (green dots), precipitation amount increases for every tag compared to the stadial case (brown dots), except for the NEA tag where this is a slight decrease. Subfigure 4b shows the f_{tag} for both experiments. The GIN and A45 tags represent the largest contributions to total Summit precipitation, indicating a strong Atlantic influence from

the south and east. During interstadials, Greenland precipitation is largely composed of GIN vapor (42.5%) and then A45 vapor (23.7%), with the rest of the tags each individually < 10%. During stadials, precipitation composition favors A45 (28.9%) and GIN vapor (19.5%), and the remaining 51.6% is roughly equally divided among SNP, NEA, LND, LGN, and ROW. Δf_{tag} is large and positive only for the GIN tag and very weakly positive for the LHB tag (where Δ refers to the GI-GS, or green dots minus brown dots); for every other tag, Δf_{tag} is negative. This indicates a fractional shift towards predominantly local, eastern, and southeastern Atlantic vapor sources, and away from distant oceanic and land based source during interstadials.

The GI-GS shifts in f_{tag} are largely attributable to a sharp increase in the vapor contribution of the GIN tag to total Summit precipitation. Figure 4a showed the strong increase in GIN precipitation amount during interstadials, whereas all other tags had comparatively weaker increases. GIN precipitation increases from approximately 9.38 mm to 35.82 mm, a fractional increase of 282%. Alternatively, the A45 tag's fractional increase is 43.8%, and other tags are all < 50%. Thus, while there is an increase in the amount of precipitation formed from all sources during GI events except NEA, the apparent decrease in f_{tag} for the minor sources (e.g. figure 4b tags SNP, LND, etc.) occurs because the large increase in GIN precipitation forces the total amount of Summit precipitation to be much greater, making the other tags less significant (lower values of f_{tag}). The dramatic increase in GIN precipitation during interstadials is driven by the removal of sea ice, which occurs predominately in the GIN region, during interstadial events, resulting in large increases in potential evaporation over the newly exposed liquid ocean surface.

Figure 4c shows D_{tag}, the adjusted isotope ratio of the tagged precipitation. D_{tag} adjusts the conventional isotope ratio, δ_{tag}, to highlight enrichment or depletion relative to the control isotope ratio, the GS δ_{Summit}. Using this convention, negative values of D_{tag} are tags that have isotope ratios less than the control (GS) isotope ratio for total Summit precipitation, and vice versa for positive values of D_{tag}. To first order, D_{tag} appears to be negatively correlated with the nominal distance between tag location and endpoint location. For example, vapor from the subtropical North Pacific (SNP), a distant source region, is more depleted than vapor from the subtropical Atlantic (A45), a nearby source region. This is likely due to increased distillation on

longer vapor transport paths. Inter-tags D differences are an order of magnitude larger than intra-tag difference. For example, the difference between D_{SNP} and D_{A45} is approximately 25‰, whereas the difference between the GI D_{SNP} and GS D_{SNP} is approximately 2.5‰ (likewise for all other tags). This suggests that vapor source location plays a larger role in driving tag-specific isotope ratios than the climate changes associated with the two experiments. As such, one might expect that changes in the vapor source distribution (Δf_{tag}) play a larger role in shaping overall Summit $\delta^{18}O_p$.

Figure 4d shows the 3-term decomposition of the GI-GS $\Delta\delta^{18}O_{Summit}$, i.e. the f-term (red dots), D-term (blue dots), and covariance (black dots). The majority of the 3.25 ‰ $\Delta\delta^{18}O_{Summit}$ signal is driven by the f-term for the GIN tag, indicated by the relatively large positive value of the f-term (red point). This results from a combination of positive Δf_{GIN} and positive D_{GIN}: by *greatly increasing* the amount of *relatively enriched* vapor source, the overall contribution of the GIN tag is to shift Summit $\Delta\delta^{18}O_p$ towards the positive. The f-term contribution of SNP and the D-term of A45 also have a relatively minor enriching influence. For the f-term of SNP this occurs for the opposite reason of the GIN tag: by *reducing* the contributions from a relatively *depleted* tag, the overall contribution of SNP is to shift total Summit $\Delta\delta^{18}O_p$ towards the positive. The D-term of A45 results from the combination of positive ΔD_{A45} and a relatively large value of GS f_{A45}. By *increasing* the isotope ratio of a *relatively important* tag (i.e. high value of f_{tag}), the influence of A45 is to shift total Summit $\Delta\delta^{18}O_p$ towards the positive. The sum of the f-terms for GIN and SNP plus the D-term for A45 equals 3.62‰, representing 111.4% of the total $\Delta\delta^{18}O_p$ signal. The remaining tags have weak negative influences that draw the total $\Delta\delta^{18}O_p$ towards the negative. The sum of all blue, red, and black dots in figure 4d equals the total $\Delta\delta^{18}O_p$ signal (3.25‰).

To demonstrate the importance of the GIN tag to Summit $\Delta\delta^{18}O_p$, the decomposition of Summit precipitation was recalculated by assuming that the only change that occurred was the change in ΔP for the GIN tag, i.e. all values for P_{tag} and D_{tag} were kept constant at the control (GS) value, except for the value of P_{GIN}. From this, P_{total}, f_{tag} and the total Summit $\Delta\delta^{18}O_p$ was recalculated as $\Delta\delta^{18}O_p = \Delta\Sigma(f_{tag}*D_{tag})$, which, for this thought experiment, is equal to approximately 3.29‰. This suggests that by increasing the amount of GIN precipitation at

Summit by 282% during interstadials, the isotope ratio increases by 3.29‰, a change that is comparable to the simulated isotope ratio change of 3.25‰. This demonstrates a mechanism by which Summit $\delta^{18}O_p$ can change simply by removing (or adding) a capping layer of sea ice to the primary vapor source region.

Seasonal $\Delta\delta^{18}O$ decomposition

To examine the role of seasonality on $\Delta\delta^{18}O$, the decomposition is computed in terms of time (seasons) rather than space (the tags). In the decomposition derivations, subscripts "tag" are replaced with "ssn" (season), which partitions the total precipitation amount into partial contribution from each season, identical to how the tagging decomposition partitioned total rainfall into contributions from various tags. Figure 5 shows the time-based decomposition for Summit precipitation, with time spanning the 3-month averages of DJF, MAM, JJA, and SON, which are referred to as seasons. The 4 main rows of the decomposition are as in the tag-based decomposition: A) P_{ssn}, B) f_{ssn}, C) D_{ssn}, and D) the 3-term decomposition. As expected, figure 5a indicates that in all seasons, GI precipitation is greater than GS for Summit. Figure 5b demonstrates the dramatic shift in precipitation seasonality between the LGM_{GS} and LGM_{GI}. In the GI climate, precipitation is approximately evenly spread across the entire year, with each 3-month season representing anywhere from 20% – 30% of total annual rainfall, whereas precipitation is partitioned into classic summer and late summer months (JJA and SON) in the GS climate. The higher f_{ssn} during JJA and SON is due to the retreat of southern sea ice during these seasons, which is particularly pronounced in the GS due to the very little amount of precipitation occurring in the other two seasons. Figure 5c, the adjusted isotope ratio, also demonstrates a strong change in the seasonal cycle. For the warm, interstadial climate, D_{ssn} (and, equivalently, $\delta^{18}O_{ssn}$) is relatively similar throughout the seasonal cycle, with D_{ssn} values just slightly more enriched than the control total $\delta^{18}O_{total}$. Over the entire year, D_{ssn} changes by 10‰ at most. In the stadial climate, on the other hand, D_{ssn} changes by approximately 30‰ over the year.

Figure 5d shows the seasonal decomposition of Summit $\Delta\delta^{18}O$. In all seasons, the D-term is positive, indicating that the enrichment across all seasons during interstadials is a large

factor in the total $\Delta\delta^{18}O$ signal; the sum of the 4 D-term (blue dots) equals 4.36‰, which is 134% of the total $\Delta\delta^{18}O$ signal. Additionally, each season has a negative f-term, indicating that the shifts in seasonality coincide with shifts towards seasons with low isotope ratios or away from seasons with high isotope ratios during GI events. For example, in DJF Δf_{DJF} is positive, and control (stadial) D_{DJF} is negative, which is a shift towards a highly depleted season. On the other hand, in JJA Δf_{JJA} is negative, and control (stadial) D_{JJA} is positive, which is a shift away from a highly enriched season. In this sense, interstadial events have a "cold bias" that leads to reductions in isotope ratio, and, equivalently, stadials have a "warm bias" that is leads to increases in isotope ratio. These so-called seasonal biases are outweighed by the D-terms, however, indicating that shifts in the seasonal isotope ratio is more important than shifts in precipitation seasonality. Finally, the covariance value for DJF is the strongest of the covariance influences on the total $\Delta\delta^{18}O$ signal. This value is the combined result of positive Δf_{DJF} *and* positive ΔD_{DJF}. The covariance value of DJF compensates for the negative value of the f-term in DJF – because the f-term uses the product of Δf and the stadial D, if the stadial D is much different than the interstadial D, the f-term will be biased towards the stadial D value. This is the case for DJF, but it is accounted for in the covariance term.

Sea ice control on vapor sourcing and atmospheric circulation

Figure 4 shows that by increasing the amount of precipitation coming from the GIN tag alone, nearly the entire Summit $\Delta\delta^{18}O_p$ signal is achieved. Figure 6 shows the seasonal cycle of the southern extent of sea ice and oceanic evaporation for the interstadial, stadial, and GI-GS difference. Clearly, evaporation in the north Atlantic is restricted by the presence of sea ice in the model. Practically no evaporation occurs north of the 70% concentration sea ice contour in all simulations. There is evidence of evaporation "leaking" through cracks in the sea ice that expose small portions of the ocean surface, the physical phenomenon known as sea ice leads. In the model sea ice fields, this is directly related to sea ice fraction. The sea ice edge usually transitions very quickly from low to high sea ice fraction in the model, which is potentially an unrealistically strong gradient. The sea ice distribution changes are most pronounced in the GIN tag region during the months of DJF and MAM, resulting in strong differences in evaporative flux. This increased flux is reflected in the f-term of GIN from figure 4d.

Figure 5d shows how ΔD_{DJF} was an important source of enrichment for the total Summit $\Delta\delta^{18}O_p$ signal – i.e. during GI events, DJF precipitation was much more enriched, resulting in large positive D-term and covariance values, accounting for most of the total signal. This is also likely related to changes in sea ice presence over the GIN tag region. Oceanic evaporation is enriched relative to other sources of atmospheric vapor, such as evapotranspiration or sublimation from snow/ice. Over sea ice, CESM sublimates the most recent layer of snow into vapor, which is then passed to the atmosphere unfractionated. Snowfall over sea ice tends to have very low isotope ratio because it is occurring in a cold environment where much of the vapor has already been removed by upstream precipitation. This results in a source of atmospheric vapor with a large negative isotope ratio, which is reflected in ΔD_{DJF} (figure 5c).

Discussion

The role of changes in precipitation seasonality for Greenland Summit ice core isotope ratios are well-documented in the literature for DO variability. Seasonality has been shown to induce a "warm bias" during stadials by hindering wintertime precipitation over Greenland Summit, thus partitioning a large fraction of the total annual rainfall in the summertime. In doing so, the isotopes of precipitation are imprinted with the associated summertime climate signals. The results of this study confirm these patterns. The modeled GI response is to increase the fractional amount of wintertime precipitation that occurs, compared to the GS. In the seasonal decomposition, this is seen most evidently as a wintertime signal for the GIN tag, where increased isotope ratio and increased fractional contribution during DJF induce the majority of the total isotope ratio signal. While the warm bias for stadial climates exists in these results (i.e. a higher fraction of annual precipitation occurs in JJA during stadials), the total GS-GI isotope difference is most influenced by changes to the isotope ratio of precipitation during DJF, where the dramatically increased $\delta^{18}O_p$ of GI climates forces large D-effect and covariance values.

From the spatial perspective, these results provide the first quantification of how changes in moisture sourcing influence Greenland Summit isotopes. By adding sea ice to the GIN tag region in the GS climate, atmospheric circulation is changed via changes in surface

roughness and radiative balance. This study shows that in concert with these changes, the near elimination of sea ice in the GIN region, followed by a surplus of evaporation and an increase in the availability of GIN vapor drives the isotope shift at Greenland Summit.

The GS sea ice distribution was chosen by a series of sensitivity experiments that determined how much sea ice was needed in the north Atlantic before simulated Greenland temperatures were accurately reflective of the ice core temperature reconstructions. The target temperature change is known, and the boundary conditions are adjusted until that temperature change is achieved. A further refinement of the approach could utilize a physically-based model of sea ice biased to bring the simulation into agreement with proxies of sea ice extent, and then validate the simulated temperature and precipitation response to the Greenland proxies of T and P. Nevertheless, these results provide evidence that the general GS-GI isotopic differences observed in Greenland Summit ice cores can be induced very simply by greatly reducing evaporation from the GIN seas during winter by the introduction of expansive sea ice anomalies in the North Atlantic.

Bibliography

Bagniewski, W., Meissner, K. J., & Menviel, L. (2017). Exploring the oxygen isotope fingerprint of Dansgaard-Oeschger variability and Heinrich events. *Quaternary Science Reviews*, *159*, 1–14. https://doi.org/10.1016/j.quascirev.2017.01.007

Boers, N. (2018). Early-warning signals for Dansgaard-Oeschger events in a high-resolution ice core record. *Nature Communications*, *9*(1), 2556. https://doi.org/10.1038/s41467-018-04881-7

Bond, G., Showers, W., Cheseby, M., Lotti, R., Almasi, P., deMenocal, P., Priore, P., Cullen, H., Hajdas, I., & Bonani, G. (1997). A Pervasive Millennial-Scale Cycle in North Atlantic Holocene and Glacial Climates. *Science*, *278*(5341), 1257–1266. https://doi.org/10.1126/science.278.5341.1257

Brook, E. J., & Buizert, C. (2018). Antarctic and global climate history viewed from ice cores. *Nature*, *558*(7709), 200–208. https://doi.org/10.1038/s41586-018-0172-5

Buizert, C., Adrian, B., Ahn, J., Albert, M., Alley, R. B., Baggenstos, D., Bauska, T. K., Bay, R. C., Bencivengo, B. B., Bentley, C. R., Brook, E. J., Chellman, N. J., Clow, G. D., Cole-Dai, J., Conway, H., Cravens, E., Cuffey, K. M., Dunbar, N. W., Edwards, J. S., … WAIS Divide Project Members. (2015). Precise interpolar phasing of abrupt climate change during the last ice age. *Nature*, *520*(7549), 661–665. https://doi.org/10.1038/nature14401

Buizert, C., Gkinis, V., Severinghaus, J. P., He, F., Lecavalier, B. S., Kindler, P., Leuenberger, M., Carlson, A. E., Vinther, B., Masson-Delmotte, V., White, J. W. C., Liu, Z., Otto-Bliesner, B., & Brook, E. J. (2014). Greenland temperature response to climate forcing during the last deglaciation. *Science*, *345*(6201), 1177–1180. https://doi.org/10.1126/science.1254961

Charles, C. D., Lynch-Stieglitz, J., Ninnemann, U. S., & Fairbanks, R. G. (1996). Climate connections between the hemisphere revealed by deep sea sediment core/ice core correlations. *Earth and Planetary Science Letters*, *142*(1), 19–27. https://doi.org/10.1016/0012-821X(96)00083-0

Cluett, A. A., Thomas, E. K., Evans, S. M., & Keys, P. W. (2021). Seasonal Variations in Moisture Origin Explain Spatial Contrast in Precipitation Isotope Seasonality on Coastal Western Greenland. *Journal of Geophysical Research: Atmospheres*, *126*(11), e2020JD033543. https://doi.org/10.1029/2020JD033543

Cuffey, K. M., Alley, R. B., Grootes, P. M., Bolzan, J. M., & Anandakrishnan, S. (1994). Calibration of the δ18O isotopic paleothermometer for central Greenland, using borehole temperatures. *Journal of Glaciology*, *40*(135), 341–349. https://doi.org/10.3189/S0022143000007425

Dansgaard, W. (1953). The Abundance of O18 in Atmospheric Water and Water Vapour. *Tellus*, *5*(4), 461–469. https://doi.org/10.1111/j.2153-3490.1953.tb01076.x

Dansgaard, W. (1964). Stable isotopes in precipitation. *Tellus*, *16*(4), 436–468. https://doi.org/10.3402/tellusa.v16i4.8993

Dansgaard, W., Clausen, H. B., Gundestrup, N., Hammer, C. U., Johnsen, S. F., Kristinsdottir, P. M., & Reeh, N. (1982). A New Greenland Deep Ice Core. *Science*, *218*(4579), 1273–1277. https://doi.org/10.1126/science.218.4579.1273

Dansgaard, W., Johnsen, S. J., Clausen, H. B., Dahl-Jensen, D., Gundestrup, N. S., Hammer, C. U., Hvidberg, C. S., Steffensen, J. P., Sveinbjörnsdottir, A. E., Jouzel, J., & Bond, G. (1993). Evidence for general instability of past climate from a 250-kyr ice-core record. *Nature*, *364*(6434), 218–220. https://doi.org/10.1038/364218a0

Elliot, M., Labeyrie, L., Dokken, T., & Manthé, S. (2001). Coherent patterns of ice-rafted debris deposits in the Nordic regions during the last glacial (10–60 ka). *Earth and Planetary Science Letters*, *194*(1), 151–163. https://doi.org/10.1016/S0012-821X(01)00561-1

Fiorella, R. P., Siler, N., Nusbaumer, J., & Noone, D. C. (2021). Enhancing Understanding of the Hydrological Cycle via Pairing of Process-Oriented and Isotope Ratio Tracers. *Journal of Advances in Modeling Earth Systems*, *13*(10), e2021MS002648. https://doi.org/10.1029/2021MS002648

Genty, D., Blamart, D., Ouahdi, R., Gilmour, M., Baker, A., Jouzel, J., & Van-Exter, S. (2003). Precise dating of Dansgaard–Oeschger climate oscillations in western Europe from stalagmite data. *Nature*, *421*(6925), 833–837. https://doi.org/10.1038/nature01391

Grootes, P. M., Stuiver, M., White, J. W. C., Johnsen, S., & Jouzel, J. (1993). Comparison of oxygen isotope records from the GISP2 and GRIP Greenland ice cores. *Nature*, *366*(6455), 552–554. https://doi.org/10.1038/366552a0

Guillevic, M., Bazin, L., Landais, A., Kindler, P., Orsi, A., Masson-Delmotte, V., Blunier, T., Buchardt, S. L., Capron, E., Leuenberger, M., Martinerie, P., Prié, F., & Vinther, B. M. (2013). Spatial gradients of temperature, accumulation and δ^{18}O-ice in Greenland over a series of Dansgaard–Oeschger events. *Climate of the Past*, *9*(3), 1029–1051. https://doi.org/10.5194/cp-9-1029-2013

Huber, C., Leuenberger, M., Spahni, R., Flückiger, J., Schwander, J., Stocker, T. F., Johnsen, S., Landais, A., & Jouzel, J. (2006). Isotope calibrated Greenland temperature record over Marine Isotope Stage 3 and its relation to CH4. *Earth and Planetary Science Letters*, *243*(3), 504–519. https://doi.org/10.1016/j.epsl.2006.01.002

Hurrell, J. W., Holland, M. M., Gent, P. R., Ghan, S., Kay, J. E., Kushner, P. J., Lamarque, J.-F., Large, W. G., Lawrence, D., Lindsay, K., Lipscomb, W. H., Long, M. C., Mahowald, N., Marsh, D. R., Neale, R. B., Rasch, P., Vavrus, S., Vertenstein, M., Bader, D., … Marshall, S. (2013). The Community Earth System Model: A Framework for Collaborative Research. *Bulletin of the American Meteorological Society*, *94*(9), 1339–1360. https://doi.org/10.1175/BAMS-D-12-00121.1

Johnsen, S. J., Clausen, H. B., Dansgaard, W., Fuhrer, K., Gundestrup, N., Hammer, C. U., Iversen, P., Jouzel, J., Stauffer, B., & Steffensen, J. P. (1992). Irregular glacial interstadials recorded in a new Greenland ice core. *Nature*, *359*(6393), 311–313. https://doi.org/10.1038/359311a0

Johnsen, S. J., Dahl-Jensen, D., Gundestrup, N., Steffensen, J. P., Clausen, H. B., Miller, H., Masson-Delmotte, V., Sveinbjörnsdottir, A. E., & White, J. (2001). Oxygen isotope and palaeotemperature records from six Greenland ice-core stations: Camp Century, Dye-3, GRIP, GISP2, Renland and NorthGRIP. *Journal of Quaternary Science*, *16*(4), 299–307. https://doi.org/10.1002/jqs.622

Joussaume, S., Sadourny, R., & Jouzel, J. (1984). A general circulation model of water isotope cycles in the atmosphere. *Nature*, *311*(5981), 24–29. https://doi.org/10.1038/311024a0

Jouzel, J. (1999). Calibrating the Isotopic Paleothermometer. *Science*, *286*(5441), 910–911. https://doi.org/10.1126/science.286.5441.910

Jouzel, J., Alley, R. B., Cuffey, K. M., Dansgaard, W., Grootes, P., Hoffmann, G., Johnsen, S. J., Koster, R. D., Peel, D., Shuman, C. A., Stievenard, M., Stuiver, M., & White, J. (1997). Validity of the temperature reconstruction from water isotopes in ice cores. *Journal of Geophysical Research: Oceans*, *102*(C12), 26471–26487. https://doi.org/10.1029/97JC01283

Jouzel, J., & Merlivat, L. (1984). Deuterium and oxygen 18 in precipitation: Modeling of the isotopic effects during snow formation. *Journal of Geophysical Research: Atmospheres*, *89*(D7), 11749–11757. https://doi.org/10.1029/JD089iD07p11749

Krinner, G., & Genthon, C. (1998). GCM simulations of the Last Glacial Maximum surface climate of Greenland and Antarctica. *Climate Dynamics*, *14*(10), 741–758. https://doi.org/10.1007/s003820050252

Krinner, G., Genthon, C., & Jouzel, J. (1997). GCM analysis of local influences on ice core δ signals. *Geophysical Research Letters*, *24*(22), 2825–2828. https://doi.org/10.1029/97GL52891

Krinner, G., & Werner, M. (2003). Impact of precipitation seasonality changes on isotopic signals in polar ice cores: A multi-model analysis. *Earth and Planetary Science Letters*, *216*(4), 525–538. https://doi.org/10.1016/S0012-821X(03)00550-8

Landais, A., Steffensen, J. P., Caillon, N., Jouzel, J., Masson-Delmotte, V., & Schwander, J. (2004). Evidence for stratigraphic distortion in the Greenland Ice Core Project (GRIP) ice core during Event 5e1 (120 kyr BP) from gas isotopes. *Journal of Geophysical Research: Atmospheres*, *109*(D6). https://doi.org/10.1029/2003JD004193

Lang, C., Leuenberger, M., Schwander, J., & Johnsen, S. (1999). 16°C Rapid Temperature Variation in Central Greenland 70,000 Years Ago. *Science*, *286*(5441), 934–937. https://doi.org/10.1126/science.286.5441.934

Lawrence, D. M., Oleson, K. W., Flanner, M. G., Thornton, P. E., Swenson, S. C., Lawrence, P. J., Zeng, X., Yang, Z.-L., Levis, S., Sakaguchi, K., Bonan, G. B., & Slater, A. G. (2011). Parameterization improvements and functional and structural advances in Version 4 of the Community Land Model. *Journal of Advances in Modeling Earth Systems*, *3*(1). https://doi.org/10.1029/2011MS00045

Li, C., Battisti, D. S., & Bitz, C. M. (2010). Can North Atlantic Sea Ice Anomalies Account for Dansgaard–Oeschger Climate Signals? *Journal of Climate*, *23*(20), 5457–5475. https://doi.org/10.1175/2010JCLI3409.1

Li, C., Battisti, D. S., Schrag, D. P., & Tziperman, E. (2005). Abrupt climate shifts in Greenland due to displacements of the sea ice edge. *Geophysical Research Letters*, *32*(19). https://doi.org/10.1029/2005GL023492

Marcott, S. A., Shakun, J. D., Clark, P. U., & Mix, A. C. (2013). A Reconstruction of Regional and Global Temperature for the Past 11,300 Years. *Science*, *339*(6124), 1198–1201. https://doi.org/10.1126/science.1228026

Nusbaumer, J., Alexander, P. M., LeGrande, A. N., & Tedesco, M. (2019). Spatial Shift of Greenland Moisture Sources Related to Enhanced Arctic Warming. *Geophysical Research Letters*, *46*(24), 14723–14731. https://doi.org/10.1029/2019GL084633

Nusbaumer, J., & Noone, D. (2018). Numerical Evaluation of the Modern and Future Origins of Atmospheric River Moisture Over the West Coast of the United States. *Journal of Geophysical Research: Atmospheres*, *123*(12), 6423–6442. https://doi.org/10.1029/2017JD028081

Nusbaumer, J., Wong, T. E., Bardeen, C., & Noone, D. (n.d.). Evaluating hydrological processes in the Community Atmosphere Model Version 5 (CAM5) using stable isotope ratios of water. *Journal of Advances in Modeling Earth Systems*, *9*(2), 949–977. https://doi.org/10.1002/2016MS000839

Otto-Bleisner, B. L., Braconnot, P., Harrison, S. P., Lunt, D. J., Abe-Ouchi, A., Albani, S., Bartlein, P. J., Capron, E., Carlson, A. E., Dutton, A., Fischer, H., Goelzer, H., Govin, A., Haywood, A., Joos, F., Legrande, A. N., Lipscomb, W. H., Lohmann, G., Mahowald, N., … Renssen, H. (2016). The PMIP4 contribution to CMIP6 – Part 2: Two interglacials, scientific objective and experimental design for Holocene and last interglacial simulations. *Geoscientific Model Development Discussions*, *10.5194/gmd-2016–279*. http://centaur.reading.ac.uk/68688/

Rasmussen, T. L., & Thomsen, E. (2004). The role of the North Atlantic Drift in the millennial timescale glacial climate fluctuations. *Palaeogeography, Palaeoclimatology, Palaeoecology*, *210*(1), 101–116. https://doi.org/10.1016/j.palaeo.2004.04.005

Sarnthein, M., Pflaumann, U., & Weinelt, M. (2003). Past extent of sea ice in the northern North Atlantic inferred from foraminiferal paleotemperature estimates. *Paleoceanography*, *18*(2). https://doi.org/10.1029/2002PA000771

Schulz, M. (2002). On the 1470-year pacing of Dansgaard-Oeschger warm events. *Paleoceanography*, *17*(2), 4-1-4–9. https://doi.org/10.1029/2000PA000571

Seierstad, I. K., Abbott, P. M., Bigler, M., Blunier, T., Bourne, A. J., Brook, E., Buchardt, S. L., Buizert, C., Clausen, H. B., Cook, E., Dahl-Jensen, D., Davies, S. M., Guillevic, M., Johnsen, S. J., Pedersen, D. S., Popp, T. J., Rasmussen, S. O., Severinghaus, J. P., Svensson, A., & Vinther, B. M. (2014). Consistently dated records from the Greenland GRIP, GISP2 and NGRIP ice cores for the past 104 ka reveal regional millennial-scale δ18O gradients with possible Heinrich event imprint. *Quaternary Science Reviews*, *106*, 29–46. https://doi.org/10.1016/j.quascirev.2014.10.032

Severinghaus, J. P., & Brook, E. J. (1999). Abrupt Climate Change at the End of the Last Glacial Period Inferred from Trapped Air in Polar Ice. *Science*, *286*(5441), 930–934. https://doi.org/10.1126/science.286.5441.930

Severinghaus, J. P., Sowers, T., Brook, E. J., Alley, R. B., & Bender, M. L. (1998). Timing of abrupt climate change at the end of the Younger Dryas interval from thermally fractionated gases in polar ice. *Nature*, *391*(6663), 141–146. https://doi.org/10.1038/34346

Sime, L. C., Hopcroft, P. O., & Rhodes, R. H. (2019). Impact of abrupt sea ice loss on Greenland water isotopes during the last glacial period. *Proceedings of the National Academy of Sciences*, *116*(10), 4099–4104. https://doi.org/10.1073/pnas.1807261116

Singh, H. A., Bitz, C. M., Nusbaumer, J., & Noone, D. C. (2016). A mathematical framework for analysis of water tracers: Part 1: Development of theory and application to the preindustrial mean state. *Journal of Advances in Modeling Earth Systems*, *8*(2), 991–1013. https://doi.org/10.1002/2016MS000649

Singh, H. K. A., Bitz, C. M., Donohoe, A., Nusbaumer, J., & Noone, D. C. (2016). A Mathematical Framework for Analysis of Water Tracers. Part II: Understanding Large-Scale Perturbations in the Hydrological Cycle due to CO2 Doubling. *Journal of Climate*, *29*(18), 6765–6782. https://doi.org/10.1175/JCLI-D-16-0293.1

Sodemann, H., Schwierz, C., & Wernli, H. (2008). Interannual variability of Greenland winter precipitation sources: Lagrangian moisture diagnostic and North Atlantic Oscillation influence. *Journal of Geophysical Research: Atmospheres*, *113*(D3). https://doi.org/10.1029/2007JD008503

Thomas, E. R., Mulvaney, R., & Wolff, E. W. (2008). A change in seasonality in Greenland during a Dansgaard–Oeschger warming. *Annals of Glaciology*, *48*, 19–24. https://doi.org/10.3189/172756408784700590

Voelker, A. H. L. (2002). Global distribution of centennial-scale records for Marine Isotope Stage (MIS) 3: A database. *Quaternary Science Reviews*, *21*(10), 1185–1212. https://doi.org/10.1016/S0277-3791(01)00139-1

Werner, M., Heimann, M., & Hoffmann, G. (2001). Isotopic composition and origin of polar precipitation in present and glacial climate simulations. *Tellus B: Chemical and Physical Meteorology*, *53*(1), 53–71. https://doi.org/10.3402/tellusb.v53i1.16539

Werner, M., Mikolajewicz, U., Heimann, M., & Hoffmann, G. (2000). Borehole versus isotope temperatures on Greenland: Seasonality does matter. *Geophysical Research Letters*, *27*(5), 723–726. https://doi.org/10.1029/1999GL006075

Wolff, E. W., Chappellaz, J., Blunier, T., Rasmussen, S. O., & Svensson, A. (2010). Millennial-scale variability during the last glacial: The ice core record. *Quaternary Science Reviews*, *29*(21), 2828–2838. https://doi.org/10.1016/j.quascirev.2009.10.013

Wong, T. E., Nusbaumer, J., & Noone, D. C. (n.d.). Evaluation of modeled land-atmosphere exchanges with a comprehensive water isotope fractionation scheme in version 4 of the Community Land Model. *Journal of Advances in Modeling Earth Systems*, *9*(2), 978–1001. https://doi.org/10.1002/2016MS000842

Figures & Tables

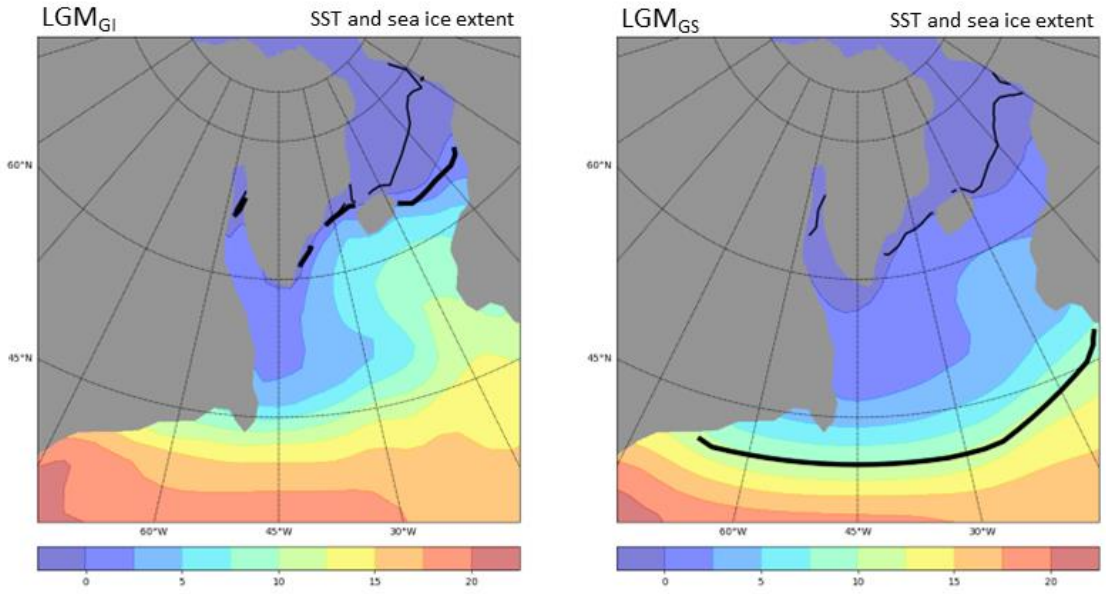

Figure 3.1 Sea ice southern extent and annual mean SST for warm/LGM$_{GI}$ (left) and cold/LGM$_{GS}$ (right). SSTs are shown as colored contours in °C. Sea ice southern extent is shown as black contour line, thick lines are the March boundary and thin lines are the September boundary (both defined by 40% ice concentration).

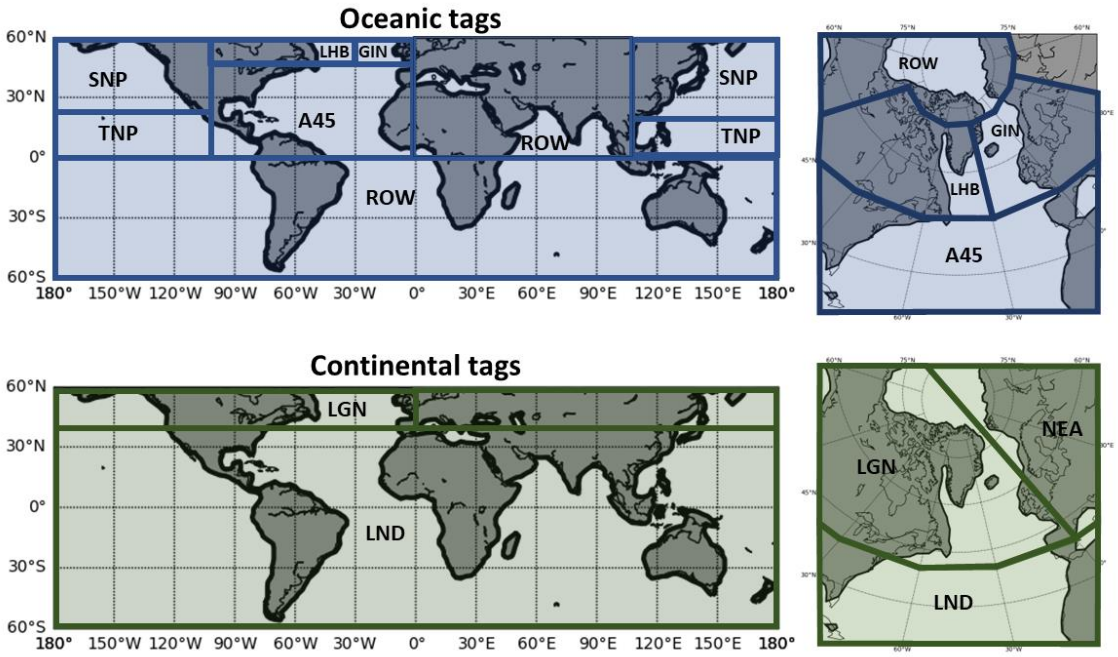

Figure 3.2 The tag layout. In blue (top) are the oceanic tags, where evaporation is multiple by the fraction of the model grid cell that is covered by an ocean. In green (bottom) are the continental tags, similar to the oceanic tags, but masked by the land fraction of each grid cell. Inlays of Greenland are shown to the right for both oceanic and continental tags to highlight local tag detail. All land surfaces are assigned a tag, but not all oceanic surfaces are. Non-tagged oceanic surfaces (including the southern hemisphere oceans, the Indian Ocean, and the Arctic Ocean) are included in the ROW tag calculation. See metadata in Table 3.1

Tag	Long name	Location (S,N,E,W)	Surface
A45	Atlantic Ocn south of 45° N	0, 45, 260, 360	Ocean
LHB	Labrador, Hudson, Baffin	45, 75, 255, 315	Ocean
GIN	Greenland, Icelandic, Norwegian seas	45, 75, 315, 105	Ocean
SNP	Subtropical North Pac Ocn	23.5, 75, 105, 260	Ocean
TNP	Tropical North Pac Ocn	0, 23.5, 105, 255	Ocean
LGN	Laurentide and Greenland	40, 90, 195, 360	Land
NEA	Northern Eurasia	40, 90, 0, 195	Land
LND	Land South of 40° N	-90, 40, 0 , 360	Land

Table 3.1 The tag layout metadata

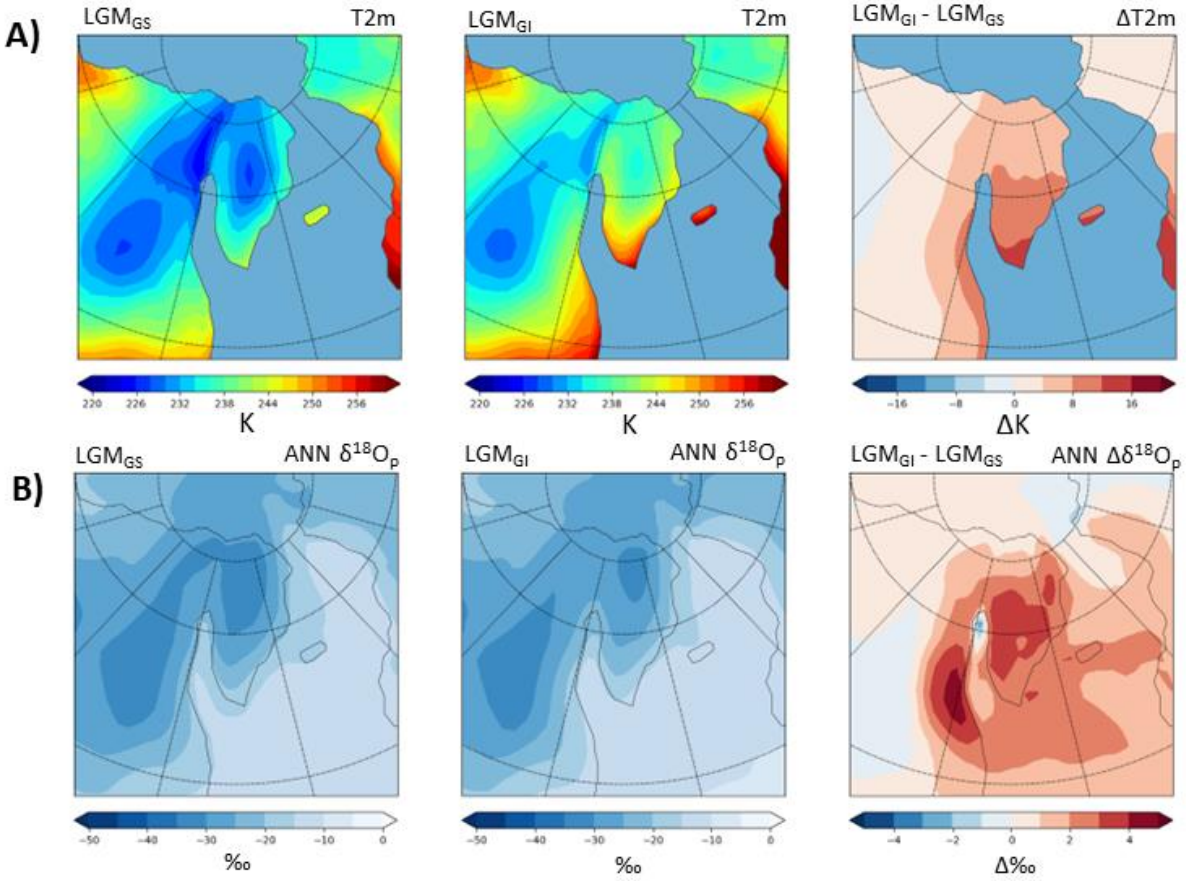

Figure 3.3 Temperature and precipitation isotope ratio changes during GI, GS, and the GI-GS difference. A) Annual mean 2m air temperature for the LGM_{GS} (left), LGM_{GI} (middle), and $LGM_{GI} – LGM_{GS}$ difference (right); B) annual mean amount-weighted $\delta^{18}O_p$ for the same climates as in (A).

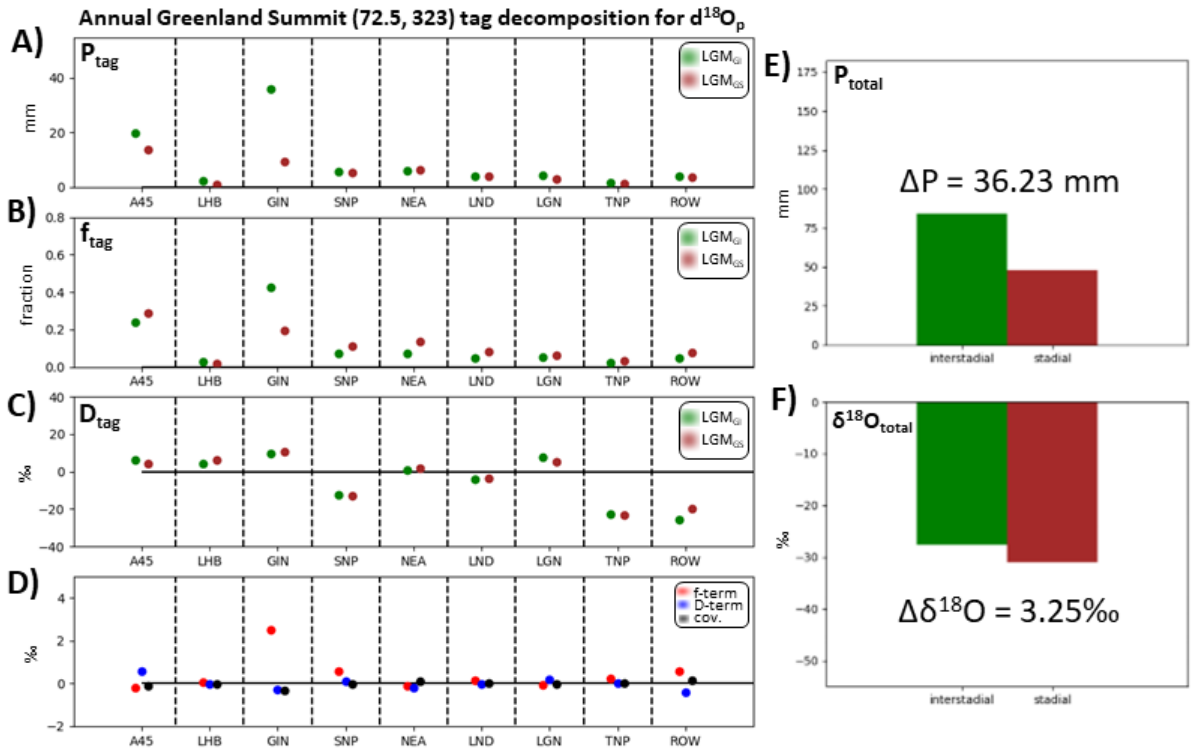

Figure 3.4 Decomposition of annual sum Greenland Summit precipitation into tag regions. In (A) – (C), and (E) – (F), green dots and bars represent the LGM_{GI} and brown the LGM_{GS}. A) P_{tag}, the total precipitation (mm/day) from each tag; B) f_{tag}, the fractional vapor contribution to total Greenland Summit precipitation. C) D_{tag}, the adjusted isotope ratio of tagged precipitation; D) the three-term decomposition of Greenland Summit $\Delta\delta^{18}O_{total}$ (see Methods); E) the total annual Greenland Summit precipitation amount F) the annual mean, amount-weighted isotope ratio of Greenland Summit precipitation

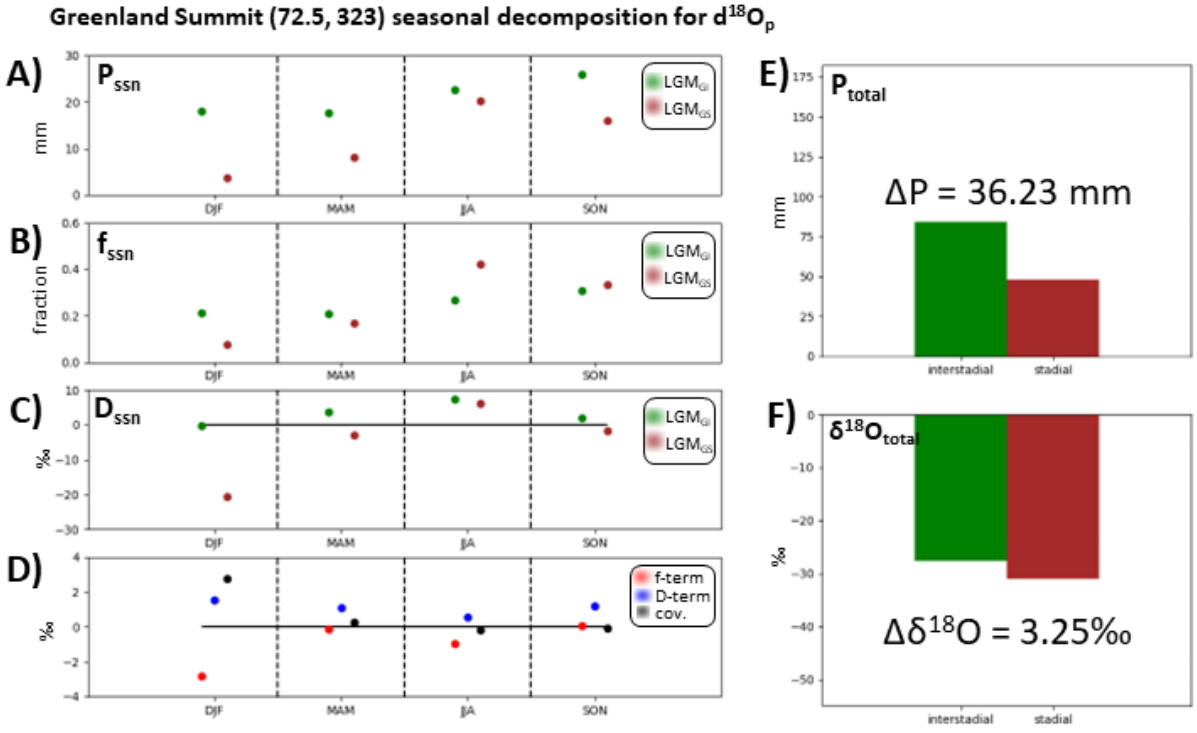

Figure 3.5 Decomposition of Greenland Summit precipitation into seasons. In all rows, the x-axis denotes the 3-month seasonal average, i.e. DJF, MAM, JJA, and SON. In (a) – (c), green dots are values from the LGM_{GI} simulation and brown dots are from LGM_{GS}. A) P_{ssn}, the distribution of Greenland Summit precipitation (in mm/day) across the season; B) f_{ssn}, the fractional contribution of each season to total annual Summit precipitation; C) D_{ssn}, the adjusted isotope ratio of rainfall for each season; D) the three-term decomposition (f-term in blue, D-term in red; covariance in black); E) and F) the total precipitation amount (mm summed over the year) and $\delta^{18}O_p$ for annual mean Summit precipitation (same subfigures as in fig 3.4).

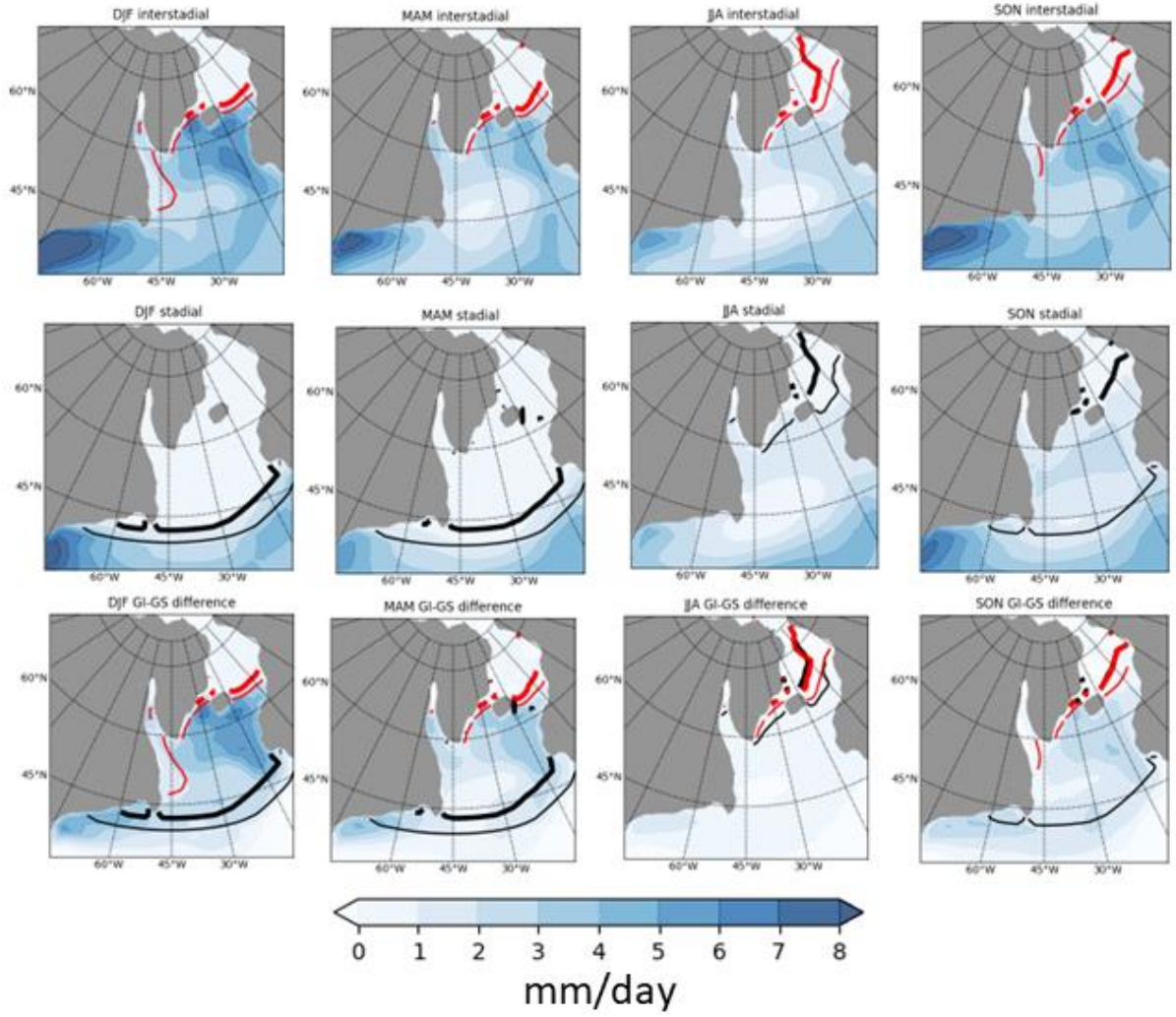

Figure 3.6 Evaporation and sea ice extent across the seasonal cycle. Rows represent the LGM_{GI} and LGM_{GS} experiments, with the last row as the GI-GS difference. Columns are ordered in time as DJF, MAM, JJA, and SON averages. Colored filled contours are the evaporative flux, in mm/day. Line contours are the southern extent of sea ice for the 30% (thin line) and 70% (thick line) concentrations. In all subfigures, red lines are the sea ice extent for LGM_{GI} and black lines are for LGM_{GS}.

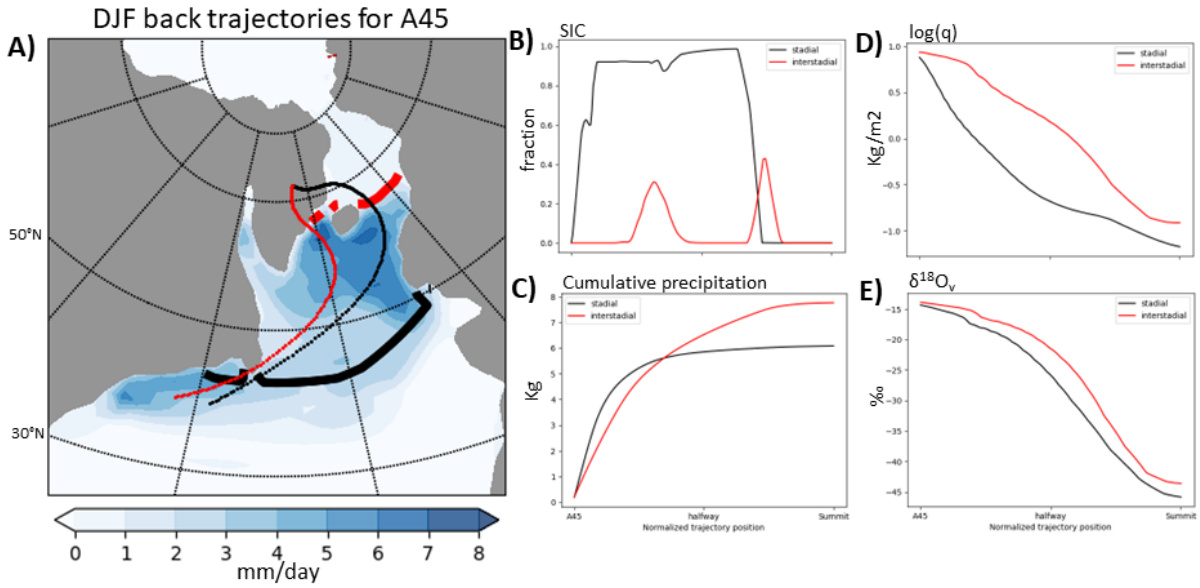

Figure 3.7 1 hour back-trajectories of A45 tagged vapor with evaporation contours and sea ice southern extent, all using DJF data. Thin lines converging at Greenland Summit are the trajectories (calculated as backwards trajectories) from the A45 tag region to Greenland Summit. Bold lines are the southern border of 70% SIC. For all line contours, red represent the LGM_{GI} and black represents the LGM_{GS}. Blue filled contours are the GI-GS difference in evaporative flux. (B) - (E) are 4 variables calculated along the trajectories, oriented from source to Greenland going left to right: B) sea ice concentration; C) cumulative precipitation ($\sum P^*\Delta T$); D) log of column integrated q, the mixing ratio of water vapor; E) $\delta^{18}O_v$, the oxygen isotope ratio of column integrated water vapor.

General Conclusion

Isotope-based proxies provide unique and important information on the state of past hydroclimates, but their relationships to climate phenomena, both large-scale and small-scale, and in both time and space, are not well constrained. This critical knowledge gap hinders the potential power of isotope proxies. For example, tropical δ_p-based proxies are thought of as representative of changes in precipitation amount, but it is known that δ_p integrates more climate information than simply how much rain fell at a particular location. Knowing that rainfall changes occurred is one thing, but a more consequential follow-up question is "why did that change occur?". Answering this question provides more detailed insight into past climate states and provides an analogue for application to future climate change. Furthermore, while δ_p may be related to rainfall amount via amount-effect-like correlations, the amount-effect never explains all the variance in δ_p. Isotope proxies are increasingly being thought of as surveyors and integrators of circulation-scale atmospheric dynamics. This dissertation presents evidence that δ_p can be considered through the perspective of shifts in the spatial variability of moisture sourcing, shifts in the fractionating influences of hydrologic processes, and shifts in the pathways between the vapor source and precipitation sink.

For any given location, δ_p is ultimately very simple if you are a climate model. Evaporation provides vapor of a particular isotope ratio to the atmosphere above. This vapor is then moved around via winds; some of it makes it to the location at hand, condenses in clouds, and falls to the ground. Along this path, isotopic fractionation occurs at three points: 1) evaporation from the surface, 2) precipitation events during vapor transport, and 3) condensation into cloud drops. Ignoring the non-fractionating effects of mixing (which is enabled through the use of water tracers), from the initial evaporation source to the eventual precipitation sink, the sum of these three terms constitutes the isotope ratio of precipitation for a given moisture source, and the weighted average of all vapor sources constitutes the total precipitation isotope ratio. In this sense, δ_p is the end-member of cumulative upstream and local fractionation processes; by accumulating these fractionations, one completes the source-to-sink diagram of δ_p. This is true regardless of geography – the poles, the equator, and

everywhere in between follow this basic isotopic circulation. This approach formed the backbone for the analyses from chapter 2 and 3, and by quantifying the bulk effects of fractionation at the three points along the vapor transport, the upstream influences of fractionating effects on local isotope ratios along a few vapor streamlines were achieved.

The need to determine circulation-scale influences on local δ_p establishes a critical conclusion from this dissertation: accurate and useful interpretations of δ_p-based proxies necessitate the use of an isotope-enabled atmospheric circulation model. If changes in δ_p are to be thought of as reflecting changes in upstream circulation, one must have access to the complete upstream climate, which is only achievable via a circulation model. Despite attempts to expand the spatial extent over which they may be interpreted, δ_p-based proxies remain inherently restricted by their point-based nature, and as such require a circulation model to fill in the gaps between their point-based nature and the circulations interacting with them.

The decomposition results from chapters 2 and 3 present an interesting thought experiment. Imagine a region where precipitation comes entirely from 4 evaporating basins (4 tags, per the language of chapters 2 and 3). Further imagine that the isotope ratio of all tagged rainfall decreases in some perturbation experiment compared to a control. In the decomposition, this is referred to as negative ΔD_{tag}. In this scenario, as long as intra-tag variability in D_{tag} is sufficiently large, it is possible to construct a shift in atmospheric circulation that results in a higher total isotope ratio, even though the isotope ratios of the contributing tags were all lower. This is accomplished by shifting the pattern of moisture sourcing towards areas that have numerically positive contributions to precipitation isotope ratios, and away from areas that contribute numerically negatively to isotope ratios. This is demonstrated schematically in figure 1. In this hand-crafted perturbation experiment, all tagged isotope ratios are more depleted in the perturbation than in the control, but there is an accompanying shift in moisture sourcing towards tag 4 and away from tag 1. Because tag 4 is generally a tag with positive isotope ratio, and tag 1 with generally negative, this manifests as large positive f-terms for tag 1 and 4, and total rainfall isotope ratio change of about 3.5‰ compared to the control. This thought experiment is ultimately an extension of the results from chapters 2 and 3, where shifts towards the negative contributions of the Pacific were the controlling factor on EASM

isotopes, and shifts towards the positive contributions of the GIN tag controlled GI enrichment for Summit precipitation isotope ratios. These results highlighted the potential role of low-contribution sources (e.g. the NPA and SPA), and emphasizes the fact that, for rainfall composed of many source regions with distinct isotope ratios, systematic shifts in moisture sourcing towards vapor source regions of a particular isotopic composition compose the majority of the total isotope ratio signal at the precipitation location.

Collections of spatially expansive δ_p-based proxies are another way in which proxy-guided climate reconstructions can provide climate information on spatial scales larger than an individual proxy. In chapter 1 it was shown that zonal- and meridional-mean circulation changes induced similar changes in the zonal- and meridional-mean profiles of simulated δ_p, suggesting that climate phenomena that exist over large spatial scales (e.g., scales of the entire tropics) have a controlling influence on isotope ratios averaged over those same spatial scales. By expanding the δ_p proxy network, more accurate estimations of zonal- and meridional-mean δ_p are enabled, which further enables an accurate recreation of the related large-scale circulation cells. A lack of δ_p-based proxies in several areas of the tropics is a hinderance to the combined utility of models and proxies, and filling in the spatial gaps where insufficient δ_p-based proxies assemblages exist, for example in India and northern Africa (for the MH), should be considered a critical scientific endeavor.

Figures

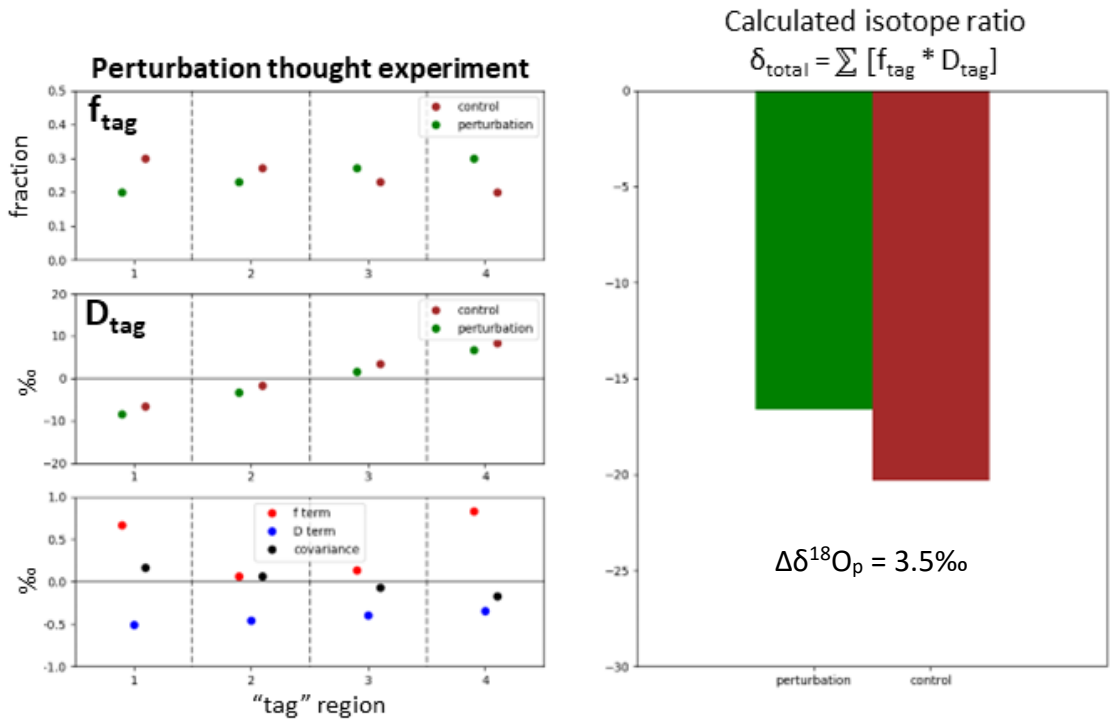

Figure C.1 The constructed decomposition of the perturbation thought experiment. In the perturbation, isotope ratios of each tag are more depleted than the control, but the perturbation total isotope ratio is more enriched than the control